Mechanics of thin carbon fiber composites with a silicone matrix

Thesis by

Francisco López Jiménez

In Partial Fulfillment of the Requirements

for the Degree of

Doctor of Philosophy

California Institute of Technology

Pasadena, California

2011

(Defended January 7, 2011)

A mis abuelos, que no pudieron estudiar,
pero para los que la educación de sus hijos fue lo primero.

Acknowledgements

This section is nothing but a brief, scarce summary: the people I need to thank are too many, the list of debts I have is too long to detail.

The work presented in this thesis would not have been possible without the guidance and support of my advisor, Professor Sergio Pellegrino. It has been honor to be his first Caltech student. I have been always particularly impressed by his willingness to spend as much time as iwas required (sometimes more than two hours) discussing a problem. Looking back, those meetings were some of the most enjoyable parts of my stay at Caltech.

I also need to extend my deepest gratitude to the members of my both my thesis defense and candidacy examination committees, Professors Michael Ortiz, Guruswami "Ravi" Ravichandran, Kaushik Bhattacharya and Chiara Daraio, and Dr. Mark Thompson. Their support and advice, both scientific and personal, was key during several points of my Ph.D. I am particularly grateful to Professor Ortiz, who is the main responsible, along with Professor Pilar Ariza from the University of Seville, for my involvement with Caltech. I will never forget the opportunity they gave me. Finally, I want to acknowledge the support and inspiration of Professors Jaime Domínguez Abascal and José Domínguez Abascal.

Besides my advisor and committee members, several other people have provided suggestions or help at one point or another. Dr. Leri Datashvili, Dr. Julián Santiago-Prowald, Professor Wolgang Knauss, Professor Mathieu Desbrun, Dr. Abha Misra, Jingqing Huang, Dr. Laurence Bodelot, Dr. Daniel Balzani, all of them were more than eager to give me a hand when in need.

I want to thank the sponsorship of the Keck Institute of Space Studies at Caltech, and the Earl K. Sears fellowship, which allowed me to focus on my research without having to worry about funding.

Caltech would be a much less nice place if it weren't for the people who make everything

easy. From the administrative stuff, to the catering, to the several labs, everybody works make the lives of the students easier and more pleasant. I need to particularly thank John Van Deusen from the Mechanical Engineering Machine Shop, for his mentoring, advice, and his inhuman patience while explaining me how to change the tool in the lathe for the n-th time.

My work conditions would have been substantially more miserable without the great interaction with the rest of the members in Professor Pellegrino's research group. You guys have greatly contributed to both my research and personal life. I need to mention particularly the two people with whom I worked more closely, my office mate Chinthaka, who many times acted as a postdoc, helping everybody in the group, and Kawai, partner in many night discussions, due to our common (and late) timetables.

All my friends at Caltech have been essential for my happiness. Celia, Olive, Yacine, the Spanish crowd, Pia, Greg, Andreas, Dev, Phil, Jim, Flora, Daniel and family, and many others, from getting a coke and taking a walk to sharing the madness of the first year, you were always there. As a more gifted writer said once, "defeats are softened and victories are sweeter because we did them together".

Everybody involved in the Caltech Classroom Connection, the people coming to movie night, my Erasmus friends, everybody in Seville (María, Mercedes, all my high school and college friends) and all my family (both the very small one I was born with, and the larger one I found on the way here; you all know who you are), you all helped me at looking at things with a little bit of perspective and distance, and putting, even if briefly, the research problems aside.

Finally, nothing would have happened without the support and love of my parents and sister, who inspired me with their integrity and work ethics, and who always encouraged me to follow my dreams, even if that involved moving to the other side of the world. You made me who I am.

Gracias a todos.

Abstract

This thesis presents an experimental, numerical and analytical study of the behavior of thin fiber composites with a silicone matrix. The main difference with respect to traditional composites with epoxy matrix is the fact that the soft matrix allows the fibers to microbuckle without breaking. This process acts as a stress relief mechanism during folding, and allows the material to reach very high curvatures, which makes them particularly interesting as components of space deployable structures. The goal of this study is to characterize the behavior and understand the mechanics of this type of composite.

Experimental testing of the bending behavior of unidirectional composites with a silicone matrix shows a highly non-linear moment vs. curvature relationship, as well as strain softening under cyclic loading. These effects are not usually observed in composites with an epoxy matrix. In the case of tension in the direction transverse to the fibers, the behavior shows again non-linearity and strain softening, as well as an initial stiffness much higher than what would be expected based on the traditional estimates for fiber composites.

The micro mechanics of the material have been studied with a finite element model. It uses solid elements and a random fiber arrangement produced with a reconstruction process based on micrographs of the material cross section. The simulations capture the macroscopic non-linear response, as well as the fiber microbuckling, and show how microbuckling reduces the strain in the fibers. The model shows good agreement for the bending stiffness of specimens with low fiber volume fraction, but it overestimates the effect of the matrix for more densely packed fibers. This is due to the high matrix strain that derives from the assumption of perfect bonding between fiber and matrix. In the case of tension transverse to the fibers, the model shows a much better agreement with experiments than traditional composite theory, and shows that the reason for the observed high stiffness is the incompressibility of the matrix. In order to capture the

strain softening due to fiber debonding, cohesive elements have been introduced between the fibers and the matrix. This allows the model to capture quantitatively the non-linear behavior in the case of loading transverse to the fibers, and the damage due to cyclic loading. A single set of parameters for the cohesive elements produce good agreement with the experimental results for very different values of the fiber volume fraction, and could also be used in the analysis of more complicated loading cases, such as bending or biaxial tension.

In addition to the simulations, a homogenized analytical model has also been created. It extends previous analysis of composites with a soft matrix to the case of very thin composites. It provides a good qualitative description of the material behavior, and it helps understand the mechanics that take place within the material, such as the equilibrium of energy terms leading to a finite wave length, as opposed to microbuckling under compression.

Contents

List of Figures

List of Tables

Chapter 1

Introduction

1.1 Composite materials in deployable space structures

Composite materials are defined as those made from at least two or more constitutive materials which remain distinct at the microscopic level, as opposed to homogeneous combinations, such as alloys. The constituents are usually chosen so that the composite exhibits the best quality of each one. In practice, composite materials usually consist of a soft constituent, known as matrix or binder, and a reinforcement material which increases the overall stiffness of the composite.

Several materials found in nature are in fact composites. Wood, composed of cellulose fibers in a matrix of lignin, is probably the best known example, and many biological tissues consist of collagen fibrils embedded in a very soft hydrated-matrix. Man-made composite materials are also common in engineering applications. Examples of composite materials used in industrial applications include: concrete, the graphite-reinforced rubbers used to make tyres, and fiber composites, which are possibly the most widely used form of composite materials.

Fiber composites are composite materials in which the reinforcement component are fibers, embedded in a matrix of polymer, usually epoxy. Several type of fibers are used, the most common one being carbon fibers. The strength-to-weight and stiffness-to-weight ratio of carbon fiber composites make them very attractive to aerospace applications, to the point that the fuselage of the new Boeing 787 Dreamliner and Airbus A350 XWB will be mainly made of composites. Besides being used as rigid structural components, fiber

composites also play an important role in the design of deployable space structures.

Most space structures include elements that are deployed after launching. This can be achieved with two different types of architecture. The first one is based around stiff structural members connected by mechanical joints to allow their relative motion. An example of this approach is the deployable mast in Figure 1.1. The main limitations to these structures are their complexity, weight, and the fact that they need to be externally actuated.

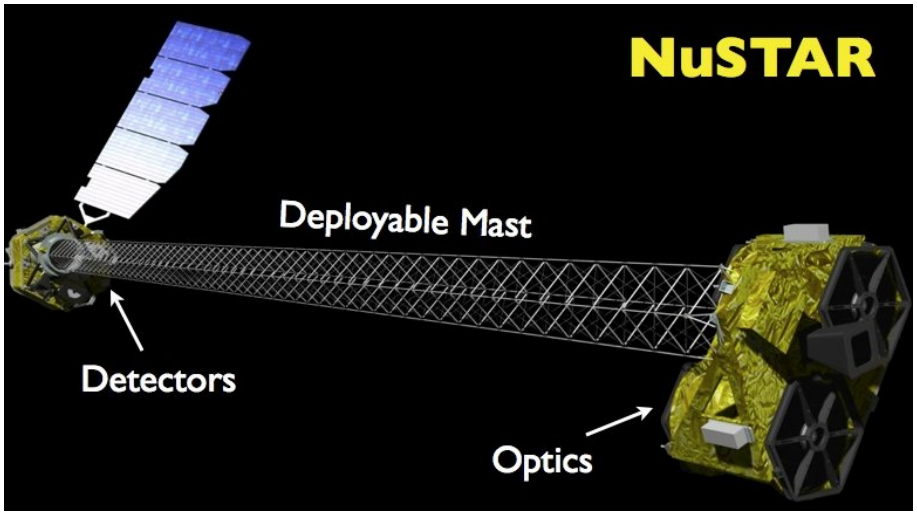

Figure 1.1: An artist's concept of the NuSTAR telescope showing the deployed mast, taken from NASA Science News (January 7 2010)

More recently, joint-less architectures have been proposed. In this case large relative motions between different parts of a structure are achieved by allowing the connecting elements to deform elastically. These designs are comparatively lighter, simpler, and do not require external actuation, since they use the stored strain energy of the structure to activate deployment. Some examples can be seen in Figure 1.2.

In this type of architecture it is common to use very thin elements, such as tape springs, working as hinges. These components become highly compliant when folded, and much stiffer when they are deployed. The maximum curvature of the folded hinge cannot exceed a limiting value that is related to the failure strain of the material. This is the main limitation on how tightly one can package structures based on this type of architecture. New designs have appeared in recent years for structures that require hinges that can achieve high curvatures and recover elastically (Mejia-Ariza et al., 2006; Rehnmark et al., 2007; Mejia-Ariza et al., 2010b). A possibility is the use of fiber composites with a very

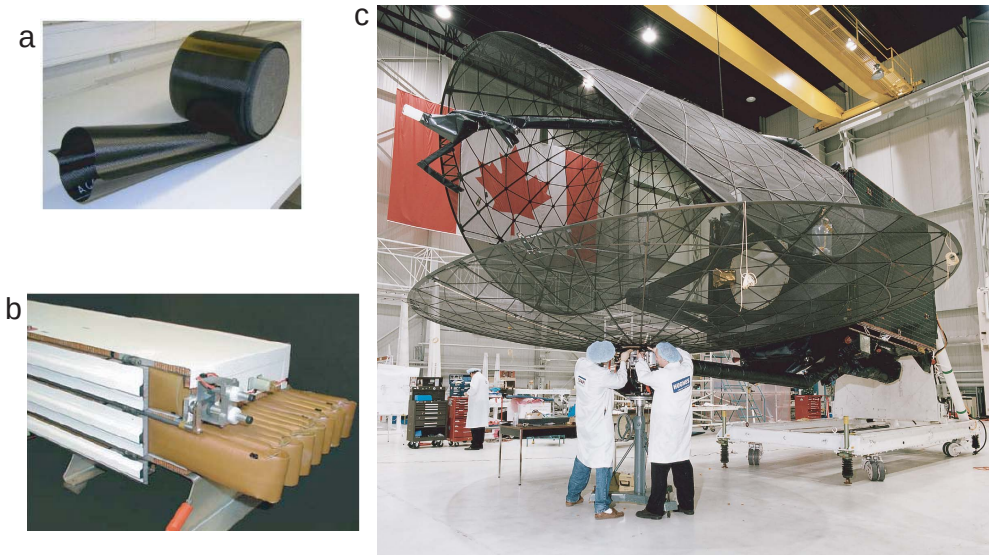

Figure 1.2: Examples of deployable space structures: (a) DLR-CFRP boom, German Aerospace Center (Leipold et al., 2005), (b) Northrop Grumman Astro Aerospace Flattenable Foldable Tubes for the Mars Express (Adams and Mobrem, 2009), and (c) Boeing springback reflectors on the Mobile Satellite System (Tan and Pellegrino, 2006)

soft hyperelastic matrix, such as silicone or rubber. These composites can be folded to very high curvatures while retaining their high tensile stiffness. The plot in Figure 1.3 shows the areal density vs. failure curvature for thin shells of different materials, usually considered in the design of deployable structures Mejia-Ariza et al. (2010b). The thickness of each shell is calculated so that all of them have the same stiffness under tension, 10 kN/mm.

It must be noted that Figure 1.3 does not present a complete characterization of the materials. The analysis only considers unidirectional stiffness, while considering an isotropic shell would benefit alloys over composites. Also, important aspects such as compression stiffness are omitted, and would greatly depend on the geometry of the complete structure. However, it shows the potential of deployable structures based on fiber composites with a soft hyperelastic matrix.

1.2 Motivation

This thesis focuses on the mechanics of composites made with carbon fibers embedded in a silicone matrix. Fiber composite materials in which the fibers are bonded by a soft hyperelastic matrix, such as silicones and elastomers, are an attractive alternative

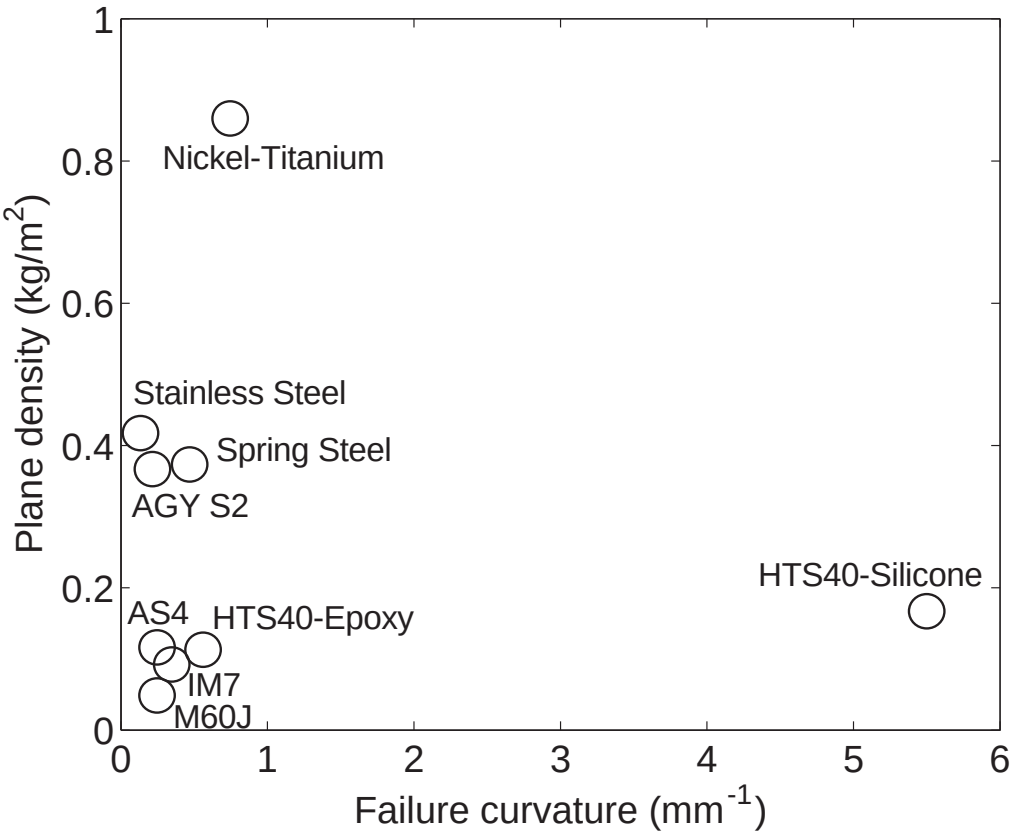

Figure 1.3: Areal density vs. failure curvature for thin shells with 10 kN/mm tensile stiffness: Torayca M60J carbon fiber composite, Hexcel IM7 carbon fiber composite, Hexcel AS4 carbon fibers in vinyl-ester resin at 50% fiber volume fraction, AGY S2 glass fiber composite, spring steel (ASTM A228), 304 stainless steel, superelastic nickel-titanium, HTS40 carbon fiber in epoxy at 60% fiber volume fraction, HTS40 carbon fiber in silicone at 30% fiber volume fraction. Material data taken from Mejia-Ariza et al. (2010b), except carbon fiber in silicone, for which the model in Chapter 6 has been used

for the design of deployable structures. Such materials can be folded to a much higher curvature than composites made with traditional epoxy. The reason is the capability of the fibers to move within the matrix. In particular, the fibers in the compression side of the material can buckle without breaking (see Figure 1.4). This process acts as a stress relief mechanism during folding (Campbell et al., 2004; Murphey et al., 2001; Francis et al., 2006; Francis, 2008).

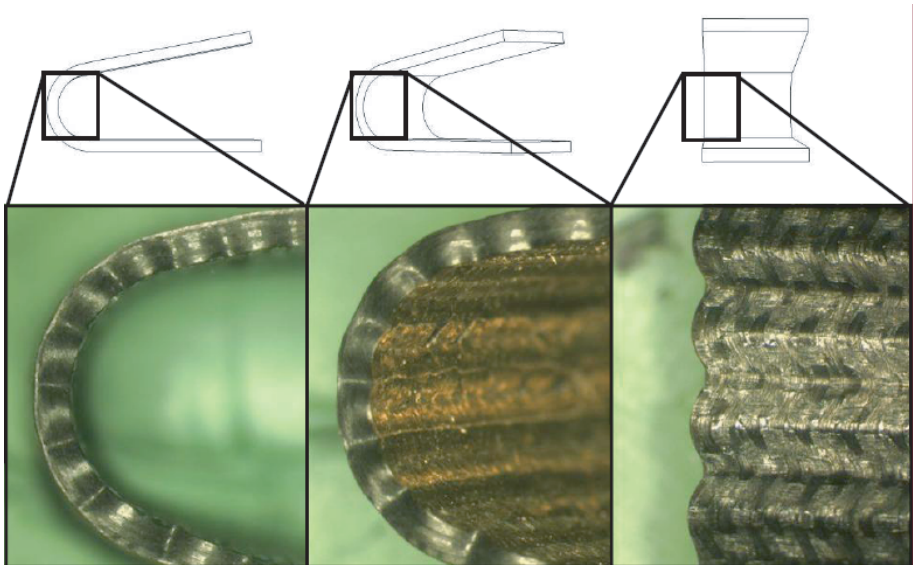

Figure 1.4: Bent elastic memory composite sample showing microbuckling of initially straight fibers. Taken from Francis (2008)

This new type of composite has already been used to build models showing exceptional folding capabilities (Datashvili et al., 2010; Mejia-Ariza et al., 2010a), such as the reflector shown in Figure 1.5. However, the micromechanics of the fibers are not properly understood yet. There are no numerical or analytical models able to predict the strain in the fibers, and therefore estimate the failure curvature. The mechanical response of the material has also not been studied. There is a particular need to analyze the bending stiffness, and the nonlinearities due to fiber microbuckling. Finally, even if these composites are able to undergo extreme folding deformations without catastrophic failure, some non-critical damage might be taking place in the material. These questions need to be addressed before this type of composite can be used in the design of space structures.

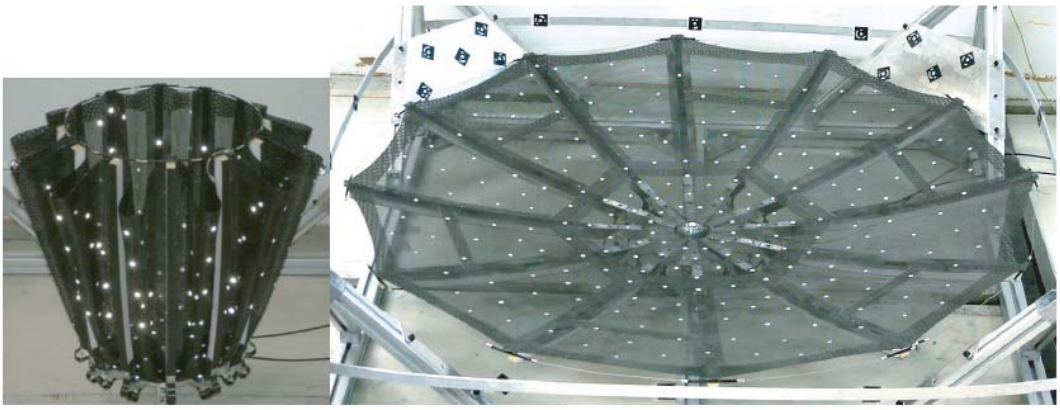

Figure 1.5: SMART demonstrator with an umbrella-like deployment scheme, folded and deployed (Datashvili et al., 2010)

1.3 Outline

The layout of the thesis is as follows. Chapter 2 reviews the relevant background to the problem studied. Special attention is paid to three different topics: mechanics of fibers in a hyperelastic matrix, fiber microbuckling, and stress softening of filled rubbers. The most relevant theories are presented, and their relation to the present work addressed.

Chapter 3 describes the materials used in this study, and the specimen fabrication techniques. Special care is taken to produce a proper characterization of the fiber distribution within the material, since it will be used to build the finite element model of Chapter 4. The experimental results are then presented. The response to tension in the direction along the fibers is dominated by the fiber's properties, and does not differ from traditional composites with epoxy matrix. The situation is different when bending or tension perpendicular to the fiber direction is applied. In this case, the material shows a highly nonlinear behavior, as well as stress softening.

Chapter 4 presents the finite element models used to study the micromechanics in the material: a three-dimensional model for folding, and a two-dimensional model to study the loading transverse to the fibers. Both of them use representative volume elements (RVEs) with periodic boundary conditions. Three different types of fiber arrangements have been used: a hexagonal lattice, a purely random arrangement, and a random arrangement based on the fiber distribution observed in micrographs of the material, created with a

reconstruction algorithm. A parametric study of parameters such as the size of the RVE and the mesh refinement is also presented.

Chapter 5 contains the numerical results. In the case of bending, the material presents a good quantitative prediction in the case of low fiber volume fractions. When the volume fraction is high the model captures the qualitative behavior, but overestimates the stiffness. The two-dimensional predictions for loading transverse to the fibers provide a good approximation of the linear stiffness. Cohesive elements are introduced to capture the strain softening due to fiber debonding. This makes it possible to model also the nonlinear response after the initial regimen.

Chapter 6 presents an analytical study of the bending properties of the material. This work extends some of the results presented in Chapter 2 to the particular case of very thin fiber-reinforced hyperelastic solids.

Chapter 7 presents a discussion on the results, as well as concluding remarks. Finally, Appendix A details some of the options used in the numerical simulations, and Appendix B contains a detailed analysis of the fiber folding test in Section 3.1.1.

Chapter 2

Background

There are three main differences between epoxy and silicone fiber-reinforced composites that will be addressed in this work. This chapter will provide a review of relevant studies regarding the three of them.

The first difference is the nonlinear behavior of finitely deformed fiber composites. Several large strain models have been used to study the mechanics and stability of composites under large deformations.

The second one is the fact that the low elastic modulus of the silicone allows the fibers to microbuckle without breaking, as they do with epoxy matrix. In particular, the fibers are able to buckle when the material is folded. This stress relief process has been studied in the case of elastic memory composites, but the mechanics are not properly understood yet, especially regarding the nonlinear post-buckling behavior.

Finally, fiber-reinforced rubbers present stress softening, commonly known as Mullins effect. This is a progressive damage process typical of particle-reinforced rubbers, which reduces the stiffness of the material as the applied strain is increased.

2.1 Large strain mechanics of fiber-reinforced composites

There are several large strain formulations for fiber reinforced composites. Several of them make use of the work of Spencer (1972), who showed that for an elastic material without internal constraints the most general strain-energy function for a homogenized transversely isotropic nonlinear elastic solid depends only on the first five invariants. The

first three, I_1, I_2, and I_3, are the usual invariants of $\mathbf{C} = \mathbf{F}^T\mathbf{F}$, where $\mathbf{F}$ is the deformation gradient

$$I_1 = tr\mathbf{C} \tag{2.1}$$

$$I_2 = I_3 tr(\mathbf{C}^{-1}) \tag{2.2}$$

$$I_3 = det\mathbf{C}\ . \tag{2.3}$$

The other two invariants, I_4 and I_5, are defined using the unit vector A, which defines the direction of anisotropy given by the fiber reinforcement in the undeformed configuration

$$I_4 = \mathbf{A}(\mathbf{CA}) = \mathbf{aa} \tag{2.4}$$

$$I_5 = \mathbf{A}(\mathbf{C}^2\mathbf{A}) = \mathbf{aBa} \tag{2.5}$$

where $\mathbf{a} = \mathbf{FA}$, that is, the direction of fiber reinforcement in the deformed configuration.

It is clear from the definition that I_4 is the square of the deformation in the direction of the fiber, i.e., the stretch of the fibers. I_5 does not have a clear physical meaning, but it can be shown that

$$I_5 = I_1 I_4 - I_2 + \mathbf{A}(\mathbf{C}^*\mathbf{A}) \tag{2.6}$$

where $\mathbf{C}^* = I_3\mathbf{C}^{-1}$ is the adjugate of $\mathbf{C}$. The final term in the equation can be interpreted as the square of the ratio of deformed to undeformed surface area, for an area element normal to $\mathbf{A}$.

This formulation was used by Triantafyllidis and Abeyaratne (1983) to study the material and geometric instabilities of unidirectional fiber-reinforced elastic materials under large deformations. In order to do so, the energy of the material was defined as the sum of an isotropic component and an anisotropic term taking into account the contribution

of the fibers

$$W = W_{iso}(I_1, I_2, I_3) + W_{aniso}(I_4) \ . \tag{2.7}$$

The fiber contribution is modeled with the so-called standard reinforcing model

$$W_{aniso}(I_4) = \alpha \, (I_4 - 1)^m \tag{2.8}$$

where the anisotropy parameter α is positive, and the exponent m is usually particularized to 2.

This model was used to predict surface bifurcations due to compression in plane strain conditions, and it showed that the presence of fibers can weaken the material with respect to its stability. However, some of the results are not applicable to carbon fiber composites, since the values of the stretch used are well beyond the critical elongation of the fibers.

A similar approach was used by Merodio and Ogden (2002) to extend the analysis to instabilities different from fiber kinking, such as debonding, splitting, and matrix failure, using the result of Geymonat et al. (1993) relating macroscopic instabilities to the loss of ellipticity of the homogenized constitutive relationships. Two different ways to model the effect of the fibers were used by Merodio and Ogden: the standard reinforcing model, as well as an energy term function of I_5. The matrix was modeled as incompressible, which allowed simplification of the kinematics of the material. The work was extended to the case of a compressible matrix in Merodio and Ogden (2003).

Several biological materials fit the description of stiff fibers in a very soft matrix, and several models have appeared based on Spencer's approach. Holzapfel et al. (2000) modeled arterial walls as a combination of layers, each of them with two different sets of fibers, with initial direction given by the unit vectors $\mathbf{A_1}$ and $\mathbf{A_2}$. For this reason, the set of additional invariants required is now

$$\bar{I}_4 = \mathbf{A_1}(\bar{\mathbf{C}}\mathbf{A_1}) \tag{2.9}$$

$$\bar{I}_5 = \mathbf{A_1}(\bar{\mathbf{C}}^2\mathbf{A_1}) \tag{2.10}$$

$$\bar{I}_6 = \mathbf{A_2}(\bar{\mathbf{C}}\mathbf{A_2}) \tag{2.11}$$

$$\bar{I}_7 = \mathbf{A_2}(\bar{\mathbf{C}}^2\mathbf{A_2}) \tag{2.12}$$

$$\bar{I}_8 = (\mathbf{A_1}\cdot\mathbf{A_2})\mathbf{A_1}\cdot\bar{\mathbf{C}}\mathbf{A_2} \tag{2.13}$$

$$\bar{I}_9 = (\mathbf{A_1}\cdot\mathbf{A_2})^2 \tag{2.14}$$

where the $\bar{I}_9$ is a constant defining the initial geometry, and $\bar{\mathbf{C}}$ is obtained through the multiplicative decomposition into volumetric and deviatoric components

$$\mathbf{F} = \left(J^{\frac{1}{3}}\mathbf{I}\right)\bar{\mathbf{F}} \tag{2.15}$$

$$\mathbf{C} = \mathbf{F}^T\mathbf{F} = J^{\frac{2}{3}}\bar{\mathbf{C}} = J^{\frac{2}{3}}\bar{\mathbf{F}}^T\bar{\mathbf{F}}\ . \tag{2.16}$$

In this case the energy term due to the presence of the fibers is

$$W_{aniso}(\bar{I}_4, \bar{I}_6) = \frac{k_1}{2k_2}\sum_{i=4,6}\left(e^{k_2\left(\bar{I}_i-1\right)^2} - 1\right) \tag{2.17}$$

where $k_1 > 0$ is a stress-like material parameter and $k_2 > 0$ is a dimensionless parameter. The same procedure has been applied to model the cornea (Pandolfi and Manganiello, 2006), and modified to include the spatial dispersion of collagen fibril orientations (Pandolfi and Holzapfel, 2008) by defining the energy as

$$W_{aniso}(\bar{I}_4, \bar{I}_6) = \sum_{i=4,6}\frac{k_{1i}}{2k_{2i}}\left(e^{k_{2i}\left(\kappa_i\bar{I}_1+(1-3\kappa_i)\bar{I}_i-1\right)^2} - 1\right) \tag{2.18}$$

where $\kappa_i \in \left[0, \frac{1}{3}\right]$ is a parameter modeling the dispersion, and $k_{2i} > 0$ and $k_{1i} > 0$ are dimensionless and stress-like parameters, respectively, to be determined from mechanical

tests.

A different approach used to study fiber-reinforced hyperelastic materials is based on the second-order homogenization theory developed by Ponte Castañeda (2002). The results are still in development, see for example Lopez-Pamies and Ponte Castañeda (2006), Agoras et al. (2009), and Lopez-Pamies and Idiart (2010). This theory has been compared with numerical results in Moraleda et al. (2009a).

In all these studies, the loading is two dimensional, usually under the assumption of plane strain. This is due not only to the extreme complexity of the models, but also to the intended applications, mainly filled rubbers such as tires and biological materials. In particular, there is no analysis of behavior under bending.

2.2 Fiber microbuckling

The first analysis of fiber microbuckling is due to Rosen (1965), who used Timoshenko and Gere's solution for the buckling under compression of a beam on an elastic foundation (Timoshenko and Gere, 1936). It models the composite as a two-dimensional succession of fibers of thickness d at a distance $2c$ from each other. The analysis equates the change of strain energy of the material, ΔU, with the external work, ΔT

$$\Delta U = \Delta U_f + \Delta U_m = \Delta T \tag{2.19}$$

where ΔU_f and ΔU_m are the strain energies per unit width in the fibers and the matrix.

Each fiber is assumed to buckle in a sinusoidal pattern. The deflection v in the y direction, defined in the centroid of a fiber, is expressed as

$$v = a \sin\left(\frac{x}{\lambda}\right) \tag{2.20}$$

where λ is the wavelength.

Neglecting the shear and normal terms, the strain energy of the fibers can be expressed

as

$$\Delta U_f = \frac{\pi E_f d^3 a^2}{48\lambda^3} \tag{2.21}$$

where E_f is the elastic modulus of the fibers and the second moment of area of the fibers have been calculated per unit width.

Regarding the matrix, Rosen considered two options, the so called extension mode, in which the fibers buckle alternatively out of phase, with the matrix deforming in extension, and the shear mode, in which the fibers buckle in phase, shearing the matrix between them, see Figure 2.1.

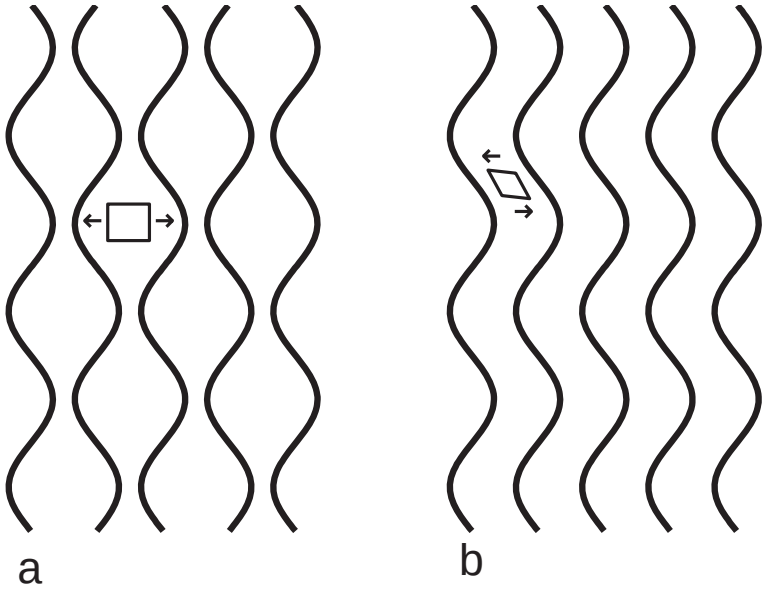

Figure 2.1: Schematic of fiber microbuckling: (a) extension mode and (b) shear mode

The shear mode is the one that requires lower energy, and so it is the one detailed here. The shear is assumed to depend only on the longitudinal coordinate x, which gives the form

$$\gamma_{xy} = \frac{\partial v}{\partial x} + \frac{\partial u}{\partial y} = \left(1 + \frac{d}{2c}\right) \frac{dv}{dx} \tag{2.22}$$

where the factor $\frac{h}{2c}$ takes into account the thickness of the fibers in the shearing deforma-

tion of the matrix, and the derivative $\frac{dv}{dx}$ is again taken in the axis of the fiber.

The strain energy of the matrix is therefore equal to

$$\Delta U_m = \frac{1}{2}\int_V \tau_{xy}\gamma_{xy}dV = G_m c\left(1+\frac{d}{2c}\right)^2 \frac{\pi a^2}{2\lambda} \tag{2.23}$$

where G_m is the shear modulus of the matrix.

Finally, the external work can be expressed as a function of the load carried by every fiber, σ_f, and the fiber deflection as

$$\Delta T = \frac{1}{2}\sigma_f d\int_0^\lambda \left(\frac{\partial v}{\partial x}\right)^2 dx = \frac{\sigma_f d\pi a^2}{4\lambda}\ . \tag{2.24}$$

Combining the three equations together, the critical stress is equal to

$$\sigma_{f_{cr}} = \frac{G_m}{V_f\left(1-V_f\right)} + \frac{E_f d^2}{12\lambda^2} \tag{2.25}$$

where V_f is the fiber volume fraction, $V_f = \frac{d}{d+2c}$.

The critical stress is minimized then the wavelength λ is much larger than the fiber diameter d, with an asymptotic value of

$$\sigma_{f_{cr}} = \frac{G_m}{V_f\left(1-V_f\right)}\ . \tag{2.26}$$

The homogenized critical load for the material as a whole is then equal to

$$\sigma_{cr} = \frac{G_m}{1-V_f}\ . \tag{2.27}$$

In his extensive work on composite failure, Fleck (1997) gives a value of the critical stress equal to

$$\sigma_{cr} = G + \frac{\pi^2 d^2 E}{3\lambda} \tag{2.28}$$

where E and G are the axial an in-plane shear moduli of the composite.

Fleck also establishes that the experimentally observed compressive strength is approximately equal to $\sigma_{cr} = \frac{G}{4}$. The reduction is due to imperfections, pre-existing fiber waviness, and plastic kinking.

The approach of treating the fibers as beams on an elastic foundation has been used in several other works that refined the approach of Rosen, studying the effect of factors such as material thickness, fiber volume fraction, and the type of load applied to the material (Drapier et al., 1996 1999 2001; Parnes and Chiskis, 2002).

The influence of fiber microbuckling for the flexural properties of a composite was studied by Marissen and Brouwer (1999). They calculated the reduction of flexural strength as a function of the ratio of tensile strength to critical buckling stress in the composite. Their work focuses only on the ultimate strength, since microbuckling is a failure mechanism in traditional composites, see Figure 2.2.

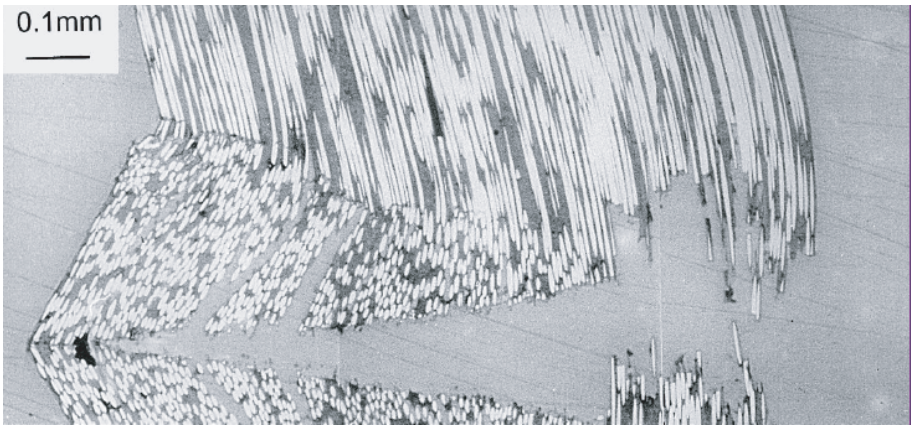

Figure 2.2: Micrograph of a unidirectional polyamide 66 glass-fiber composite, exposed to flexural creep load at enhanced temperature and humidity, provided by Jan van Lochem from KEMA Inspection Technology. Taken from Marissen and Brouwer (1999)

The situation is different if the matrix is soft and elastic enough to allow the fibers to deflect without breaking. Microbuckling can then act as a stress relieving mechanism, as it has been shown for the case of thermoplastic and elastic memory composites (Gall et al., 2000; Murphey et al., 2001; Campbell et al., 2004; Lan et al., 2009). Figure 2.3 shows a sketch of the process. When the folding starts, the bending stiffness is constant throughout the thickness of the material, and the neutral axis lies in the middle plane. As the fibers in the compression side reach the critical buckling load, their stiffness is reduced, according to the post-buckling mechanics of the fibers. This produces a bilinear

constitutive model, shifting the neutral axis from the middle surface to the tensile side of the laminate. This effect reduces considerably the maximum strain in the fibers, allowing for a much smaller radius of curvature. It should be noted that the buckling deflection has been depicted as out of plane for a better visualization. Experimental observations show that it occurs within the plane of the material, that is, parallel to the axis of rotation.

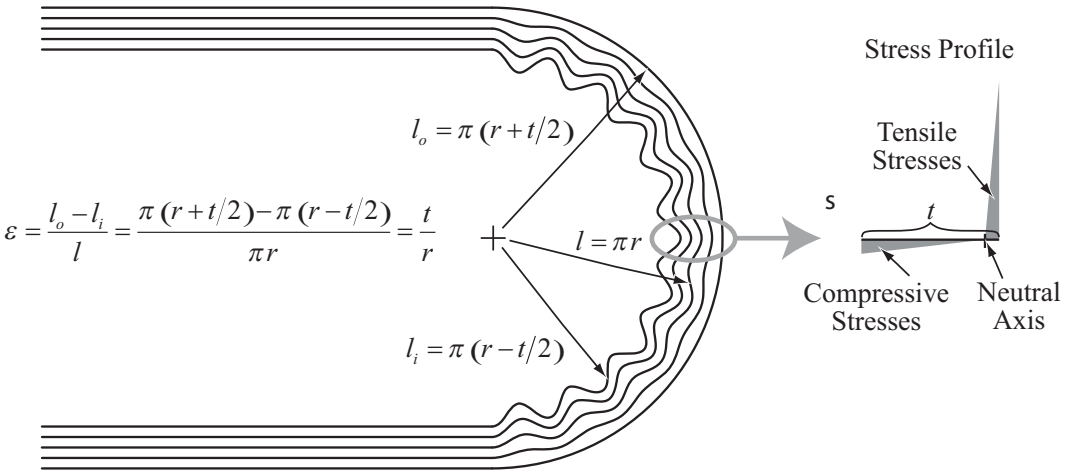

Figure 2.3: Fibre microbuckling and stress profile in a heavily bent laminate, taken from Murphey et al. (2001)

This effect has been studied by Francis (Francis et al., 2006; Francis, 2008), with an analysis similar to that of Rosen. The main difference is that the fiber deflection is not uniform through the material. Instead, it depends on the position of the fiber with respect to z, defined as the coordinate through the thickness. In order to calculate this dependence, it is assumed that the homogenized strain along the direction of the fibers, $\tilde{\epsilon}_x$, varies linearly through the composite thickness as a function of distance from the neutral surface according to Kirchoff's hypothesis. It can therefore be calculated with the usual expression

$$\tilde{\epsilon}_x = -\kappa(z - z_n) \tag{2.29}$$

where κ is the applied curvature and z_n the position of the neutral strain surface.

It is then assumed that the fibers stretch in the tensile side, while on the compression side the homogenized strain is accommodated by the fiber purely by microbuckling, with no fiber extension or compression. In this case, the strain needs to be expressed as

a function of the end shortening of a sinusoidal wave with constant arc length. The calculation involves an elliptic function of second order, but a good approximation is given by

$$\tilde{\epsilon}_x = -\left(\frac{\pi a}{2\lambda}\right)^2 . \tag{2.30}$$

Assuming that the wavelength λ is constant through the material, the sine amplitude a can be expressed as

$$a = \frac{2\lambda}{\pi}\sqrt{-\epsilon_x} = \frac{2\lambda}{\pi}\sqrt{\kappa(z - z_n)} . \tag{2.31}$$

The dependence of a with respect to z introduces a new shear component in the matrix, γ_{yz}. This deformation is produced by the difference in deflection of fibers with two different values of the z coordinate, and it can be approximated as

$$\gamma_{yz} = \frac{\partial v}{\partial z} = \frac{\kappa\lambda}{\pi\sqrt{\kappa(z - z_n)}} \sin\left(\frac{x}{\lambda}\right) . \tag{2.32}$$

The total strain energy in the material can now be expressed as

$$\Delta U = \Delta U_x + \Delta U_{xy} + \Delta U_{yz} + \Delta U_f \tag{2.33}$$

where ΔU_x is the strain energy of the unbuckled material (fibers and matrix), ΔU_{xy} and ΔU_{yz} are the strain energy terms of the matrix, and ΔU_f is the strain energy of the buckled fibers. Every energy term has a different dependence with respect to the buckle wavelength λ

$$\Delta U_{xy} \propto \frac{1}{\lambda} \tag{2.34}$$

$$\Delta U_{yz} \propto \lambda \tag{2.35}$$

$$\Delta U_f \propto \frac{1}{\lambda^3} . \tag{2.36}$$

Following the procedure of Rosen, the critical buckling stress will have, as before, a

constant component (due to ΔU_{xy}) and a component proportional to $\frac{1}{\lambda^2}$ (due to ΔU_f), but also a term proportional to λ^2 (due to ΔU_{yz}).

Therefore the case of non-homogeneous buckling differs from that studied by Rosen in the presence of an additional term in the expression of the critical stress, which increases with the fiber wavelength. The wavelength will be the value that minimizes the sum of all the terms, which is now finite. The value given by Francis is

$$\lambda = \frac{\pi}{2}\left(\frac{9V_f t^2 d^2 E_f}{8G_m \ln\left(\frac{6t}{d}\sqrt{\frac{V_f}{\pi}}\right)}\right)^{\frac{1}{4}} \tag{2.37}$$

where t is the thickness of composite plate being bent. Once the wave-length has been calculated, the amplitude of the buckled fibers can be calculated using Equation 2.31. The strain in the fibers can then be approximated as

$$\epsilon_f = \frac{d}{2}\kappa_f = \frac{d}{2}v'' = \frac{da\pi^2}{2\lambda^2} \tag{2.38}$$

where ϵ_f is given as an absolute value.

Similar studies have been performed with composite materials in which the matrix is silicone or very soft epoxy (Lopez Jimenez and Pellegrino, 2009; Mejia-Ariza et al., 2010a), always under the assumptions of linearized kinematics and linearly elastic material behavior for both fiber and matrix.

2.3 Stress softening in filled rubber

Experimental observations show that when a rubber filled with reinforcing particles is loaded in simple tension, unloaded, and then loaded again, the stress required on reloading is lower than that required on the initial loading. This stress softening is usually called Mullins effect, due to the extensive early measurements by Mullins. It is shown schematically in Figure 2.4. If a virgin material sample is loaded to the strain level (1), it follows the path (a), known as the primary loading curve. Subsequent unloading and

loading to state (1) will follow the path (b). The material has been weakened by the initial loading process, and its stiffness is reduced. If the strain exceeds (1), path (a) is followed again. If unloading from a higher strain level (2) occurs, it will create a new path (c) with a greater loss of stiffness.

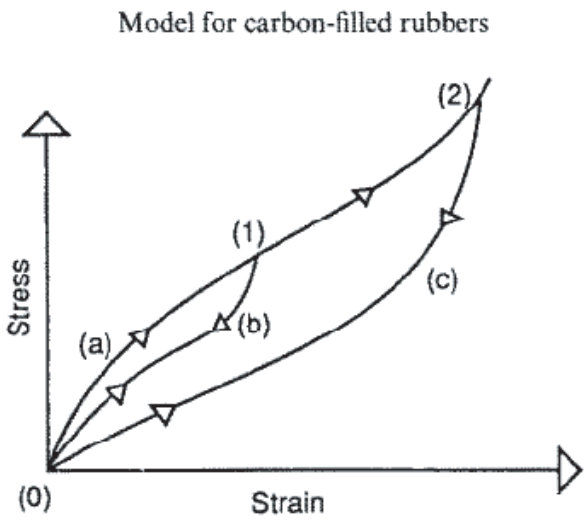

Figure 2.4: Typical schematic of cyclic tension demonstrating Mullin's effect. Taken from Govindjee and Simo (1991)

The process described above is the usual idealization of the phenomena observed experimentally, in which a reduction of stress takes place on each successive loading and unloading cycle. The reduction is largest between the first and second cycle, and it becomes very small after a few cycles, a process known as preconditioning. After those initial cycles, the stress-strain response is essentially repeatable. Representing the loading and unloading path as the same is also an idealization. There are large differences in the stress in both states, even in rubbers not showing hysteresis before being reinforced. All these phenomena depend on the concentration of particles in the rubber. In particular, both the softening and the hysteresis increase with the filler content. The experimental data in Figure 2.5 shows all these effects. Stress softening is not exclusive of rubbers, and can be found in other applications in which a reinforced matrix undergoes large deformations, such as discontinously reinforced metal-matrix composites and rocket solid fuel.

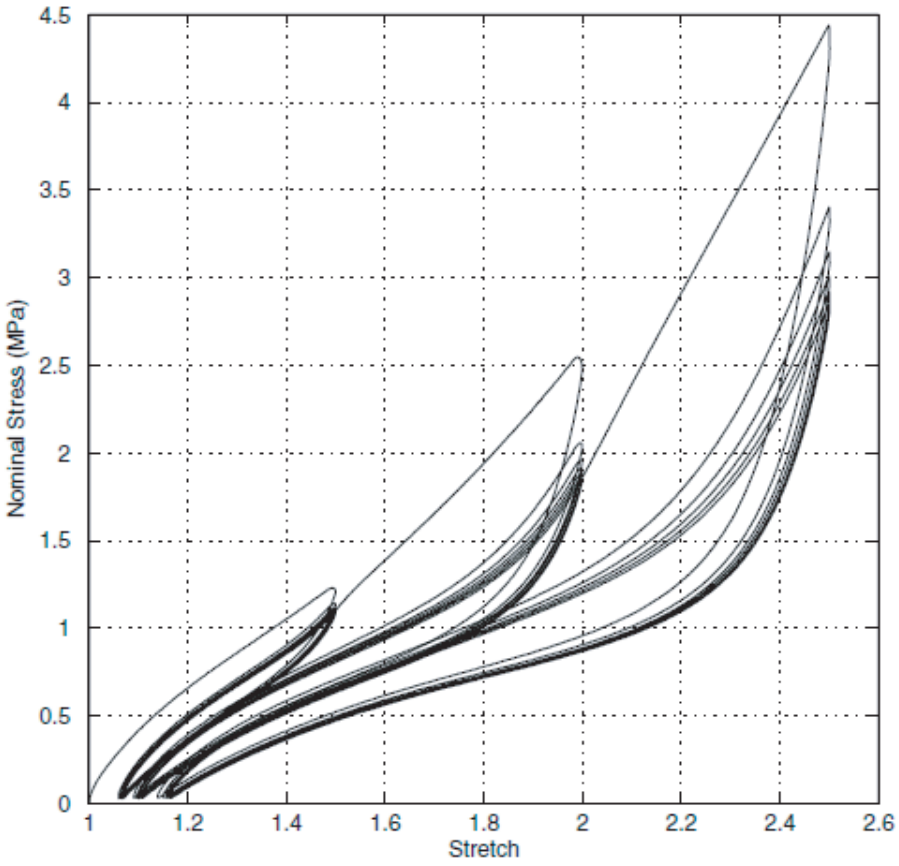

Figure 2.5: Periodic uniaxial extension tests of a particle-reinforced dumbbell specimen with 60 phr of carbon black with maximum stretches of $\lambda = 1.5$, $\lambda = 2$, and $\lambda = 2.5$. Taken from Dorfmann and Odgen (2004)

Several physical explanations have been proposed, including debonding, molecules slipping, rupture in the filler particles, disentanglement of polymer chains, or crystallization of rubber due to stress concentrations. See Diani et al. (2009) for a review on different failure mechanisms, as well as the types of model proposed, some of which are presented here.

Govindjee and Simo (1991) presented a homogenized model in which damage is incorporated through statistical mechanics of polymer networks, applied in this case to carbon black filled rubbers. It makes use of the phenomenological damage models proposed by Simo (1987), and shows good agreement with experiments.

Ogden and Roxburgh (1999) proposed a pseudo-elastic model in which the potential energy of the rubber, which is usually defined as a function of only two of the three principal stretches, λ_1, λ_2, with the third stretch expressed in terms of the other two due

to incompressibility, is now given by:

$$W\left(\lambda_1, \lambda_2, \eta\right) = \eta \tilde{W}\left(\lambda_1, \lambda_2\right) + \phi\left(\eta\right) \tag{2.39}$$

where $\tilde{W}$ is the potential of the virgin material, η is a scalar variable that keeps track of the damage in the material, and ϕ, known as the damage function, is a correction to the potential.

In a primary loading, that is, when the applied strain is increasing, $\eta = 1$ and $\phi(1) = 0$. Otherwise $0 < \eta < 1$ and ϕ needs to satisfy the conditions:

$$\phi'\left(\eta\right) = -\tilde{W} \tag{2.40}$$

$$\phi''\left(\eta\right) < 0\ . \tag{2.41}$$

The functions chosen by Ogden and Roxburgh are:

$$\eta = 1 - \frac{1}{r}\mathrm{erf}\left(\frac{1}{m}\left(W_m - \tilde{W}\right)\right) \tag{2.42}$$

and

$$-\phi'(\eta) = m\,\mathrm{erf}^{-1}\left(r\left(\eta - 1\right)\right) + W_m \tag{2.43}$$

which does not need to be integrated explicitly, and where m and r are positive parameters, and W_m is the maximum value of $\tilde{W}$, that is, the value for which $\eta = 1$. The values of m and r do not have a physical interpretation, and should be obtained by fitting to experimental data.

This model is implemented in Abaqus as one of the available hyperelastic potentials. It was modified by Dorfmann and Odgen (2004) to include permanent deformation, introducing an additional scalar η_2. This approach is similar to the one followed by Beatty and Krishnaswamy (2000).

Bergström and Boyce (1998) provided test of filled rubbers in compression, in which the time-dependent behavior of the material was studied combining loading tests with different strain rates, and stress relaxation tests. The tests showed a clear viscoelastic behavior. They also presented a large strain model in which a decomposition analogous to the Standard Linear Solid is used. The model provides good agreement with the experimental data. However, the test showed that the behavior is also present in unfilled rubber, so it is not clear if the observations would apply to rubbers whose unfilled behavior is closer to the hyperelastic idealization. The time-dependency is usually neglected in other works.

Even if there is extensive work on the subject, the case of filled silicone rubbers has barely been addressed. Machado et al. (2010) presents experimental testing, as well as an analysis on the ability of different models to describe the materials' behavior. The work shows how models based on strain energy produce better results than those using elongations as variables to model the damage evolution. It should be noted that silicone rubber often does not show hysteresis or softening in the unfilled state (Meunier et al., 2008), and so some of the physical explanations proposed for the Mullins effect could not apply in this case.

Stress softening is observed in other materials with two or more components, such as biological tissue, particle-reinforced polymers, or pocket solid fuel. Tong and Ravichandran (1994) and Ravichandran and Liu (1995) provide expressions for the elastic properties of particle composites undergoing damage by dewetting. The results are in those cases limited to the linear response of the material.

Debonding has also been introduced in finite element analysis of the micromechanics of elastomeres reinforced with particles (Zhong and Knauss, 1997 2000) and fibers (Moraleda et al., 2009b). The results show good qualitative agreement with the behavior observed experimentally.

Stress softening is also common in biological materials (Fung, 1972). It has been observed in different kind of tissues, such as blood vessels (Holzapfel et al., 2000) and the mussel byssus (Bertoldi and Boyce, 2007), which can be described as fiber-reinforced composites. This effect is attributed to a change of properties in the material when it is prepared for testing, and it is often eliminated by preconditioning the material, in an

attempt to reproduce the behavior the material would exhibit in vivo.

There are differences with engineering materials. While the response of fiber composites in the direction along the fiber is dominated by the fiber behavior and does not show stress softening, this is not the case in the case of biological materials, where the fibers can undergo much larger deformation. Several causes have been proposed to explain this effect, from plastic deformation of the fibers to the effect of the fiber microstructure, none of them applicable to carbon fiber composites.

Chapter 3

Experiments

There are not many experimental studies of carbon fiber composites embedded in a hyperelastic matrix. The few works providing quantitative results focused on the capabilities of the material to be folded without catastrophic failure, as well as small strain testing of the tension and bending stiffness (Francis et al., 2006; Francis, 2008; Mejia-Ariza et al., 2010a).

This chapter presents experimental testing of a composite material consisting of unidirectional carbon fibers embedded in a silicone matrix. The specimen fabrication and characterization process is detailed. The tests study the large strain behavior of the composite material under bending and tension, both along and transverse to the fibers. The response to tension in the direction along the fibers is dominated by the fiber's properties, and does not differ from traditional composites with epoxy matrix. In the other two cases the properties of the composite are dominated by the matrix (tension perpendicular to the fibers) or the interaction between fiber and matrix (bending). The behavior is then very different from that traditionally observed in fiber composites. In particular, the material shows a highly nonlinear behavior, as well as stress softening. This is in contrast with the linear behavior of traditional composites.

3.1 Materials

This section provides a description of the materials used during this study. The silicone has been characterized experimentally, while in the case of the fibers the only property calculated experimentally has been the failure curvature.

3.1.1 Fibers

The fibers used in this study are HTS40-12K, produced by Toho Tenax (retrieved August 2010). They were provided by Itochu Corporation, which processed the initial tows (bundles of continuous filaments) by spreading them. This produces a continuous layer of unidirectional fibers, called a ply, that is then rolled around a cylinder, from which it can be unrolled and cut in the required size. The surface density of the ply is equal to 40 g/m^2. This implies that the fibers corresponding to the original tows are spread on a region of approximately 20 mm width, although after the spreading the original tows cannot be distinguished. The properties of the fibers provided by the manufacturer are summarized in Table 3.1. No value was specified for the transverse elastic modulus or the Poisson's ratio of the fibers.

Fiber properties	
Diameter	7 μm
Tensile modulus	240 GPa
Density	1.77 g/cm^3
Failure strain	1.8 %
Matrix properties	
Viscosity (part A)	1300 mPa s
Viscosity (part B)	800 mPa s
Density	0.96 g/cm^3
Tensile modulus	0.8 MPa
Elongation at failure	100%

Table 3.1: Material properties according to the suppliers

The failure properties of carbon fibers are highly dependent on the existence of flaws (Donnet et al., 1998). The tensile strength shows variation along and between different filaments, and it is usually described with a Weibull distribution. The value of 1.8% for the critical elongation should only be used in the case of pure tension. In the case of bending, brittle materials can achieve higher maximum strains than in pure tension (Ashby and Jones, 1986). In order to characterize the failure curvature, tests were performed using the rig in Figure 3.1. A loop is formed with a bundle of about ten fibers, and then attached to the rig. The glass covering the fibers ensures that the loops do not transform. Rotating the screw increases the curvature in the fibers, until they break. The test is performed under a Nikon Eclipse LV100 microscope with a Nikon DS-Fi1 digital camera. A video of

the process is recorded, and then used to calculate the curvature of the fibers before they break.

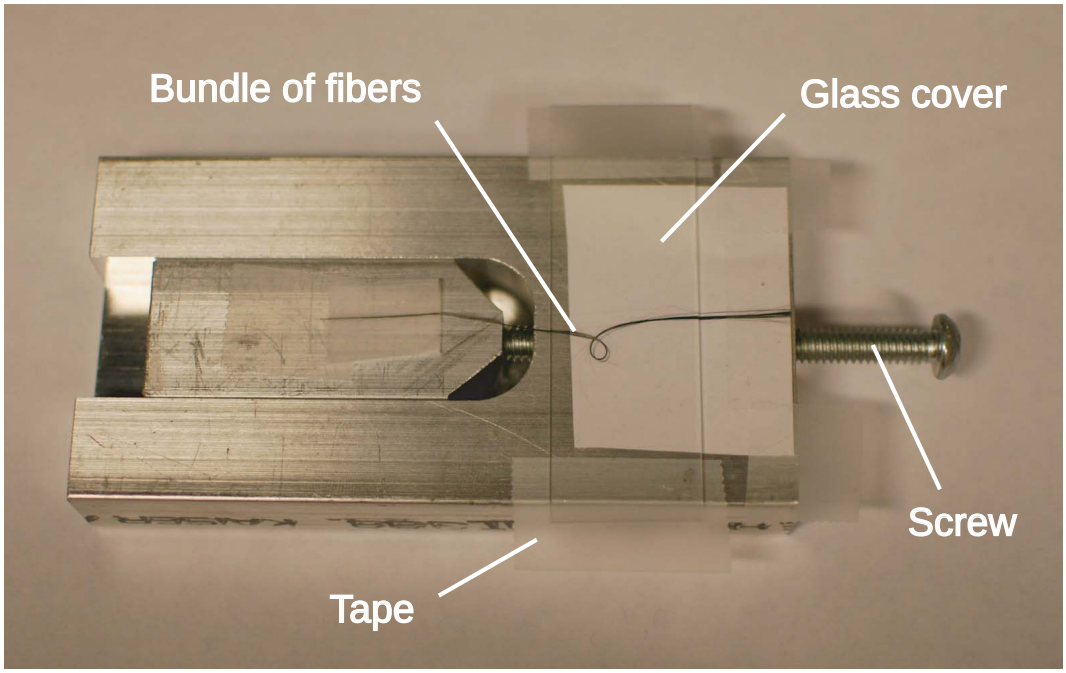

Figure 3.1: Rig used to measure the fiber curvature failure. The tape on the sides prevents the covering glass from touching the bottom surface, therefore allows the fibers to move freely

Figure 3.2 shows one of the frames recorded during the test. The portion of the fiber between Points A and B is assumed to be a cylindrical helix. The different out-of-plane coordinate at both points can be calculated by focusing the microscope at each point.

The resulting geometry is a helix, with curvature

$$\kappa = \frac{R}{R^2 + \left(\frac{H}{\pi}\right)^2} \tag{3.1}$$

where R is the curvature of the projected helix, and H the difference in height between points A and B. There is also a torsion component, given by

$$\tau = \frac{\left(\frac{H}{\pi}\right)}{R^2 + \left(\frac{H}{\pi}\right)^2} \, . \tag{3.2}$$

The torsion is at least one order of magnitude lower than the curvature in the fibers considered, and it is neglected.

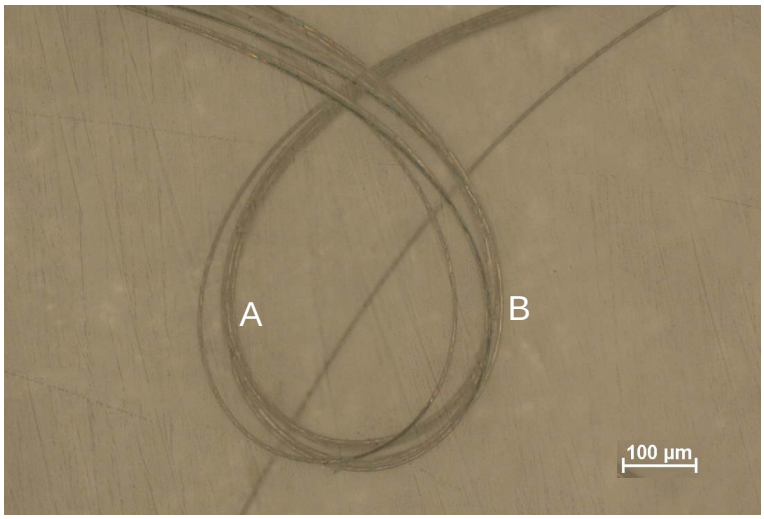

Figure 3.2: Bundle of looped fibers under the microscope, showing the two points A and B limiting the portion of the fibers considered in the analysis

An analysis of the stress conditions in the fiber has been performed using Euler's elastica theory, and can be found in Appendix B. It shows that the average axial strain is less than 0.002%, and so the fibers can be considered as being loaded in pure bending. The effect of friction can be neglected, since the region of the fiber with highest curvature is not touching the surfaces constraining it.

The test has been performed in several bundles, for a total of 105 fibers. The resulting curvatures are plotted in Figure 3.3. The vertical lines in the plot show the curvature for given maximum strains in the fibers. This result is important in cases when the fiber strain is mainly due to bending, such as fiber microbuckling.

3.1.2 Matrix

The matrix used is CF19-2615, produced by NuSil Silicone Technology (March 2007). It is a two-part, optically clear silicone. It has low viscosity (see Table 3.1), which facilitates its flow within the fibers. The modulus and elongation properties provided by the manufacturer were verified experimentally through uniaxial testing in a Instron 5569 testing machine with a 10 N load cell. The specimens were cut with a dog-bone shape to ensure that failure occurs away from the grips. The strain was measured with an Epsilon LEO1 laser extensometer. Two different sets of values were found (see Figure 3.4). For specimens cured in the autoclave, failure typically occurs at stretches $\lambda = 2.2 - 2.4$, with

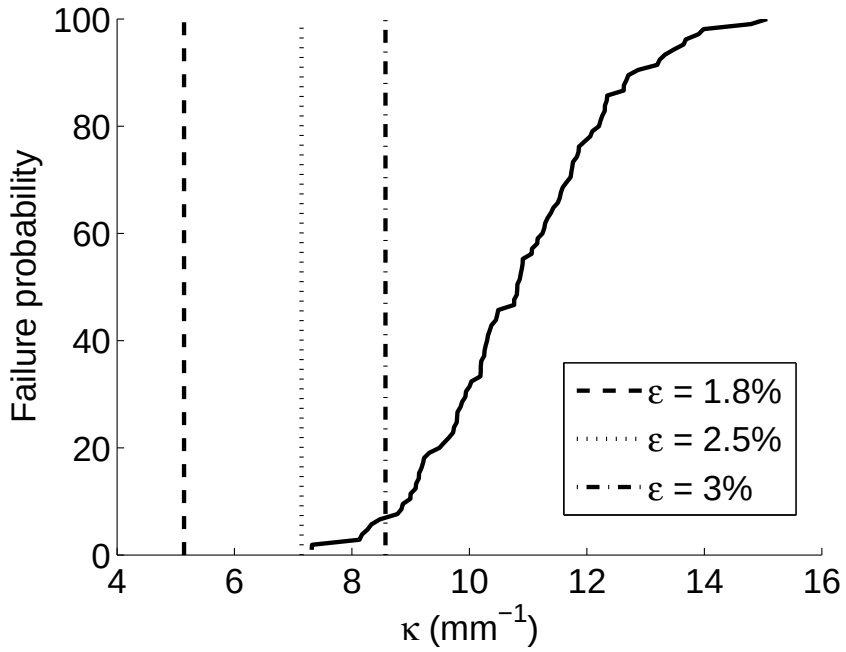

Figure 3.3: Probability of fiber failure as a function of curvature

a value of the Cauchy stress of approximately 1.25 MPa. For specimens cured in an oven, the values are $\lambda = 2 - 2.2$ and $1.7 - 2$ MPa, respectively. There are several factors that could affect or even poison the curing of the silicone. It is believed that in this case the reason for the difference in stiffness is the presence of epoxy residue in the autoclave, where traditional composites are often cured.

Figure 3.5 and Figure 3.6 show the results of a test conducted on two different sets of silicone, with the stress plotted as a function of stretch and time. The tests are a combination of cyclic and relaxation loading, showing negligible hysteresis or viscoelastic effects. This agrees with testing results of silicone rubber found in the literature (Meunier et al., 2008).

No failure criteria for silicone rubber under multi-axial loading conditions has been developed yet. There is also no information about cavitation, a failure process consisting of the sudden appearance of internal flaws, first described by Gent and Lindley (1959), which has been extensively studied in the case of filled rubbers (Gent, 1980; Gent and Park, 1984; Cho et al., 1987; Cho and Gent, 1988). For this reason, the value of the stretch at failure can not be readily applied to other loading conditions, but it will be used as an indication in the following chapters.

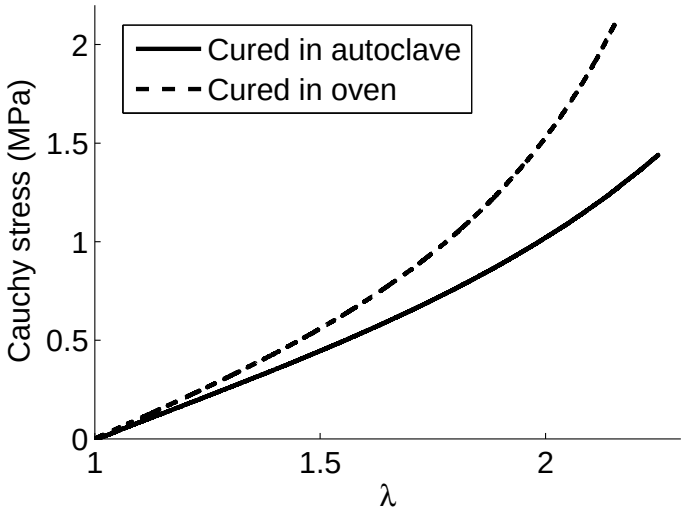

Figure 3.4: Uniaxial stress-strain relationship of CF19-2615 silicone. The two specimens are taken from the same batch of silicone, the only difference being the curing

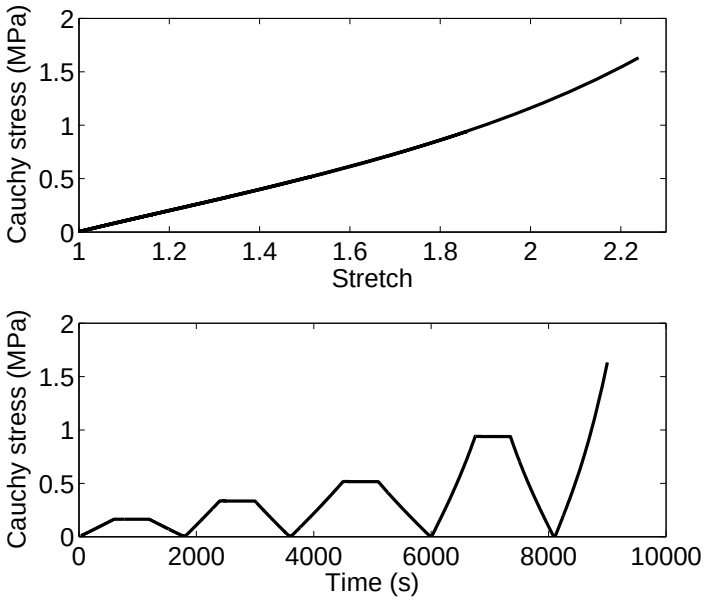

Figure 3.5: Uniaxial stress-strain and stress-time relationship of CF19-2615 silicone on a test consisting on cyclic loading with holding periods. Silicone cured in autoclave

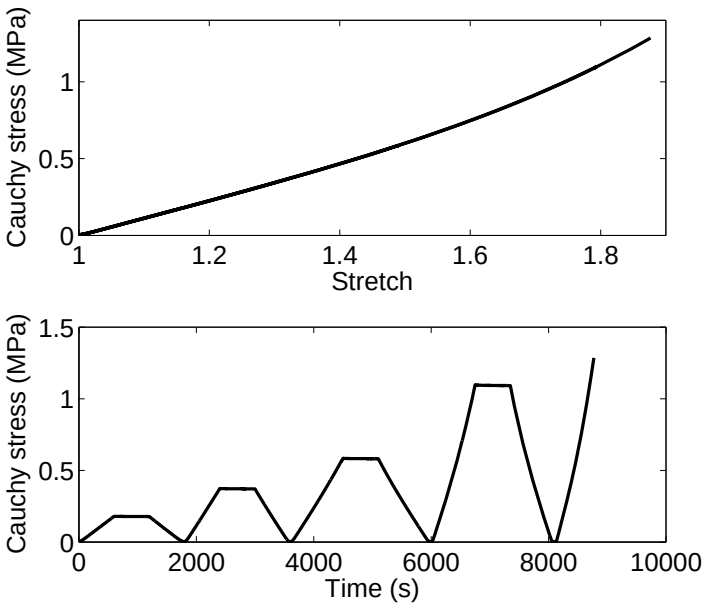

Figure 3.6: Uniaxial stress-strain and stress-time relationship of CF19-2615 silicone from a test consisting of cyclic loading with holding periods. Silicone cured in oven

3.2 Specimen fabrication

In the fabrication process, the two parts of the silicone are mixed, and vacuum is applied to extract air bubbles. The mixture is then poured over the fibers, previously placed on a Teflon-coated tray or a PTFE sheet, in order to avoid adhesion. The material is cured for 30 minutes at 150 °C, in either an oven or an autoclave. In the latter, the specimens are vacuum bagged, and internal vacuum and up to 85 psi (0.586 MPa) of external pressure were applied. This technique is able to vary the fiber volume fraction between 25% and 55% (see Figure 3.7). Holding the specimen under vacuum is the main contributor to achieving high quality specimens. Increasing the pressure differential has the advantage of better consolidating the fibers and also achieving a more homogeneous distribution of fibers in the matrix.

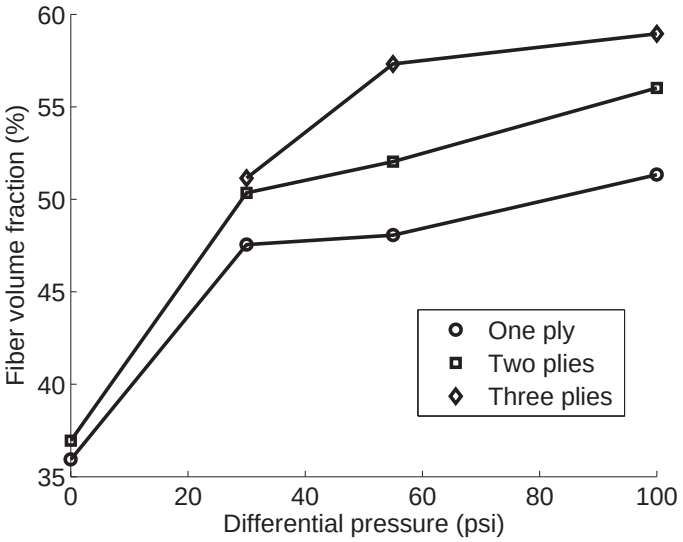

Figure 3.7: Average fiber fraction in the material vs. differential pressure applied during curing

The fiber volume fraction is fairly independent on the amount of silicone applied before curing. In composites cured in the autoclave, the differential pressure is enough to evacuate the extra silicone through a perforated release film. In specimens cured in the oven it is possible to decrease the volume fraction even further by applying an excess of silicone, but this does not result in a homogeneous distribution of the fibers. An extreme case (less than 10% volume fraction) can be seen in Figure 3.8; note that all the fibers are concentrated in a narrow section of the material and are surrounded by pure silicone. The local fiber volume fraction in the region containing the fibers is approximately 25%.

3.3 Specimen characterization

The simplest characterization of the microstructure of the composite is given by its fiber volume fraction, defined as

$$V_f = \frac{A_f}{A} \tag{3.3}$$

where A_f is the cross-sectional area of the fibers and A is the total area of the cross section, both as observed in the micrographs. However, additional information is necessary to

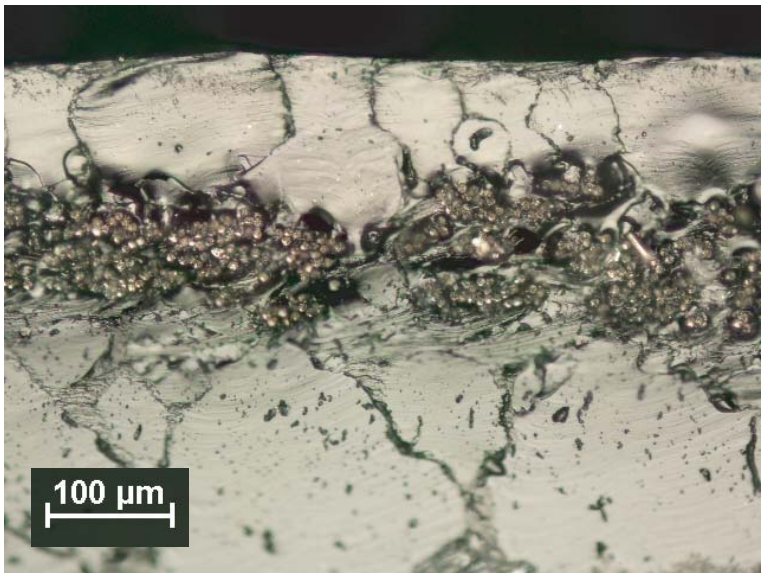

Figure 3.8: Example of specimen with different global and local fiber volume fraction

describe a particular fiber arrangement.

The real distribution of the fibers is different from the regular lattices that are sometimes used as an idealization in finite element and analytical modeling. In order to incorporate the random microstructure, it is necessary to use a fiber distribution that allows the simulations to capture the main behavior observed in the experiments.

The first step in this process is to obtain micrographs of the material cross section. This requires a very flat surface, which is traditionally achieved by embedding the specimen in epoxy, and then polishing it. However, this is not possible with a composite consisting of a very soft and highly elastic matrix. Instead, the material was cut with a razor and then placed directly under a Nikon Eclipe LV100 microscope with 50x amplification and a Nikon DS-Fi1 digital camera. The surface obtained this way is not sufficiently flat to lie entirely within the depth of field of the camera. In order to solve this problem, several pictures of the material are taken at different focus distances. The images are then processed with the focus stacking capabilities of Adobe Photoshop CS4 (Adobe Photoshop CS4, 2008), producing micrographs in which all regions are focused (see Figure 3.9).

The second and main step is then to obtain a function that characterizes the fiber distribution in the material with more detail than the volume fraction. Several studies have proposed parameterizations based on the Voronoi tessellation of the fibers (see Figure 3.10). The segments of the Voronoi diagram are all the points in the plane that are

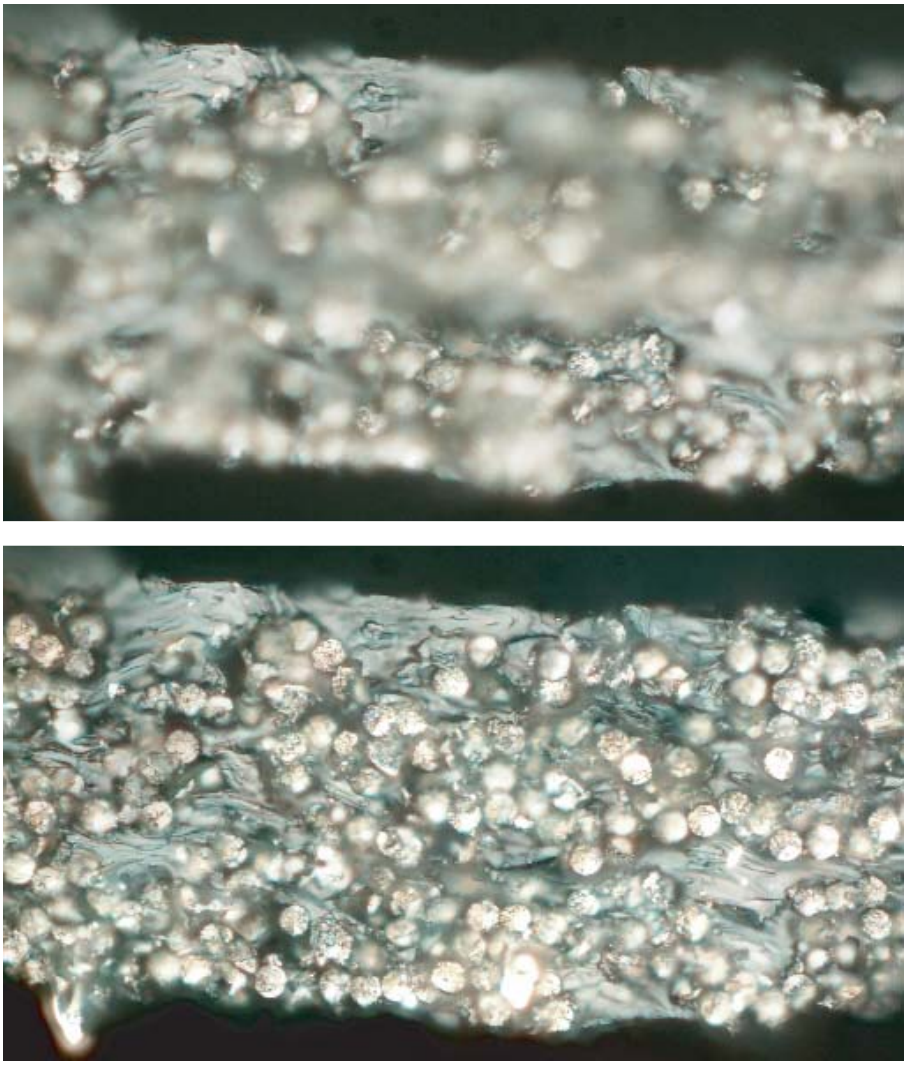

Figure 3.9: Original micrograph and final micrograph after stacking six images

equidistant to the two nearest fibers. Therefore, every cell contains all the points that are closer to the same fiber than to any other. The main limitation is that, in the case of thin composites, the Voronoi cells corresponding to fibers near the surface of the material extend to infinity.

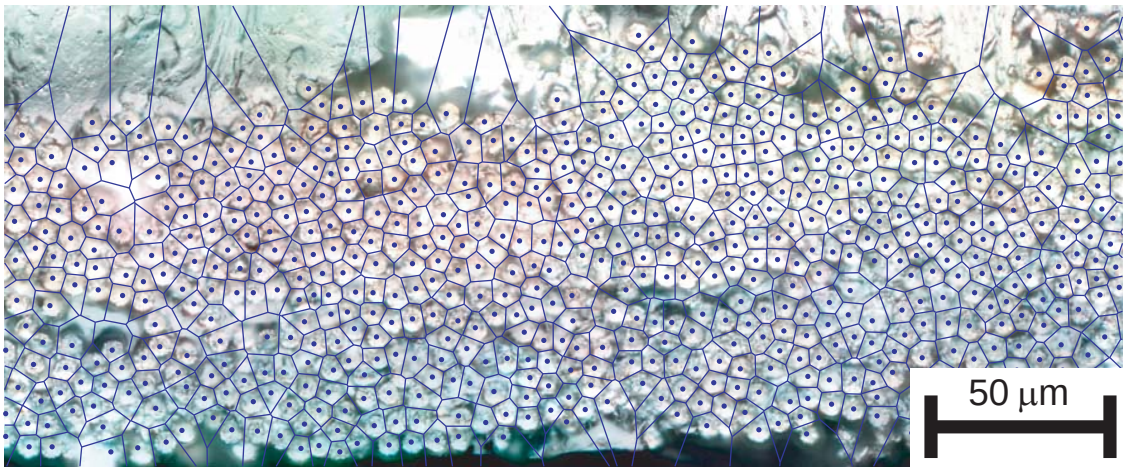

Figure 3.10: Micrograph showing the Voronoi tessellation of the fibers, obtained with the voronoi command in Matlab, with the centroid of the fibers given as an input

Davy and Guild (1988) used the distance from each fiber to the closest Voronoi segment as a measure to describe the fiber distribution obtained through a Gibbs hardcore process. Note that this is equivalent to using the distance to the closest fiber, which is just twice the value of the distance to the cell.

Pyrz and Bochenek (1998) employed the topological entropy of the Voronoi tessellation of the fibers as a function to describe the microstructure. It is defined as

$$S = -\sum_{n=1}^{k} p_n \log p_n \tag{3.4}$$

where p_n is the probability of finding a n-sided polygon.

The Voronoi tessellation can also be used to study with more detail the volume fraction. In particular, the difference between global and local volume fraction can be established by calculating the volume fraction of each of the Voronoi cells. Figure 3.11 shows its histogram, with the vertical line marking the average value (55%, for a three-ply specimen), which agrees with the value obtained from weight measurements. The figure shows how

the most common value of the volume fraction is in the 60%−65% range. The peak at very low volume fractions corresponds to fibers next to the surface of the material, which, as previously mentioned, have Voronoi cells that extend to infinity.

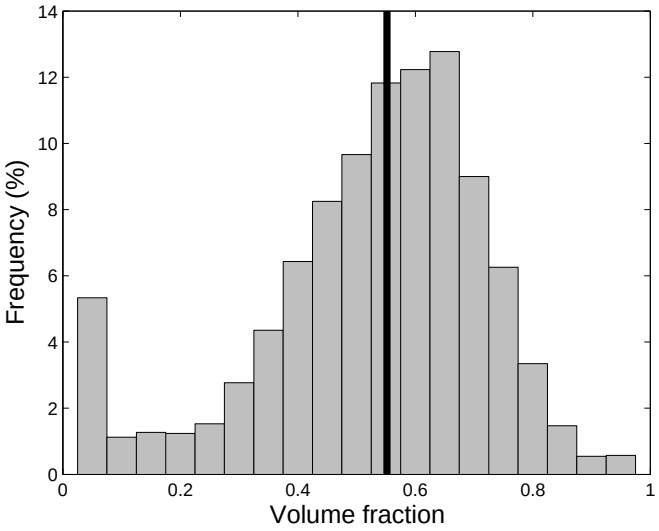

Figure 3.11: Histogram of the volume fractions of Voronoi cells produced from micrographs. The vertical line marks the average

Other works have modeled the properties of the microstructure using functions based on the position of the inclusions, such as the power spectral density of the indicator function (Povirk, 1995), an approach that has been followed to reconstruct microstructure which irregularly shaped inclusions. Rintoul and Torquato (1997) proposed the use of the radial distribution function (RDF), with basically measures the probability, given the position of a fiber, of finding another fiber in an annulus of radius r and $r+dr$ centered in the first one. The RDF is normalized so that it tends to one as the distance r approaches to infinity. This is not the case in the example presented here, since the fiber distribution only extends in one direction, due to the finite thickness of the specimen.

The function used in this work is the second-order intensity function $K(r)$ (Pyrz, 1994ab), defined as the average number of fibers expected to lie within a radial distance r from an arbitrary fiber, and normalized by the overall fiber density. If a section of area

A with N fibers is considered, $K(r)$ is calculated as:

$$K\left(r\right) = \frac{A}{N^2} \sum_{k=1}^{N} {w_k}^{-1} I_k\left(r\right) \tag{3.5}$$

where $I_k\left(r\right)$ is the number of fibers inside a center of radius r centered in the k-th fiber, and w_k is a factor introduced to correct for edge effects, equal the proportion of that circle contained in the area A. In practice, only the fibers sufficiently far away from the ends of the micrographs are considered, and so $w_k = 1$.

The second-order intensity function is proportional to the integral over the radius of the RDF, and so they provide the same information. Figure 3.12 shows the average number of neighbor fibers as a function of distance for samples with two different values of the fiber volume fraction, as well as the corresponding second-order intensity function.

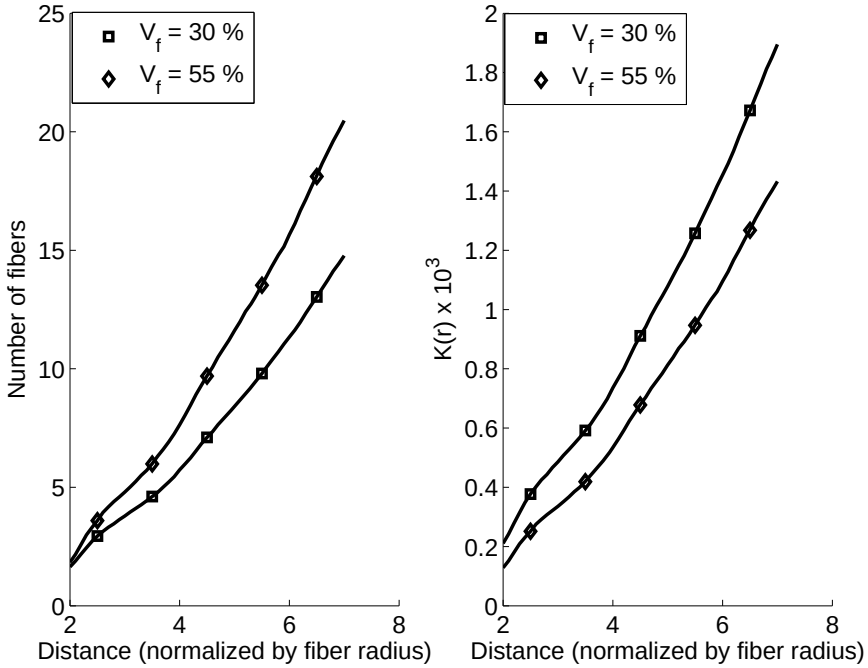

Figure 3.12: Statistical description of micrographs: (a) Average number of fibers as a function of distance to a given fiber and (b) second-order intensity function $K(r)$. The measurements are taken on one-ply specimens

The second-order intensity function will be used to produce finite element models with a fiber arrangement based on those of the real material, as detailed in Chapter 4.

This allows a more realistic comparison between experimental and numerical results. Five different sets of specimens were carefully characterized, in order to be used in both experiments and simulations: two one-ply set of specimens for the bending tests, with volume fractions equal to 30% and 55%, and three three-ply set of specimens for testing transverse tension, with volume fractions of 65%, 50%, and 22%. Note that the total amount of fibers per ply is the same in both cases. This means that, for a given number of plies, specimens with lower volume fraction have a higher thickness, but also lower homogenized longitudinal stiffness.

Figures 3.13 and 3.14 show the bending specimens. The fiber distribution is very regular in the material with 55% fiber volume fraction, while the specimens with 30% volume fraction show a combination of dense fiber clusters and large silicone areas.

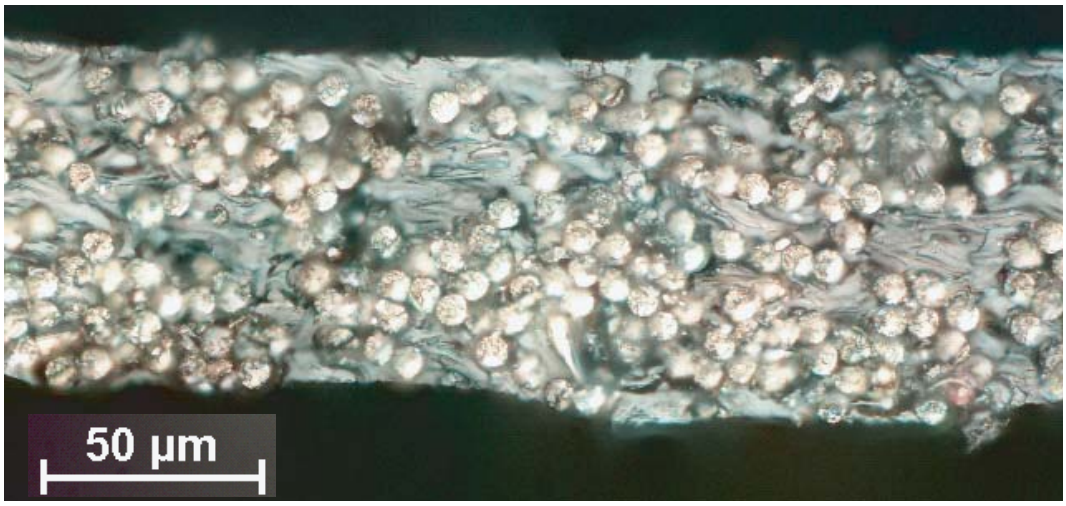

Figure 3.13: Specimen for bending tests, 30% volume fraction. The average thickness is 75 μm

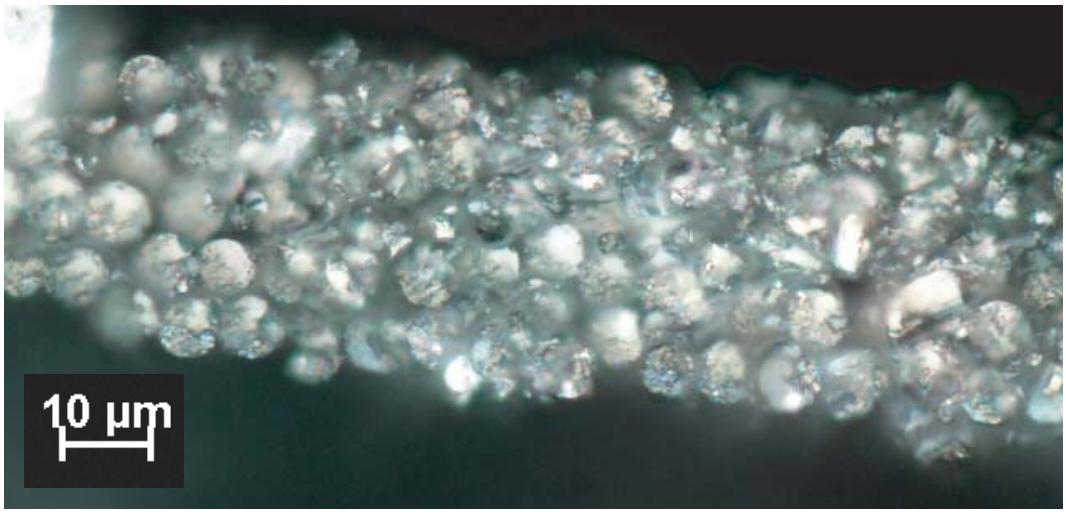

Figure 3.14: Specimen for bending tests, 55% volume fraction. The average thickness is 45 μm

The specimens used for loading transverse to the fiber direction have more than one ply. This achieved by applying silicone on one ply, and then extending the additional plies on top of the first one, making sure that the fibers of the two are aligned. It might be necessary to apply extra silicone, according to the initial quantity of uncured silicone applied, and the number of plies. Figure 3.15 and Figure 3.15 show micrographs of the two extreme cases used for loading transverse to the fibers, meaning those with 65% and 22% fiber volume fraction, respectively. The fiber distribution in the latter is very irregular, with high fiber clustering. Chapter 5 will show how this has an important effect on stress and strain concentrations.

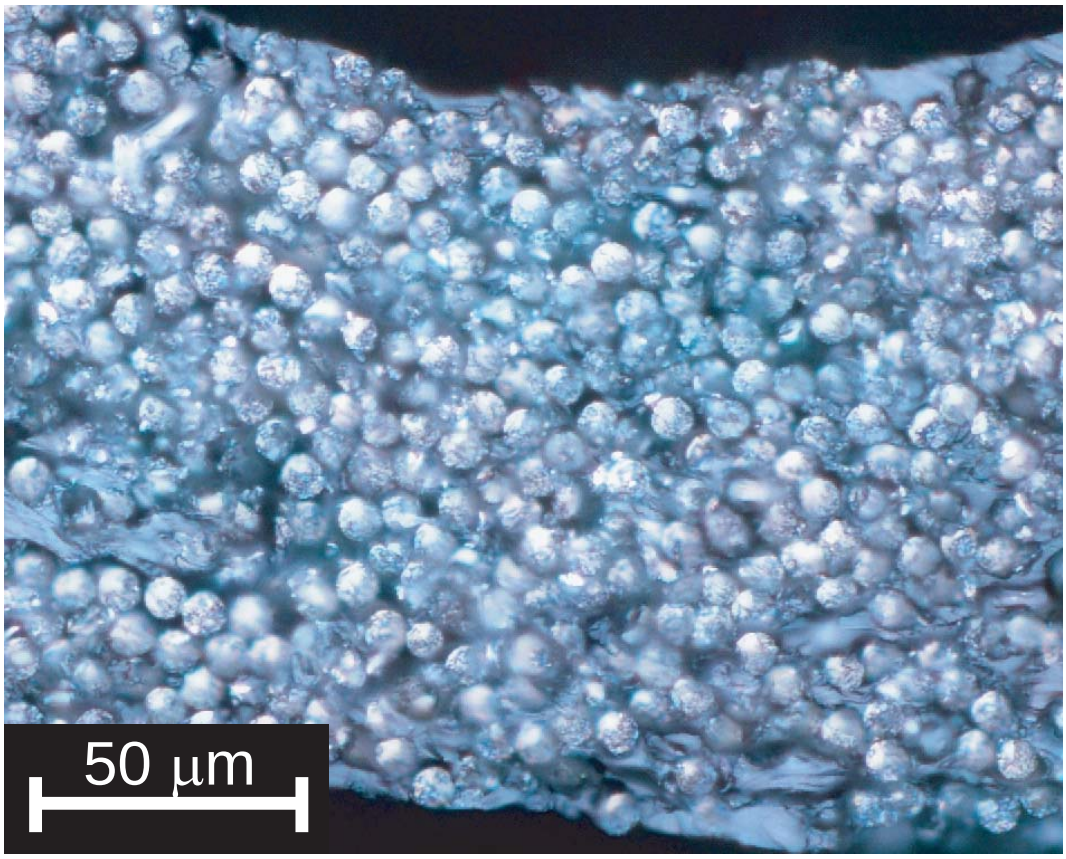

Figure 3.15: Specimen for transverse loading tests, three plies, 65% volume fraction. The average thickness is 150 μm

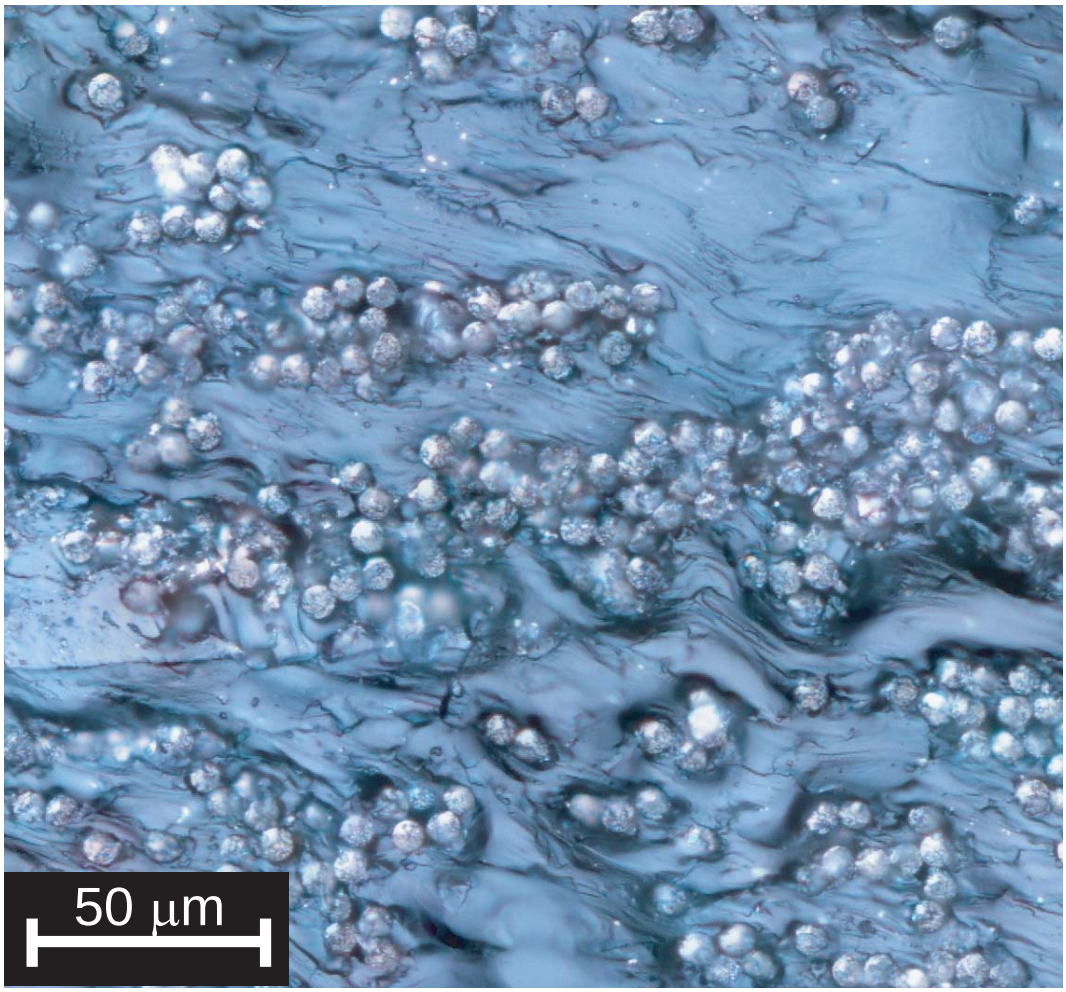

Figure 3.16: Specimen for transverse loading tests, three plies, 22% volume fraction. The average thickness is 300 μm

3.4 Tension along the fibers

The response to tension along the fibers is completely dominated by the fiber properties, and does not show significant differences with the response expected for composites with epoxy matrix. After an initial straightening, the elastic modulus of the composite can be predicted by adding the stiffness of all the fibers involved. This can be calculated since the number of fibers per unit width is known. The stiffness is independent of the fiber volume fraction, and the presence of the matrix can be neglected. Figure 3.17 shows the results of four load-unload cycles to increasing maximum strain. No change in the stiffness was observed between the cycles.

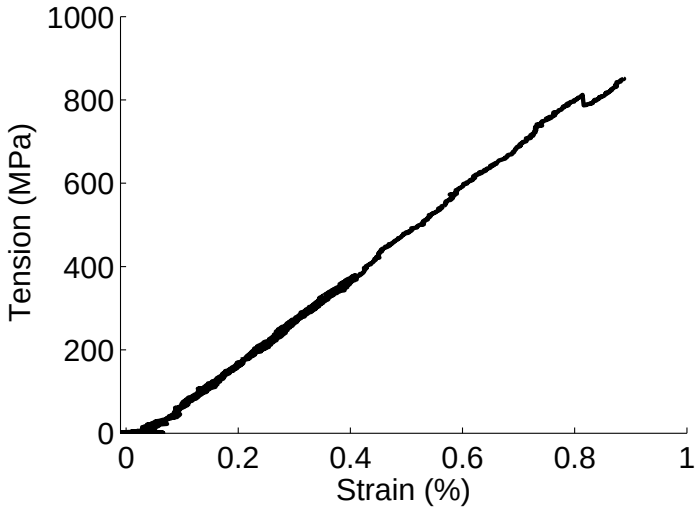

Figure 3.17: Stress vs. strain along the fibers. One-ply specimen, 50% volume fraction

The material could not be tested to failure due to the difficulty of holding the specimens properly. The grips used to test until failure have a saw pattern in the area of contact with the specimens, in order to provide the sufficient friction. This is enough to break specimens so soft in the direction perpendicular to the fibers as the ones studied here. In the case of epoxy composites, the standard practice consists of gluing metal tabs to protect the specimen. In this case, however, the tabs can not be attached firmly to the silicone. Testing was possible using grips with a flat surface of contact with the specimen, but the specimen started slipping before failure took place. An alternative able to reach higher strains consisted of using the grips with saw pattern, protecting the specimens with a layer of emery cloth. This allowed reaching a strain of approximately 1% before slipping started, as seen in Figure 3.17. The material is expected to fail when it reaches, at most, the failure stretch of the fibers, established by the manufacturer at 1.8%.

It is also difficult to observe the complete stiffness of the material early in the test. Due to the low transverse stiffness of the specimens it is not possible to make sure that they are completely flat at the beginning of the test. The stiffness increases asymptotically as the specimen straightens (see Figure 3.17).

3.5 Bending

3.5.1 Folding test

In order to observe the material while being folded, several specimens were held in a 90° kink angle, with a radius of curvature of approximately 2 mm. Figure 3.18 and Figure 3.19 show the tension and compression side of specimens with 30 and 55% fiber volume fraction, respectively. Micro buckling can be observed in both cases, although it is more regular and noticeable in the case with lower volume fraction. The buckles appear in both compression and tension side, although the amplitude is higher in the compressed fibers. This agrees with the simulation results shown in Chapter 5. The existence of buckled fibers on the tension side is typical of very thin composites, and does not happen in the case of thicker specimens (Francis, 2008).

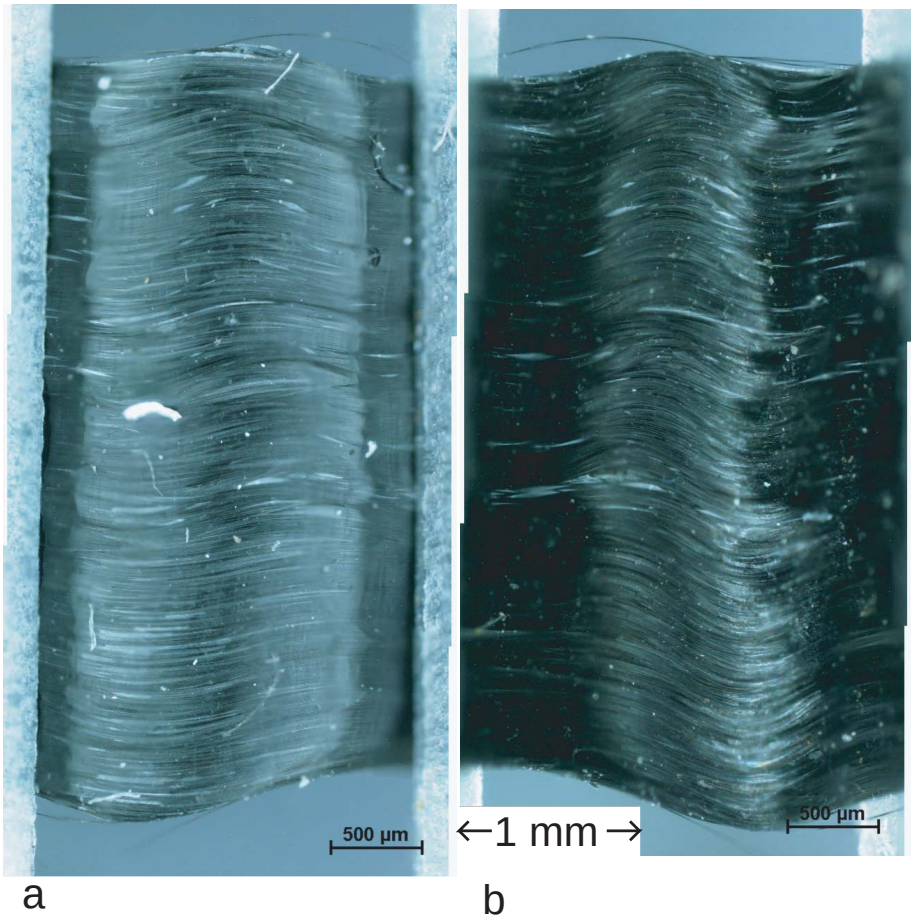

Figure 3.18: Specimen folded 90° with a 2 mm radius and 30% volume fraction: (a) tension side and (b) compression side

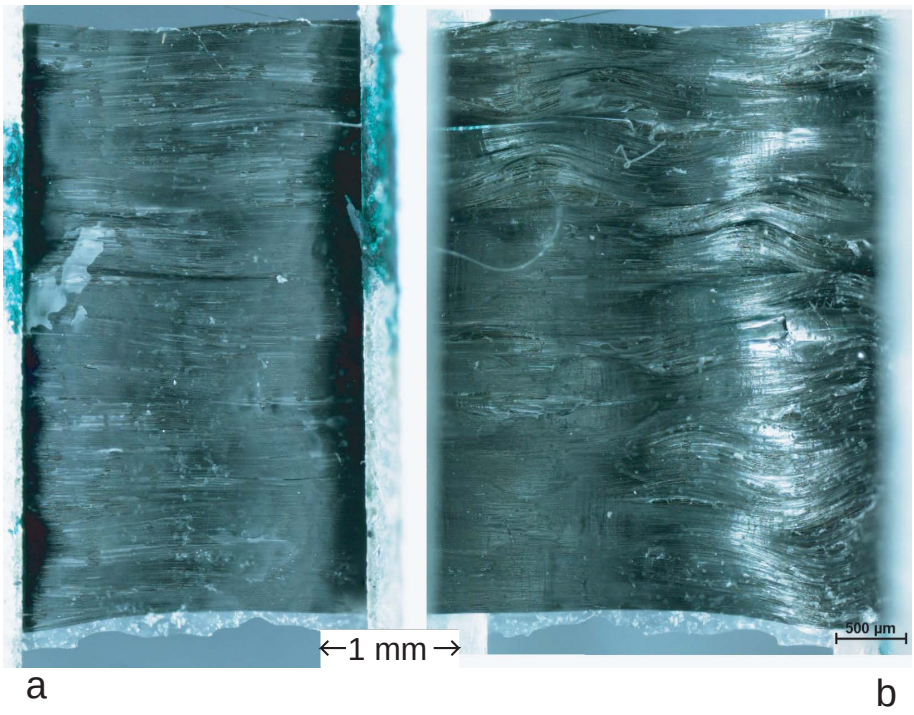

Figure 3.19: Specimen folded 90° with a 2 mm radius and 55% volume fraction: (a) tension side and (b) compression side

3.5.2 Bending test setup

Standard methods to measure the bending stiffness, such as the four-point bending test, are limited to relatively stiff specimens that undergo only small curvatures. In order to measure the nonlinear moment-curvature relationship at larger curvatures a different technique is required. In the method used in this study, the moment-curvature relationship was obtained from the post-buckling behavior of specimens under compressive load.

9-to-15 mm-wide composite specimens were sandwiched between 0.6-mm-thick aluminium-alloy plates. The plates were glued to the specimens with Instant Krazy Glue, leaving a 4 mm distance between the two pairs of plates, see Figure 3.20. The sandwiched ends of these specimens are much stiffer than the composite-only strip in the middle and they can therefore be idealized as rigid.

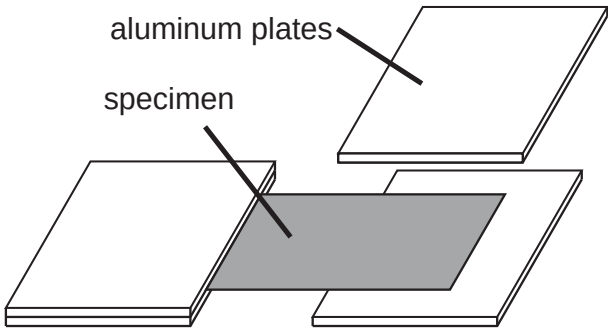

Figure 3.20: Specimen preparation for bending test

The plates are then connected with Scotch Magic Tape to the axial testing machine (INSTRON 5569 with a 10 N load cell), see Figure 3.21. The specimen does not touch the testing machine in any point of the test; instead, it rests solely on the tape. This is necessary to reduce the effect of friction and contact. The bending stiffness of the tape is much lower than that of the specimen, and it has therefore been treated as a perfect hinge, see Figure 3.22

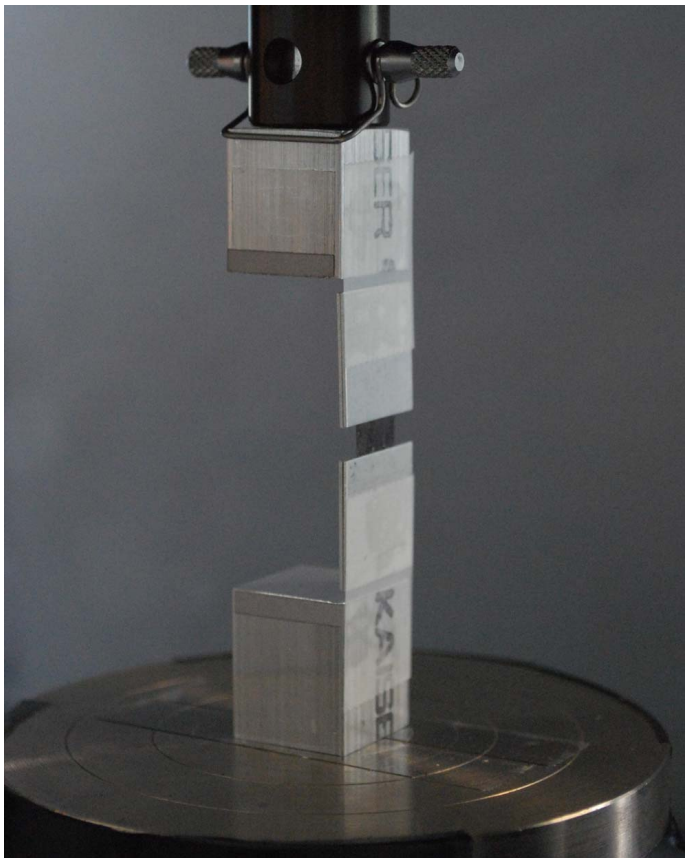

Figure 3.21: Moment-curvature experimental setup

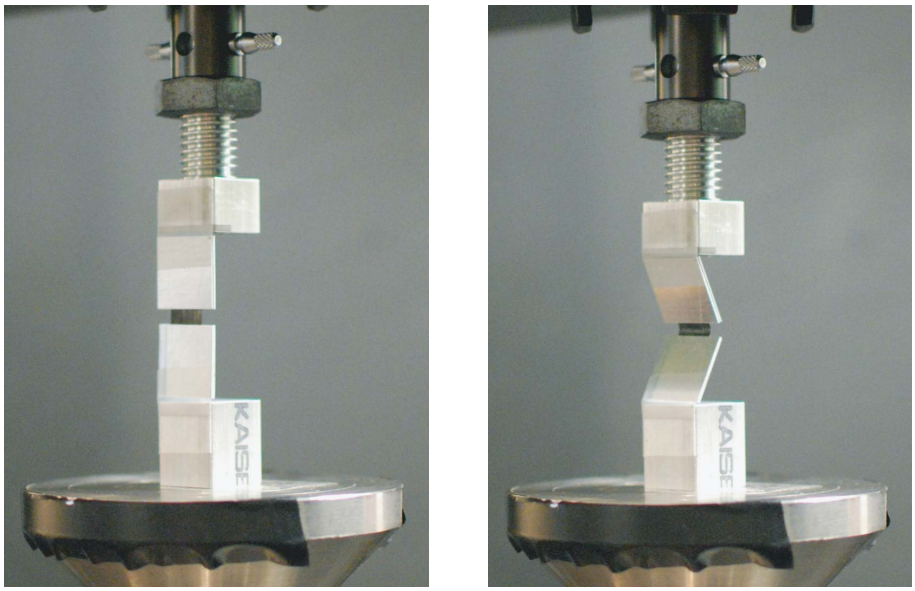

Figure 3.22: Moment-curvature experimental setup: (a) initial state and (b) post-buckled configuration

The load due to the specimen's weight, approximately equal to 0.01 N, was measured, in order to take into account its effect. A schematic analysis of the test is shown in Figure 3.23. It is performed controlling the vertical displacement, equal to $2L + b - 2h$, and measuring the vertical force F. Assuming a constant curvature in the specimen, the main geometric parameters can be expressed as:

$$\kappa = \frac{2\theta}{b} \tag{3.6}$$

$$h = L\cos\theta + \frac{b}{2\theta}\sin\theta \tag{3.7}$$

$$d = L\sin\theta + \frac{b}{2\theta}(1 - \cos\theta) \ . \tag{3.8}$$

The curvature can then be calculated with the vertical displacement, measured by the Instron.

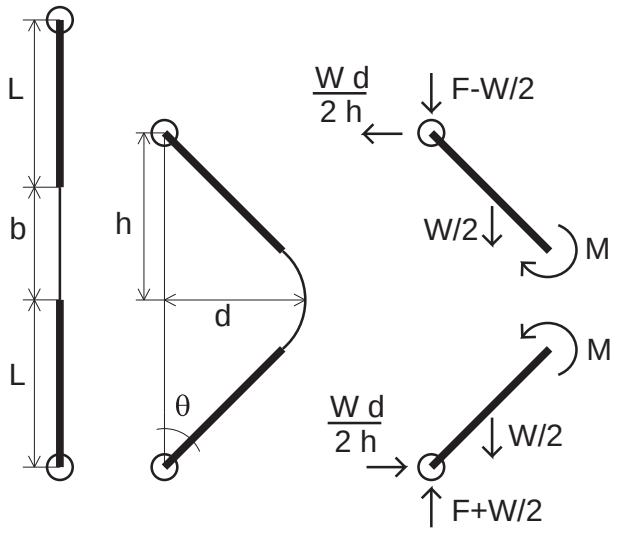

Figure 3.23: Analysis of the test setup: geometry and force equilibrium

The assumption of constant curvature implies constant moment within the compliant part of the specimen, equal to:

$$M = \left(F - \frac{W}{4}\right) d \tag{3.9}$$

where F is the applied force and W the weight of the specimen, including the aluminium-alloy plates. This result is valid when the length of the composite-only strip is small compared to the length of the end plates, $b << L$; in the present case $b = 4$ mm and $L = 25.4$ mm. The assumption was checked comparing the results to the solution of the Euler's elastica, in which the curvature was not assumed to be constant. No difference could be observed. Photos of the specimens during the tests also showed uniform curvature.

Table 3.2 summarizes the typical dimensions of the specimens used during the tests.

Length, b	4 mm
Width	9 – 15 mm
Thickness — 55% V_f	45 μm
Thickness — 30% V_f	75 μm

Table 3.2: Dimensions of bending test specimens

3.5.3 Bending test results

The test results are shown in Figure 3.24. Both specimens present a linear response for low curvatures. At approximately 0.07 mm^{-1} the stiffness starts decreasing, and for high curvatures the slope becomes negative.

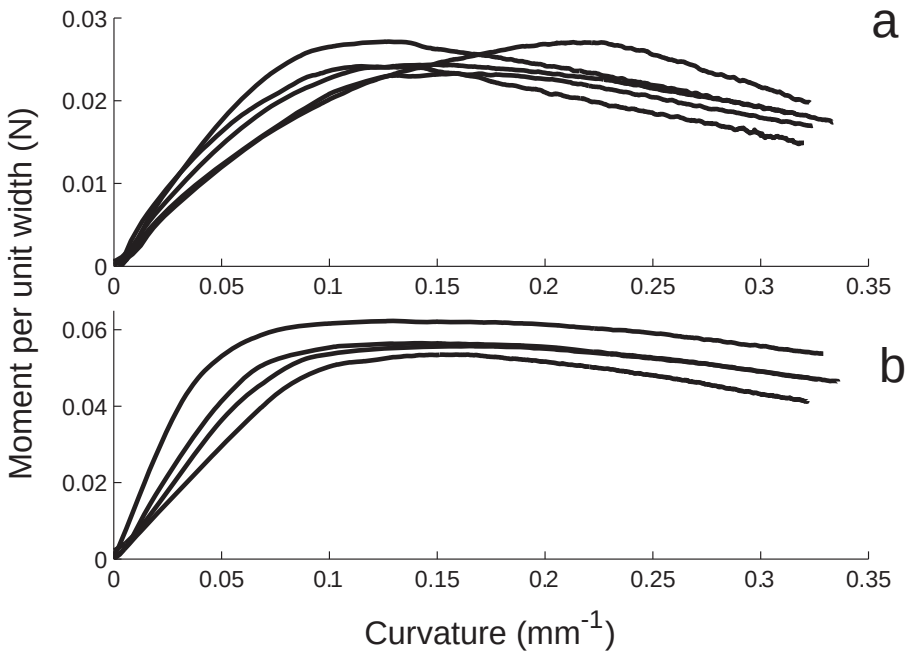

Figure 3.24: Moment-curvature relationship: for experiments with (a) 55% volume fraction and (b) 30% volume fraction

The tests were performed at three different speeds: 0.25, 0.5, and 1 mm/min of vertical displacement. Note that a linear vertical displacement does not translate into linear increase in curvature, nor in strain in the matrix and fibers, due to the complicated stress state in the matrix. No significant difference was found between them, and rate-dependance effects are therefore neglected.

If more than one loading-unloading cycle is applied, the specimens show strain-induced stress softening, also known as Mullins effect. The moment-curvature relationship obtained from a test with a single specimen can be seen in Figure 3.25. The material was folded in three sets of four cycles, each one with increasing maximum curvature: 0.22, 0.30, and 0.36 mm^{-1}. The stiffness decreased after each cycle, the difference being higher between the first and the second cycle of each set. The same specimen was tested again 24 hours after the first test. The damage was not recovered, and the stiffness was ap-

proximately the same as at the end of the previous test. Both the permanent loss of stiffness and the cycle hysteresis are less pronounced in the specimens with lower volume fraction. This agrees with the typical behavior of particle-reinforced rubbers explained in Section 2.3.

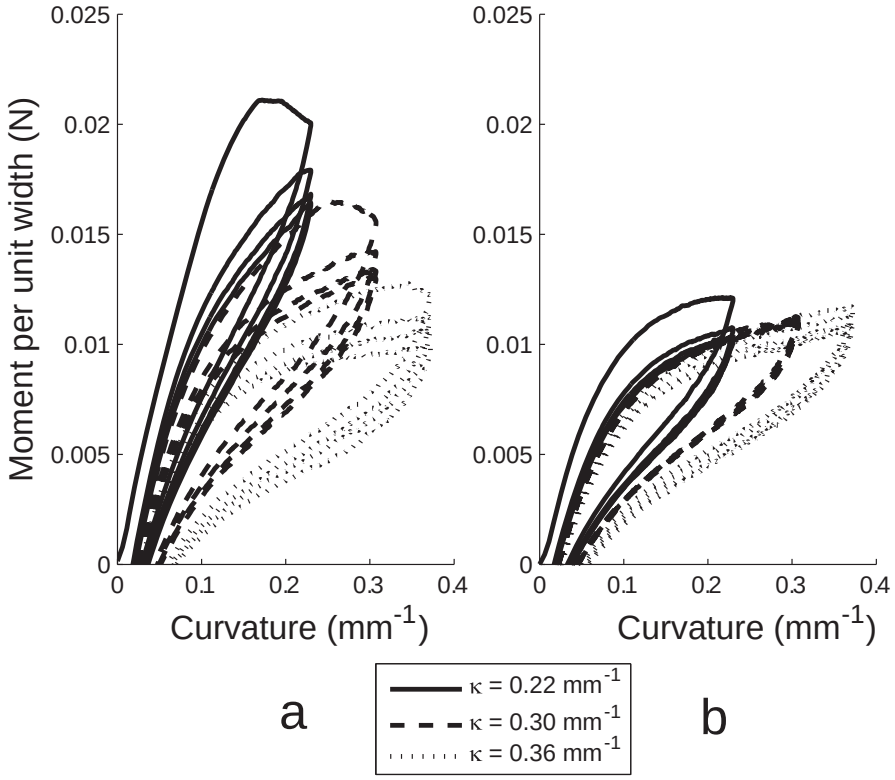

Figure 3.25: Moment-curvature relationship showing Mullins effect. Volume fraction 55%

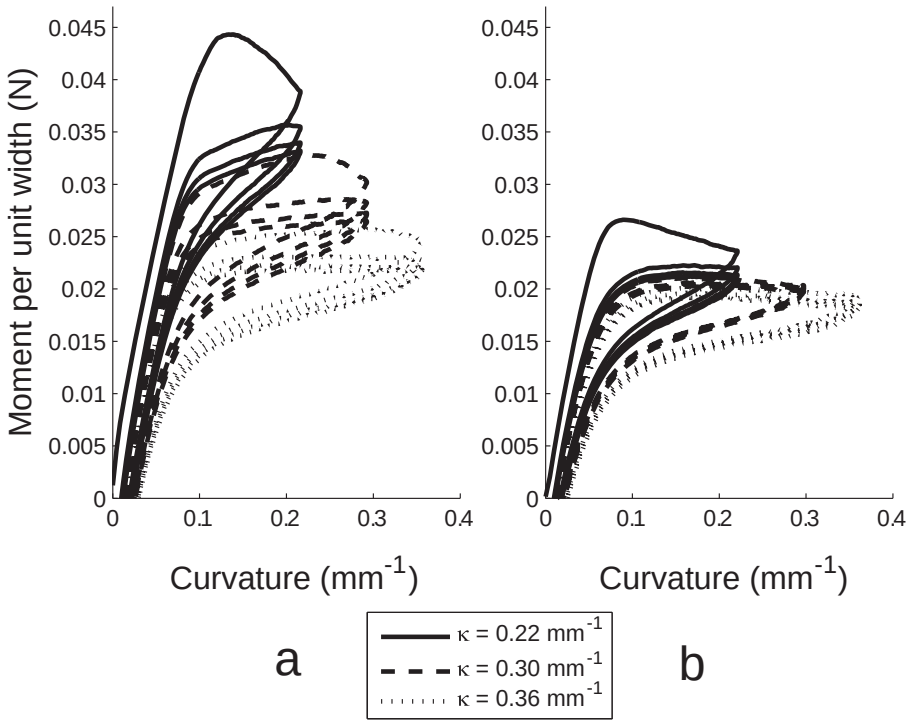

Figure 3.26: Moment-curvature relationship of a 30% specimen under cycling loading: (a) initial test and (b) test repeated on same specimen after 24 hours

3.6 Loading transverse to the fibers

The main interest of testing the material with loading perpendicular to the fiber direction is to analyze the damage process taking place. In the bending experiments the combination of geometrical and material nonlinearities make this analysis more difficult, while in this case all possible sources of nonlinearity are due to the material response.

The results of this section will be presented as average Piola-Kirchhoff stress $\bar{\sigma}_y$, obtained dividing the load F by the initial cross section A

$$\bar{\sigma}_y = \frac{F}{A} \tag{3.10}$$

and average engineering strain $\bar{\epsilon}_y$, obtained by dividing the displacement δ by the length

of the gauge section L

$$\bar{\epsilon}_y = \frac{\delta}{L} \tag{3.11}$$

Attempts to test the transverse response of the material in specimens with only one ply were unsuccessful. It is common for the composite to have some regions in which the fibers split, with only silicone remaining. Those sections break under a very low applied load. Instead, specimens with three and four plies were prepared. The specimens were tested using an INSTRON 5569 testing machine with a 10 N load cell. The strain was measured using a laser extensometer as the distance between two reflecting tapes, placed at a typical initial distance of 25 mm. The width of the specimens is 25 mm, and the total length is 90 – 100 mm, see Figure 3.27.

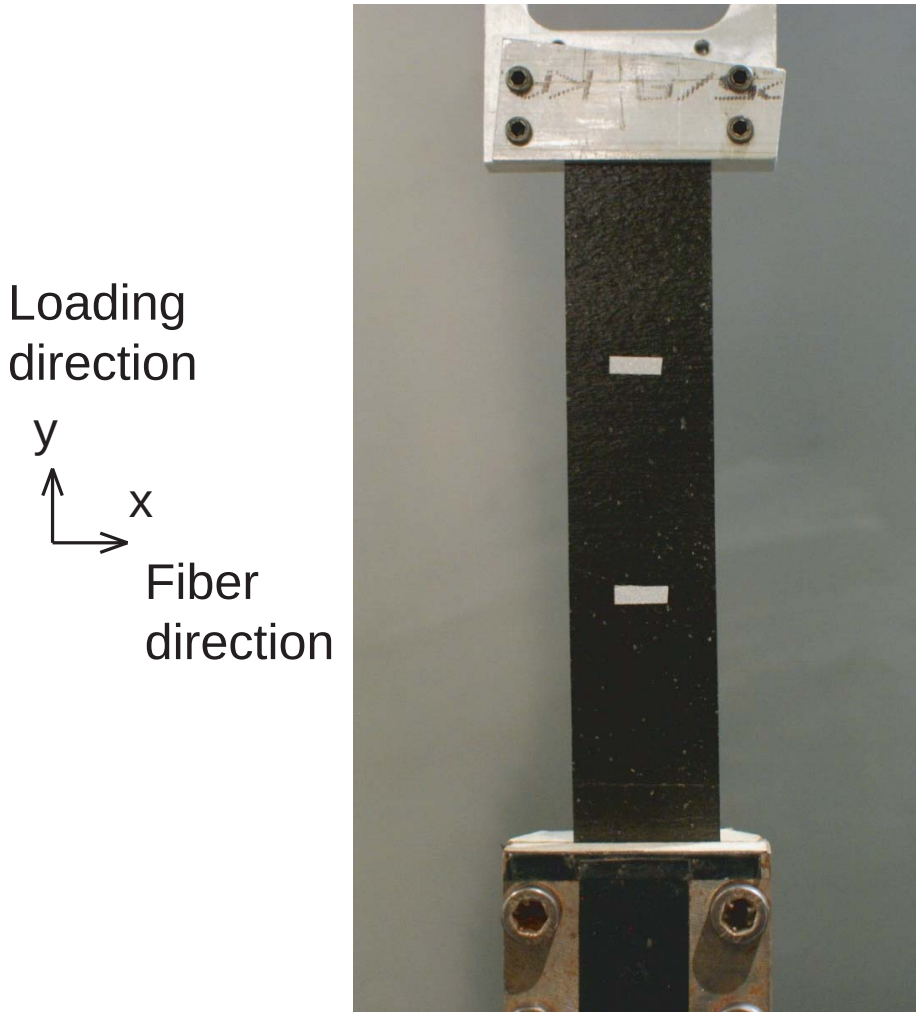

Figure 3.27: Loading transverse to the fibers experimental setup

The average stress and strain for a given specimen is shown in Figure 3.28. It was tested on three cycles, with a maximum strain of 2.5% for the three of them. The response is highly nonlinear, with a very high stress softening and hysteresis. It also shows significant permanent deformation.

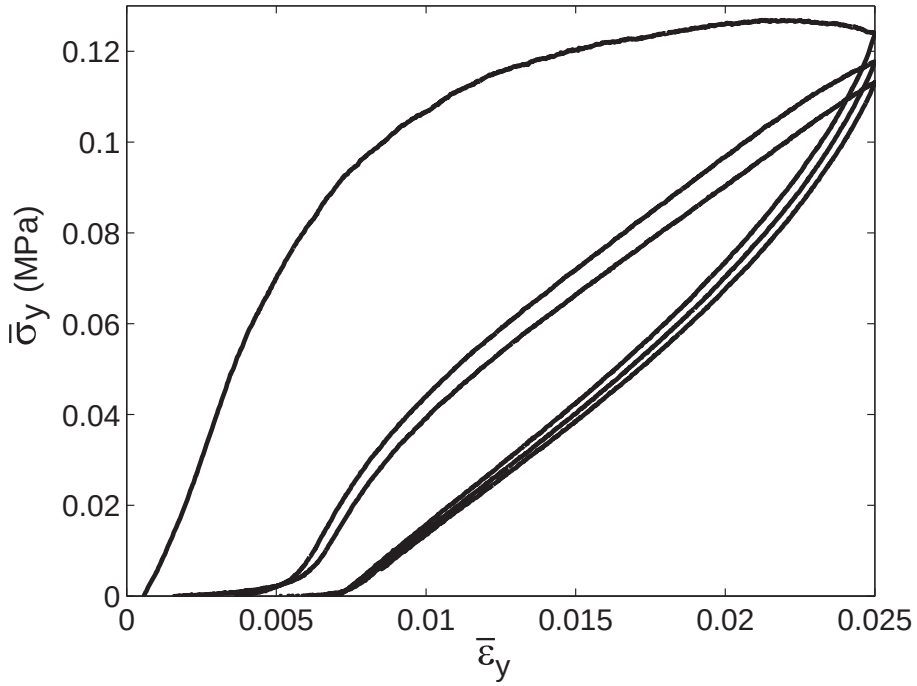

Figure 3.28: Stress vs. strain under transverse loading, three cycles with the same maximum strain. The specimen has four plies, 50% volume fraction

The behavior under this loading case is much closer to the typical Mullins effect observed in particle-reinforced rubber. Figure 3.29 shows the response of a specimen subjected to three cycles of increasing maximum strain (0.01, 0.02, and 0.03, respectively). Each cycle consists of three loops. The main drop in stiffness is observed after the first loop to a given maximum strain, although there is a slight drop in the rest of the cycle. The same specimen was tested again after 24 hours, showing no signs of recovery.

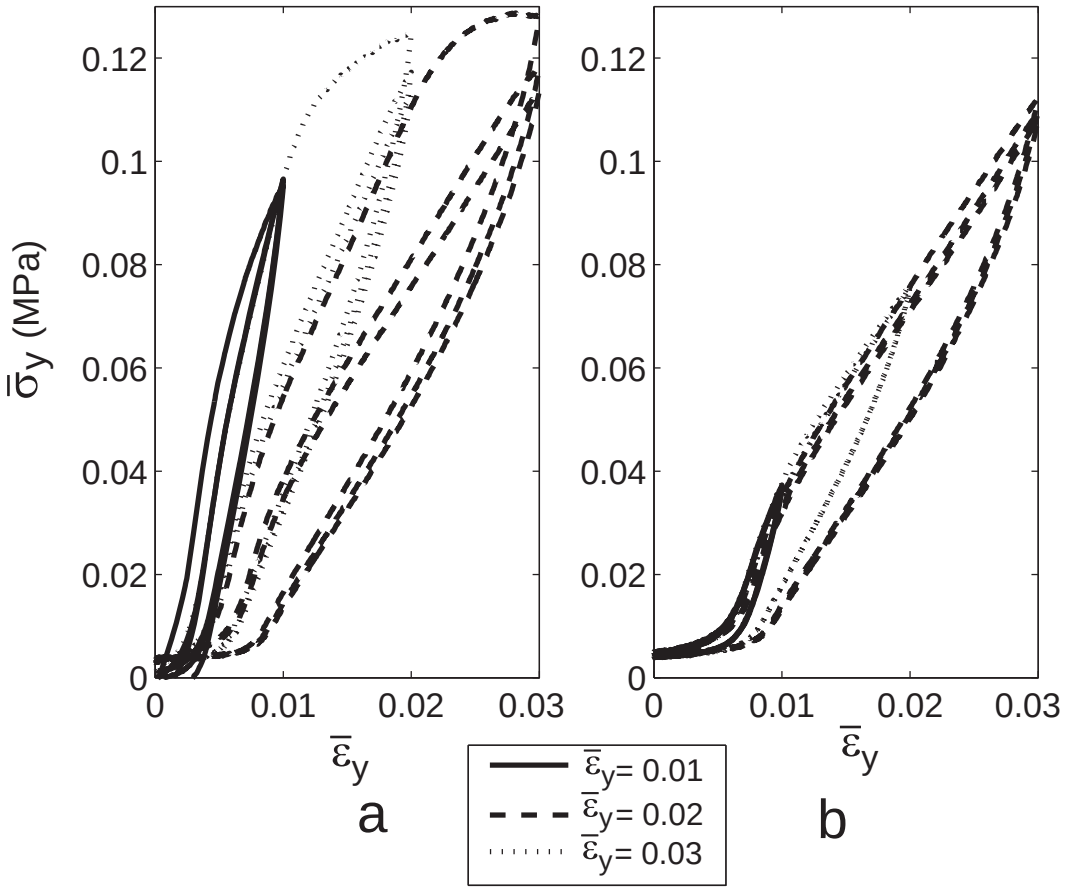

Figure 3.29: Stress vs. strain under transverse loading: (a) untested specimen and (b) same specimen after 24 hours. The specimen has four plies, 50% volume fraction

Figure 3.30 shows the response of four nominally identical specimens, subjected to three cycles of increasing maximum strain followed by further extension until failure. The maximum strains applied on the cycles correspond to 0.01, 0.02, and 0.03 for the whole specimen, controlled by the testing machine, and translates into approximately the same values for the range over which the laser extensometer takes measurements. The responses of the four specimens are similar for the first two cycles, which is the point at which failure typically starts appearing, and vary widely after that. In the second specimen (Figure 3.30 b), the material was so damaged that the third cycle could not take place. The other three specimens completed the three cycles, although with noticeable damage in the case of the fourth specimen, as seen by the much higher strains. In the case of the first and fourth specimens, the material failed after the three cycles. The different response for those two specimens is explained by the position of the main crack producing

failure, which was inside the laser gauge for the first specimen, and outside for the fourth one.

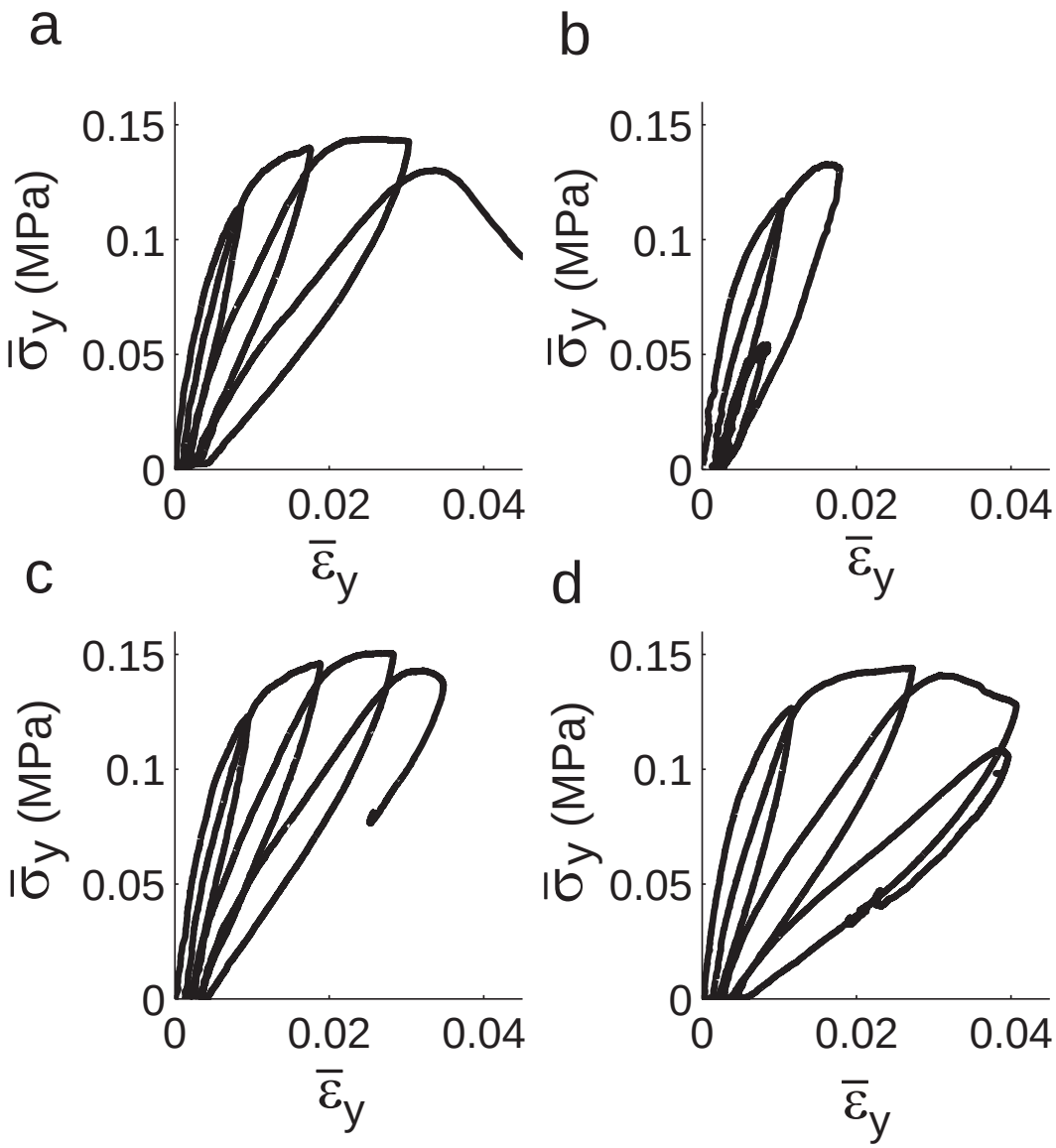

Figure 3.30: Stress vs. strain under transverse loading for four different specimens of three plies, 55% volume fraction. The specimens were tested until failure, taking place: (a) after the cycles, inside the laser gauge, (b) during the second cycle, (c) after the cycles, outside of the laser gauge, and (d) after the cycles, with noticeable damage during the third cycle

The variability of the failure behavior shows an essential difference between composites with a silicone matrix vs. those with a standard epoxy matrix. In the latter case failure

is sudden. Instead composites with a silicone matrix form stable cracks that need a load increase to grow. Hence this material often retains much of its stiffness even after visible cracks have formed; physically this behavior can be explained by a small misalignment of the fibers that results in a few fibers going across the path of the crack tears. These fibers are able to rotate, aligning with the loading direction. Since the fibers are much stiffer than the matrix, even a small number of fibers is able to sustain the same loads as the rest of the specimen.

In the case of specimens with lower volume fraction, the lower stress concentrations in the fibers reduce the nonlinearity and the stress softening. The behavior is approximately linear for a much larger range of strains, and the hysteresis is very low. These specimens also reach a much higher strain at failure, see Figure 3.31.

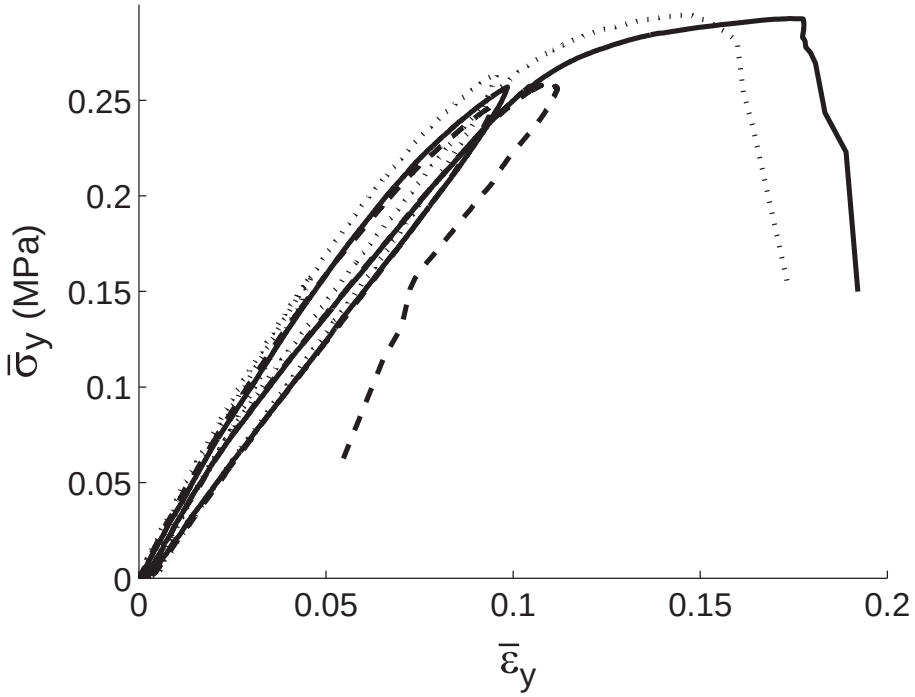

Figure 3.31: Stress vs. strain under transverse loading, three cycles with the same maximum strain. The specimens have three plies, 22% volume fraction

Chapter 4

Finite Element Model

A numerical study of the composite material used in the experiments was performed in the package Abaqus/Standard (ABAQUS/Standard, 2007). It is common to model composites using homogenization techniques, as a single material in which the fibers introduce anisotropy. In this case, the properties of the material depend on the microscopic nonlinear behavior of the fibers. In order to model this effect, it is necessary to study the micromechanics of the material, and how the fibers move while buckling. The simulations presented here model in high detail a representative volume element (RVE) of the material containing a limited number of fibers, in which both matrix and fibers are modeled with solid elements. Attempts to model the fibers with 1D beam elements did not produce coherent results. The reason is that the use of 1D elements make it impossible to correctly model the volume fraction in the material. This affects the stress distribution in the matrix. The use of solid elements is required to preserve the geometry of the problem.

This chapter discusses the finite element model used in this study. The layout is as follows: First, the model geometry and the boundary conditions will be explained in Section 4.1. Particular attention is paid to the differences for the cases of bending and tension transverse to the fibers. The fiber arrangement will be discussed next. Three different options have been used: a regular lattice, a random arrangement, and a random arrangement based on the real microstructure observed in micrographs of the material.

The next section studies the influence of the parameters used to construct the models, such as the minimum distance between fibers, or the mesh size. Finally, the material models and elements used for fibers, matrix, and their interface are detailed in Section 4.4.

More specific details regarding numerical instability, and the particular Abaqus options

used, can be found in Appendix A.

4.1 Model geometry and boundary conditions

Two different models have been used, a 3D one to study the folding behavior, and a generalized plane strain model for the loading transverse to the fibers. There are several differences between the two.

First, in order to study bending, the RVE must extend through the whole thickness of the tow, as seen in Figure 4.1. This is due to the fact that buckling will induce a different behavior in the fibers in the compression side than those in the tension side. Defining x as the direction of the fibers and y as perpendicular to the plane of the tow, we will consider the strip resulting from cutting the tow with two planes parallel to the xy plane, as seen in the figure. The piece has length L, width W, and height H, as defined in the figure.

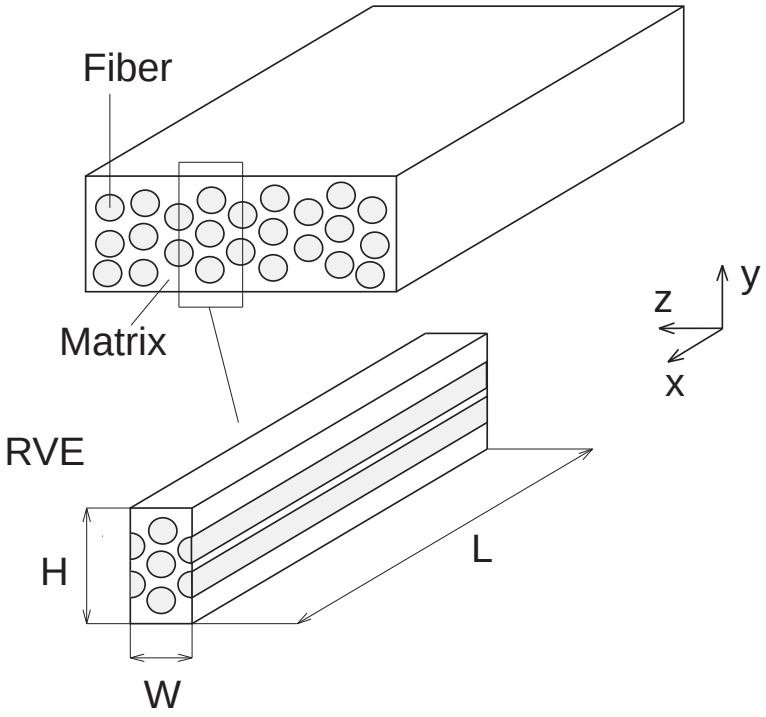

Figure 4.1: Representative volume element

The boundary conditions on the faces of this RVE must ensure that the piece of material modeled is periodic in the z direction. Since the meshing of the two faces is

identical, the conditions can be applied directly on the nodes using the EQUATION command in ABAQUS. The displacement components in the x and y directions (u and v, respectively) of every node are forced to be equal to those of the corresponding node in the opposite face.

$$u(x, y, 0) = u(x, y, W) \tag{4.1}$$

$$v(x, y, 0) = v(x, y, W) \ . \tag{4.2}$$

The difference of displacements in the z direction (w) between every pair of nodes has to be same. This implies that the width of the material might change with respect to the undeformed configuration, but it has to be constant through the model.

$$w(x_1, y_1, 0) - w(x_1, y_1, W) = w(x_2, y_2, 0) - w(x_2, y_2, W) \tag{4.3}$$

In order to achieve that, the only boundary condition applied in the end cross section is the requirement for the nodes to remain in the same plane. The relative position within the plane is unconstrained, including the displacement in the z direction. That plane is connected to a dummy node, one for each face. Equal and opposite rotations about z, of magnitude θ, are applied to each dummy node. One of the dummy nodes is constrained against translation in all directions, while the other one is free to translate along the x axis, in order to eliminate the rigid body motions. The faces perpendicular to the y axis are left free.

In the case of the 2D RVE used to study loading transverse to the fibers, it is not necessary to model the whole thickness. Instead, the model uses periodic boundary conditions in both the y and z directions:

$$v(y, 0) = v(y, L_2) \tag{4.4}$$

$$w(y_1, 0) - w(y_1, L_2) = w(y_2, 0) - w(y_2, L_2) \tag{4.5}$$

$$w(0, z) = w(L_1, z) \tag{4.6}$$

$$v(0, z_1) - v(L_1, z_1) = v(0, z_2) - v(L_1, z_2) \tag{4.7}$$

where v and w are the displacements in the y and z direction, and L_1 and L_2 are the dimensions of the 2D RVE. This boundary conditions imply that the dimensions of the RVE might change with respect to the undeformed configuration, but they have to be constant through the model. The loading is imposed as a prescribed relative displacement between two faces. No constraint on the relative position of the other two faces is applied.

4.2 Fiber arrangement

In the case of the folding simulations, the first analysis performed modeled the geometry of the fibers as a hexagonal grid of cylindrical rods. The number of fibers used matches the observations from the micrographs. The width of the RVE is such that it contains a column of complete fibers, as well as two columns of half fibers (Figure 4.6). The distance between the fibers, as well as the rest of the geometric properties of the RVE, depend only on the fiber radius and the number of fibers per unit width and the volume fraction, which can be obtained from measurements on the material (see Table 4.1).

Volume fraction	55 %	30 %
Number of fibers	9	13
Distance between fibers	8.99 μm	12.17 μm
Height (H)	40.4 μm	79.1 μm
Width (W)	15.6 μm	21.1 μm

Table 4.1: Dimension of the RVEs for the folding simulations

The hexagonal lattice is a common idealization of fiber distributions, but micrographs of the material show it is an unrealistic one. Since the fibers are expected to undergo very high deflections, the strain energy in the matrix will greatly depend on the spacing between fibers. This will be analyzed in more detail in Section 4.3.1. In order to produce more

accurate simulations, the RVEs should be based on the real fiber arrangement observed in micrographs of the material.

As explained in Section 3.3, the variable chosen to describe the microstructure is the second-order intensity function $K(r)$. Then an algorithm to reconstruct the random microstructure is required. In this work, the Random Sequential Adsortion algorithm by Rintoul and Torquato (1997) has been followed. It is an iterative process that tries to minimize a potential E that describes the difference between the goal and current configurations of the system. E does not need to have a physical meaning, and is usually defined using the parametrization function $f(r)$ as $E = \sum_k (f(r_k) - f_0(r_k))$, where $f_0(r)$ is the value of the function for the reference configuration, and the sum is made over the bins used to discretize the functions in r. The potential is therefore a measure of the distance between the current configuration and that observed in the micrographs, and the goal of the algorithm is to reduce it.

In every iteration a fiber is then picked randomly, and a random displacement is applied. The potential E' is calculated for this new configuration. The displacement is accepted according to the the probability P, defined as

$$P = \begin{cases} 1 & \text{if } \Delta E \leq 0 \\ e^{\frac{-\Delta E}{A}} & \text{if } \Delta E > 0 \end{cases} \tag{4.8}$$

where $\Delta E = E' - E$ and A is a parameter that controls how fast do the system evolves (a value of 0.05 has been used in this work). This means that the algorithm would accept some of the displacements in which the energy increases slightly, but almost none implying a large increment. The iterations are repeated until the system converges to a stable value of E. Note that the displacement applied to the fibers will respect the periodic boundary conditions of the RVE.

Two different potentials have been used in this work, and the algorithm finally implemented is detailed in the following subsections.

4.2.1 Initial mesh

First, the fibers are randomly distributed with a hard-core process. This is a Poisson random process in which a limitation on the minimum distance between the center of fibers is introduced. In the cases of high volume fraction, not all the fibers can be located randomly. The jamming limit is given by Tanemura (1979) as 0.547. This value is lowered if the distance imposed is higher than the fiber diameter, as it is the case here. In practice, jamming is observed in cases with 50% volume fraction or higher. If after 1000 attempts a fiber has not been accepted, it is located even if it overlaps with other fibers. In those cases, the Random Sequential Adsortion algorithm is used, with the potential energy

$$E = \sum_i \sum_j \left(\left(\frac{100}{d_{ij}} + 10 \right) \delta_{ij} + 100\delta_i \right) \tag{4.9}$$

where d_{ij} is the distance between two fibers, δ_{ij} is equal to one if the distance between the i-th and j-th fibers is less than the minimum imposed and zero otherwise, and δ_i is one if the i-th fiber is closer to the edges of the RVE than a specified value and zero otherwise. The factors multiplying δ_{ij} and δ_i are weights without a physical meaning. The minimization of this potential will ensure that the geometric rules are satisfied.

This process only depends on the overall volume fraction assigned to the RVE, and the geometric conditions imposed to avoid defective meshing, see Section 4.3.1.

4.2.2 Reconstruction of real microstructure

Once an initial mesh has been obtained, the next step is to make it evolve to a configuration that is statistically equivalent to the real microstructure observed in the micrographs, defined as having the same $K(r)$. It is now that the second-order intensity function $K(r)$ is used, in a potential of the form:

$$E = \sum_k \left(K\left(r_k\right) - \tilde{K}\left(r_k\right) \right)^2 + \sum_i \sum_j \left(\left(\frac{100}{d_{ij}} + 10 \right) \delta_{ij} + 100\delta_i \right) . \tag{4.10}$$

The high values assigned to the weights in the terms enforcing the minimum distance between the fibers (see Section 4.3.1) make sure that fulfilling the geometry requirements

is dominant over a reduction of the term depending on K.

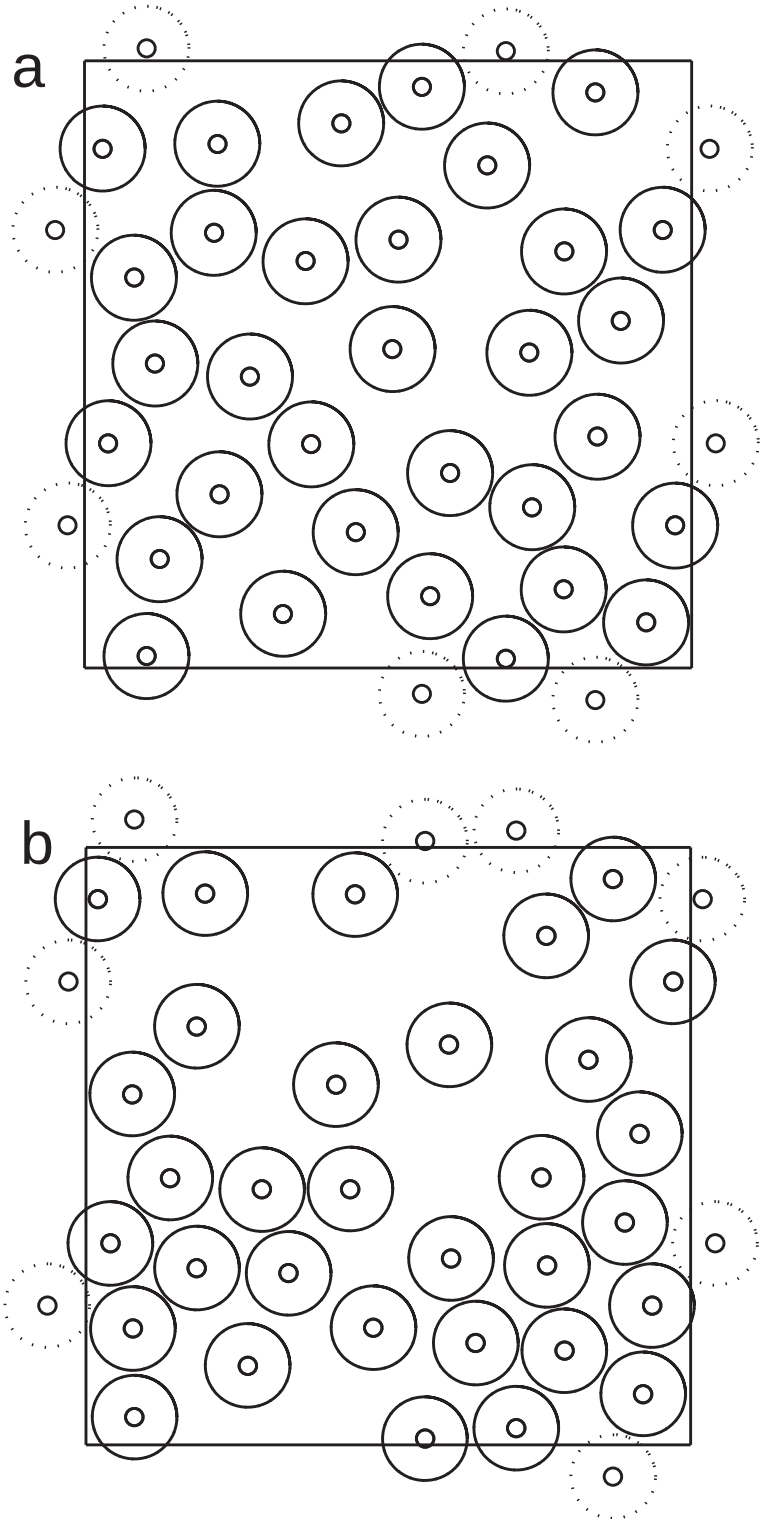

Figure 4.2: Fiber distribution in a 50-μm-square RVE with 50% volume fraction: (a) original random arrangement and (b) subsequent reconstruction of the microstructure observed in micrographs

This process leads to two different types of random RVEs: obtained purely through the hard-core process, and reconstructed from the micrographs. Only the reconstructed arrangements, along with the hexagonal lattices, will be used in the folding simulations. However, both types will be used when studying the response to transverse loading. The distinction between "purely random" and "reconstructed" will be made explicitly in each case.

4.3 Model convergence

This section presents a study of the influence of the parameters used to create the model, such as the size of the RVE, or the level of mesh refinement. In the case of the bending simulations, it was not possible to perform a detailed parametric study due to the intrinsic computational cost of the model. Even with a RVE containing very few fibers, and a coarse mesh, the complete models have in the order of 100,000 to 150,000 nodes. The two-dimensional models are, however, much less computationally expensive, and a more detailed convergence analysis could be carried out. Note that this is based on the linear stiffness, defined as $\frac{d\bar{\sigma}_y}{\bar{\epsilon}_y}$ at $\bar{\epsilon}_y = 0$.

4.3.1 Minimum distance between fibers

The minimum distance between the fibers is obviously a very important parameter in the process described above. It affects the jamming limit at high volume fractions, but it also has a great influence on the second-order intensity function of the initial configuration. Figure 4.3 shows the linear stiffness obtained from random models in which the distance varies from 0.1 μm to 1 μm. Five different cases were considered for each distance. The minimum stiffness is approximately the same for all distances, while the maximum stiffness increases as the distance decreases. A minimum separation of 0.25 μm was chosen during the rest of the simulations, in order to facilitate meshing. It represents a 3.5% of the fiber distance. The same distance was introduced as a prescribed distance to the periodic ends of the unit cell. This condition does not have a physical interpretation; it has been included only to avoid particularly hard-to-mesh regions.

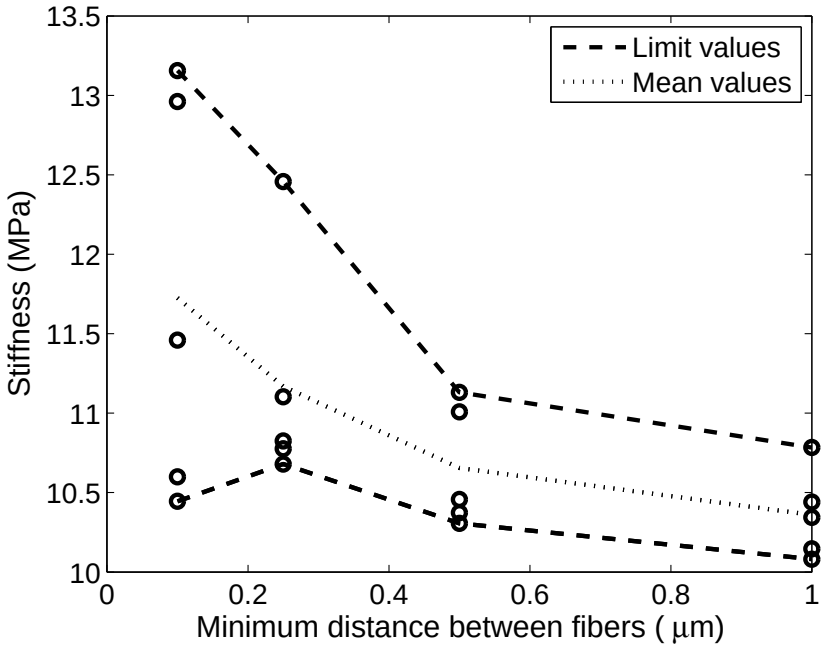

Figure 4.3: Linear stiffness under transverse loading for different minimum distance between the fibers. Purely random RVEs, 50% volume fraction, and the sides are 50 μm long

Unless stated otherwise, a value of 0.25 μm was used to produce the results presented in this study for the 2D analysis, and 1 μm for the 3D models.

4.3.2 Mesh size

The mesh size is another essential parameter in the model. Due to the incompressible nature of the matrix, very coarse meshes introduce very high stress concentrations, including check-board pattern due to the effect of the hydrostatic pressure.

In the case of the bending simulations, the results obtained with the standard mesh were compared to those obtained with a much finer mesh, showing very good agreement, both in macroscopic (wavelength, moment-curvature relationship) and microscopic (strain localization) features (see Figure 4.4).

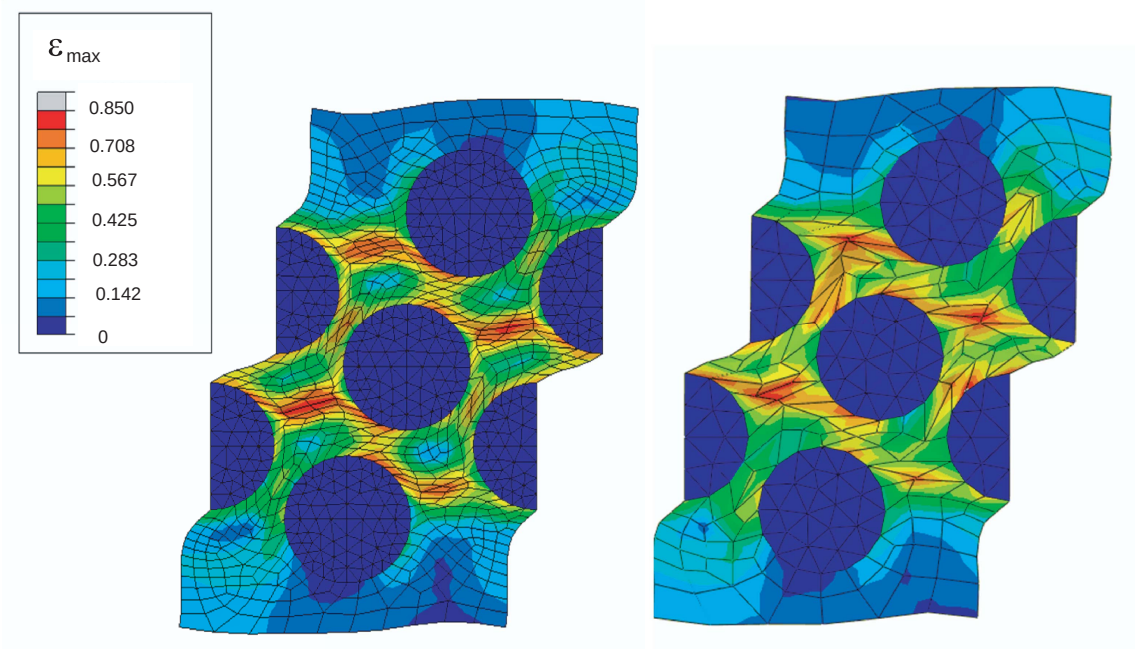

Figure 4.4: Maximum principal strain for two different meshes of the same model, showing convergence of the microscopic fields

In the the case of 2D simulations, a more detailed analysis was carried out. The usual procedure to study mesh size convergence is to analyze the evolution of the stress at a given point with respect to the mesh size. In this case, it is very hard to choose a suitable point, since the most unfavorable point will change as the mesh is refined. It is better to study the stress concentrations at all points, defined as a local stress divided by the average stress. A mesh is considered acceptable if the maximum stress concentration is the same for a finer mesh. In practice, extreme stress concentrations are avoided if there are at least two elements between each fiber. It is also possible to study the evolution of the overall response of the model, as characterized, for example, by the initial stiffness. However, meshes with a stress concentrations of up to two orders of magnitude only show a 10% increase in the global stiffness (see Figure 4.5). The results presented in this thesis use meshes in the 50,000–70,000 nodes range, unless stated otherwise.

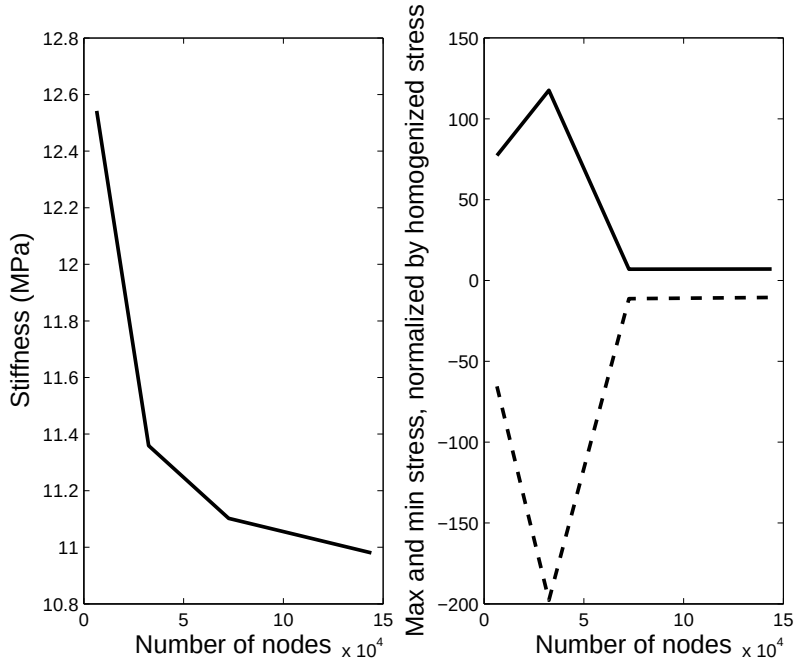

Figure 4.5: Effect of mesh size on transverse loading simulations: (a) linear stiffness and (b) stress concentrations. The RVEs have the same fiber distribution, purely random, with 50% volume fraction

4.3.3 Influence of RVE size

Müller (1987) showed that the use of a RVE does not ensure finding the solution in problems of nonlinear elasticity, such as buckling. Instead, all possible combinations of RVEs must be considered and analyzed. The solution would be the one providing the lowest energy in the system. This implies that the use of a RVE will neglect all possible instabilities larger than the size of the cell. This is particularly important in the case of the folding simulations, whose behavior strongly depends on the fiber buckling. In the two-dimensional simulations, in which instabilities are not so important, the main concern is to make sure that the RVE contains enough fibers to provide a good approximation of the material behavior.

4.3.3.1 Unit cell size of 3D model

The main concern in the folding simulations is to make sure that the length of the RVE is enough to capture the instabilities in the material. This would be a problem if the wave

length observed in the simulations was equal the length of the model, that is, the case in which the model presents only one instability. In that case, it would be possible that using a larger model would result in a longer wave length. However, the results presented in Chapter 5 show that the models used here are able to capture at least half a sinusoidal buckle. Since the minimum instability is a quarter of a buckle, this means that the length of the model is not affecting the response. Values of 1 mm were used for most of the simulations, and convergence with models using 1.5 mm was observed.

The height of the RVEs is given by observations on the real material, and the width was chosen in the initial simulations with hexagonal fiber arrangement so that it contains a column of complete fibers, as well as two columns of half fibers (see Figure 4.6), for convenience to apply the periodic boundary conditions. The dimensions of the RVEs are shown in Table 4.2.

Volume fraction	55 %	30 %
Number of fibers	9	13
Distance between fibers	8.99 μm	12.17 μm
Height (H)	40.4 μm	79.1 μm
Width (W)	15.6 μm	21.1 μm

Table 4.2: Dimension of the RVEs with hexagonal arrangement

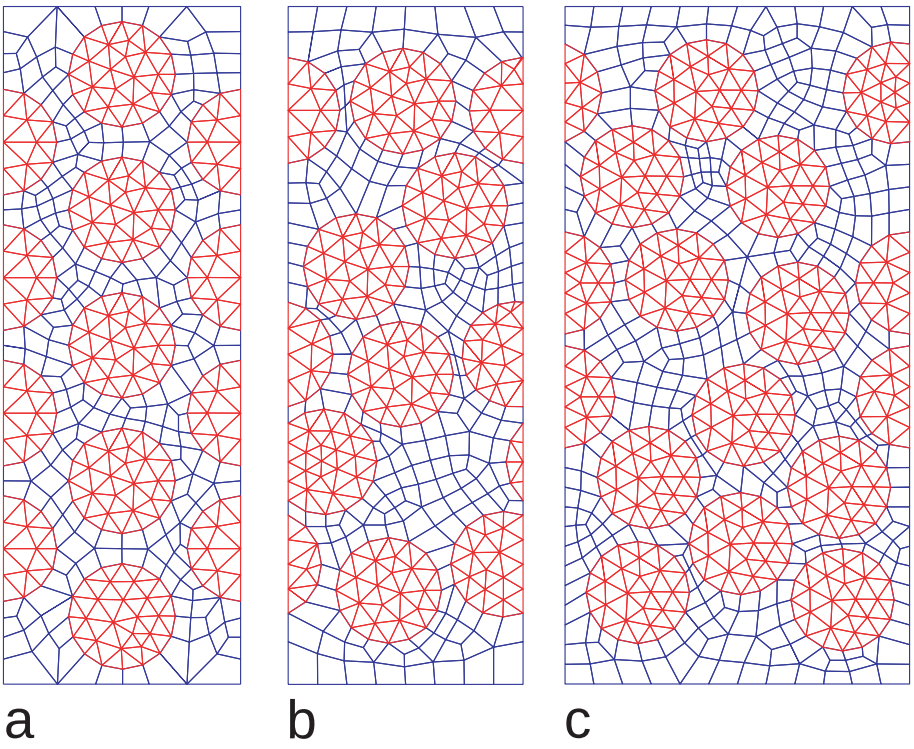

Figure 4.6: Examples of sections of three-dimensional RVEs with $V_f = 55\%$: (a) hexagonal pattern; (b) random RVE with same width as (a); and (c) random RVE with 1.5 times width of (a)

In most of the simulations using a fiber arrangement based on micrographs, the same width was used, although the dependance was studied using RVEs 1.5 times wider. In the case of 55% volume fraction, no dependance on the size of the RVE was observed. In contrast, the width of the specimens was important in the case of the low volume fraction. The reconstruction process tends to group the fibers in clusters, leaving big sections of pure silicone. The reconstruction process might produce an RVE such as the one in Figure 4.7b. The periodic boundary conditions imply that for that particular RVE there will be a section with no fibers extending through the whole material. It is possible to produce RVEs with the same size that do not present such a problem (Figure 4.7c), although the process has a better outcome with wider RVEs (Figure 4.7d).

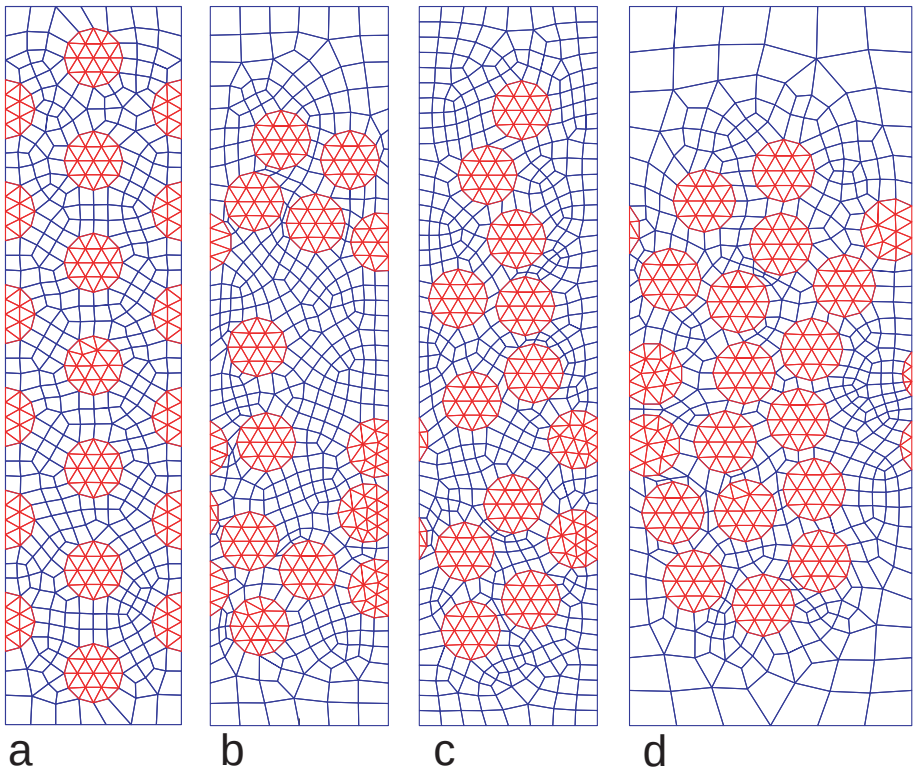

Figure 4.7: Examples of sections of three-dimensional RVEs with $V_f = 30\%$: (a) hexagonal pattern, (b) unrealistic random RVE with same width as (a); (c) realistic random RVE with same width as (a); and (d) realistic random RVE with 1.5 times width of (a)

Possible instabilities dependant on the z coordinate are neglected due to the small width of the model, but those have not been observed experimentally, and therefore it is unlikely that the model is neglecting an important deformation mechanism.

4.3.3.2 Unit cell size of 2D model

Finally, the size of the RVE is another parameter that was investigated, since the RVE needs to include enough particles to capture the behavior of the material (Monetto and Drugan, 2004). Figure 4.8 shows the linear stiffness for four different values of $L_1 = L_2$. For each size five different fiber arrangements were produced. The smallest RVE shows a wider range of values, while the other cases show very similar behavior. The transverse stiffness in both x and y directions can also be compared, to assess wether the RVE generated is orthotropic; the differences are usually on the order of 0.2%, even for $L_1 = L_2 = 25$ μm. Unless stated otherwise, a value of $L_1 = L_2 = 50$ μm is used during the rest

of this study.

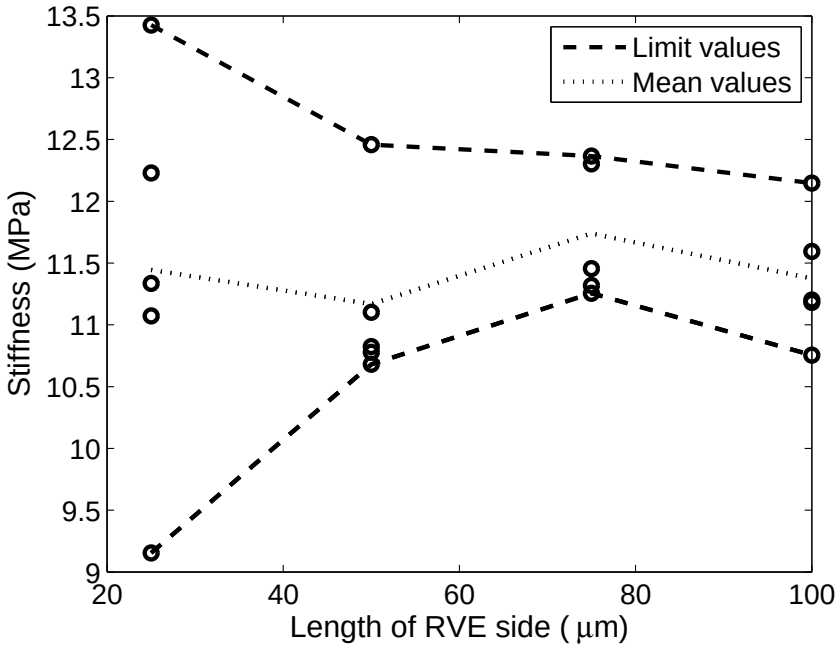

Figure 4.8: Linear stiffness for different length of the side of a square RVE. Purely random distribution, 50% volume fraction

Unless stated otherwise, a value of 50 μm is used during the rest of this study, except on the cases with very low volume fraction (under 30%), in which a value of 75 μm was used, to increase the number of fibers in the model.

4.4 Material modeling

4.4.1 Fibers

The fibers have been modeled as a linear elastic material, since the strain observed during the simulations is lower than 1%. The material is defined as isotropic. Toho Tenax does not provide a full orthotropic description of the fibers. A folding simulation was repeated modeling the fibers as orthotropic, using 20 GPa for the transverse stiffness. This value is typical of carbon fibers where no specific data could be found. The only difference observed with respect to the simulation with isotropic fibers was a small reduction in bending stiffness. The response of two-dimensional simulations was found to be same for

a using the longitudinal or the transverse stiffness of the fibers.

In the 3D elements, the elements used are triangular prisms C3D6. In the case of plane analysis, the elements are CPE3 for plane strain and CPEG3 for generalized plane strain.

4.4.2 Matrix

The matrix is modeled as a hyperelastic solid using the potential provided by Gent (2005). It was implemented in ABAQUS as a user-defined material, using the user subroutine `UHYPER`. The potential is given by:

$$W = -C_1 J_m \ln\left(1 - \frac{J_1}{J_m}\right) + C_2 \ln\left(\frac{J_2 + 3}{3}\right) \tag{4.11}$$

where

$$J_1 = \lambda_1^2 + \lambda_2^2 + \lambda_3^2 - 3 \tag{4.12}$$

$$J_2 = \lambda_1^{-2} + \lambda_2^{-2} + \lambda_3^{-2} - 3 \tag{4.13}$$

and C_1, C_2, and J_m are parameters to be determined. The parameters were obtained by fitting data to the uniaxial tests described in Section 3.1. The values obtained are $C_1 = 0.1015$ mJ, $C_2 = 0.1479$ mJ, and $J_m = 13.7870$ for the specimens cured in the autoclave and $C_1 = 0.1303$ mJ, $C_2 = 0.1345$ mJ, and $J_m = 6.3109$ for those made in the oven (see Figure 3.4). It must be noted that the strain energy tends to infinity when $J_1 = J_m$. In a uniaxial tension state, and for the values used in this work, this happens for a value of the elongation well beyond the failure stretch. However, failure in the silicone is not implemented in the model, and even if those values are not reached, the program might need to use them while calculating equilibrium. In order to prevent numerical errors, the first term in the strain energy equation is substituted by its quadratic Taylor

expansion on J_1. The complete expression is then continuous up to the second derivative:

$$W = -C_1 J_m \ln\left(1 - \frac{J_1}{J_m}\right) + C_2 \ln\left(\frac{J_2 + 3}{3}\right) \qquad \text{if} \quad J_1 \leq 0.9 J_m \tag{4.14}$$

$$\begin{aligned} W &= -C_1 J_m \ln(0.1) + \frac{C_1 \left(J_1 - 0.9 J_m\right)}{0.1} \\ &+ 0.5 \frac{J_1 \left(J_1 - 0.9 J_m\right)^2}{0.01 J_m} + C_2 \ln\left(\frac{J_2 + 3}{3}\right) \qquad \text{if} \quad J_1 > 0.9 J_m \, . \end{aligned} \tag{4.15}$$

The material was modeled as incompressible, so hybrid elements are required. Square bricks (C3D8H) and square elements (CPE4H and CPEG4H) were used. Attempts to use triangular prisms or triangular plane elements resulted in lack of convergence due locking for the first-order elements (C3D6H and CPE3H) and checker-board patterns stress distributions for the second-order elements (C3D15H and CPE6H), even for very fine meshes. High-order square elements provide coherent results for a fine enough mesh, but the linear version of the elements show better results for the same number of nodes.

4.4.3 Fiber-matrix interface

In an initial set of simulations, the interface between fibers and matrix was considered as perfect, which in practice is enforced by making the elements in both sides of the interface share the common nodes. As it will be shown in Section 5.1.2, this sometimes creates unrealistically high strain and stress values in regions of the matrix between two close fibers. In addition, the stress softening seen in the experiment hints at debonding between fibers and matrix.

In order to capture this effect, cohesive elements are introduced between the fiber and the matrix elements. The cohesive elements used are COH2D4. The behavior of the elements is described in Figure 4.9. The element keeps its initial stiffness until a traction t_0 is reached, corresponding to a separation δ_0. The material then reduces its stiffness until it reaches a value of zero for a deformation δ_f. The profile of the damaged material can follow a straight line, as in the figure, or an exponential. In the case of unloading, the profile follows a straight line to the origin. The options used in this study, as well as the

specific values, are discussed in Section 5.3. The element always retain its initial stiffness in compression.

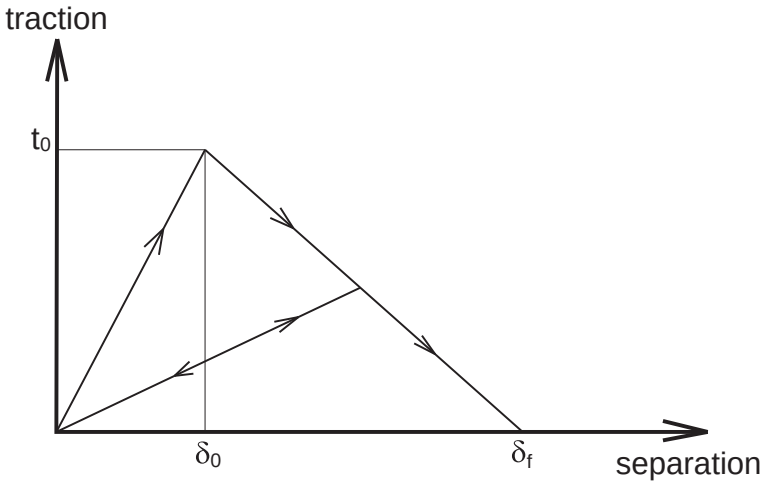

Figure 4.9: Typical traction-separation response in a cohesive element

This approach has been followed used in previous works (Zhong and Knauss, 1997 2000; Moraleda et al., 2009b) to model strain softening in particle- and fiber-reinforced solids, showing good qualitative agreement with the typical behavior observed in experiments.

Chapter 5

Finite Element Results

This chapter presents the results of the finite element simulations performed to study the behavior of the composite under bending and loading transverse to the fiber direction. The models used allow the study of not only the microscopic response of the material, but also a detailed analysis of the micromechanics of the matrix and the fibers.

Section 5.1 contains the results of the folding simulations. Two different materials have been modeled. Both of them have one ply, with 30% and 55% fiber volume fraction, respectively. In both cases, two different sets of RVEs are used, the difference being the fiber arrangement: a hexagonal grid or a random fiber arrangement based on micrographs. One of the main conclusions on this section is that the strains in the matrix are too high, meaning that neglecting any failure process in the material is unrealistic.

In order to do so, the case of transverse loading to the fibers is analyzed, since it allows a clearer study of the damage mechanism. Section 5.2 and Section 5.3 show the results of the two-dimensional models used to study the response under loading transverse to the fiber direction. In this case, the fiber arrangements used are all based on micrographs. Three different sets of specimens are used, with 22%, 50%, and 65% volume fraction. The results in Section 5.2 focus on the initial linear response, and Section 5.3 offers the results of simulations in which cohesive elements were introduced to capture the subsequent nonlinear behavior.

Finally, Section 5.4 presents a study of the differences in transverse stiffness between traditional composites and those made with an epoxy matrix. In this case, purely random fiber arrangements are used to construct the RVEs.

Unless stated otherwise, the stresses in the fibers and matrix obtained in the simula-

tions are Cauchy stresses, and the strains are logarithmic strains. The stress and strains calculated with the global response will be referred to as average strains and stresses, as was done with the ones obtained experimentally in Chapter 3.

5.1 Folding

5.1.1 Geometry

Figures 5.1 and 5.2 show different views of one of the simulations (hexagonal pattern, 55% volume fraction), in which the overall geometric characteristics are present: buckling of the fibers within the plane, large fiber deflections, higher buckle amplitude in the compression side, very uniform curvature. These features are common to all the cases, regardless of fiber arrangement and volume fraction.

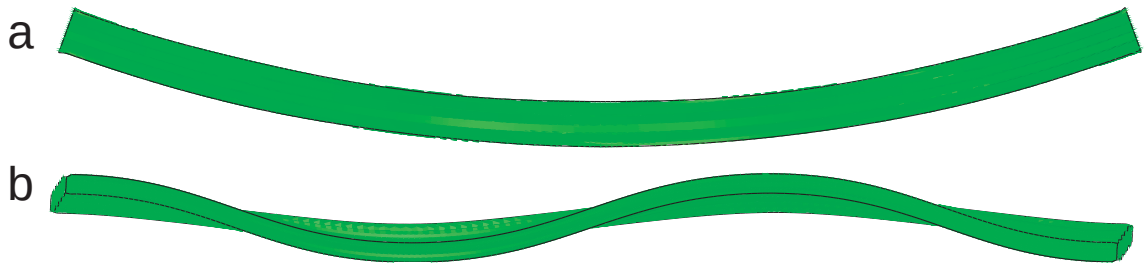

Figure 5.1: Views of deformed configurations of model with hexagonal fiber arrangement, $V_f = 55\%$ and $L = 1$ mm subject to a 0.7 mm^{-1} curvature: (a) side view and (b) top view

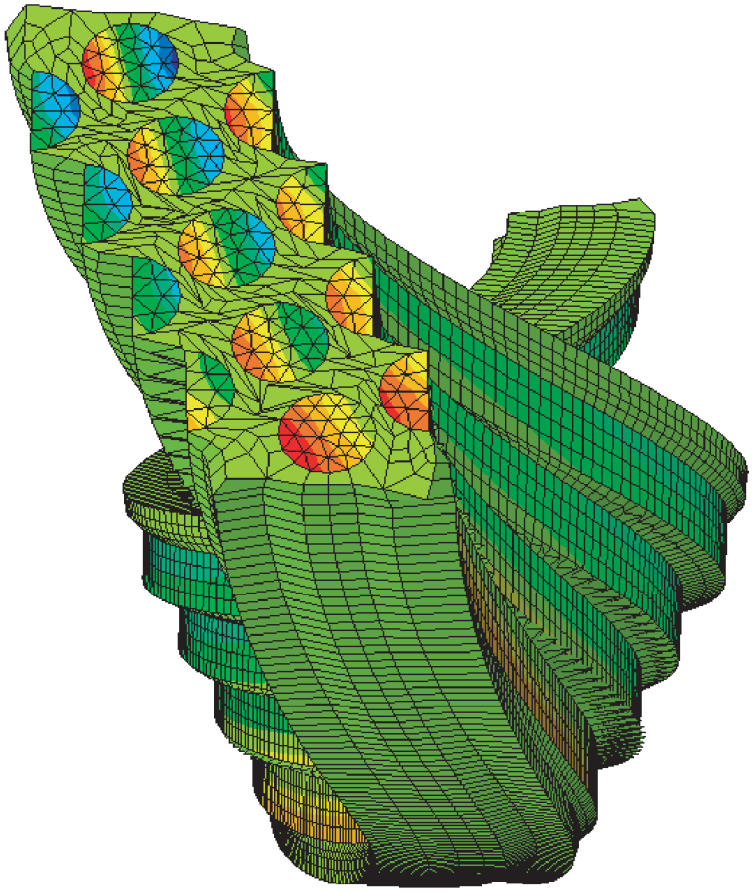

Figure 5.2: Front view of model showing longitudinal stress field. Volume fraction 55%, hexagonal fiber arrangement, 1 mm length, 0.7 mm^{-1} curvature

It must be noted that the wavelength (defined as covering π radians of phase) is limited by the length of the RVE, which is 1 mm in all the cases considered. A slightly longer or shorter RVE would probably have the same number of waves, and therefore a different wave length. This effect would be minimized using a model several times longer. However, this could not be done due to the already high computational costs.

The range of wavelengths predicted by the simulations contain those observed in the experiments for $V_f = 30\%$, but is too short for $V_f = 55\%$ (see Table 5.1). Analytical results in Francis (2008) (detailed in Section 2.2) and Lopez Jimenez and Pellegrino (2009) (detailed in Chapter 6) show that as the wavelength increases, the strain energy of the matrix does the same, while the strain energy of the fibers decreases. The results are therefore an indication that the matrix of the model is stiffer than that of the real material.

Volume fraction	55 %	30 %
Simulations	0.33–0.5 mm	0.5–1 mm
Experiments	0.55–0.70 mm	0.6–0.65 mm

Table 5.1: Comparison of wavelength in simulations and experiments

5.1.2 Strain

The evolution of the largest principal strains in the fibers with the applied curvature can be studied with these models, see Figures 5.3 and 5.5. The maximum strains are higher for random fiber arrangements.

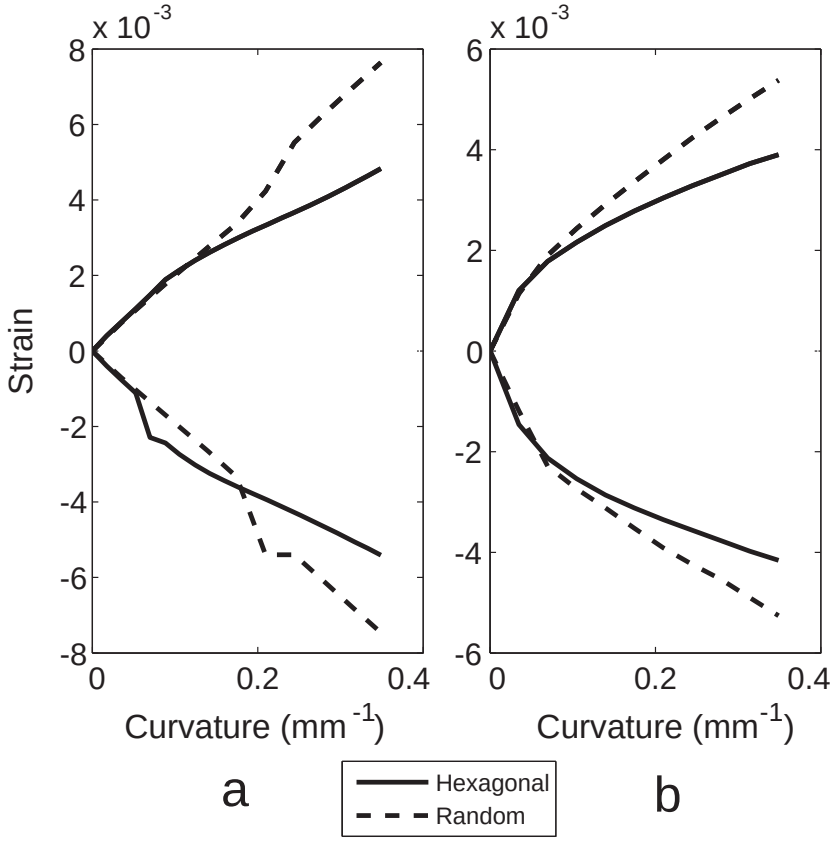

Figure 5.3: Maximum and minimum principal strains in fibers, for a model with $V_f = 30\%$

Since the fibers are mainly subjected to bending in the post-buckled state, in this case the maximum and minimum principal strains give a very good indication of the possibility of failure in the material. The failure elongation of the fibers provided by the manufacturer is 1.8 %. One of the analyses with $V_f = 30\%$ and random fiber arrangement was continued until 1.8% was reached (see Figure 5.4). However, Section 3.1.1 showed

how the fibers are able to undergo higher strain under bending. It is useful then to decompose the axial strain in the fibers in an average axial component, plus a variation due to bending. Doing so, the strain in the fiber with highest compressive strain can be decomposed in -0.58% due to axial strain and ±1.13% due to bending. Since fibers are expected to fail in tension, and the main strain component is due to the fiber curvature, the simulations show how compressed fibers are not expected to break. For the fiber with highest tensile strain, it is 1.1% axial strain and ±0.7% due to bending. In this case the axial component is still lower than the failure strain, 1.8%, although the bending component should not be completely neglected. In order to be able to accurately predict failure, it would be necessary to develop a failure criteria that combines axial and bending strain.

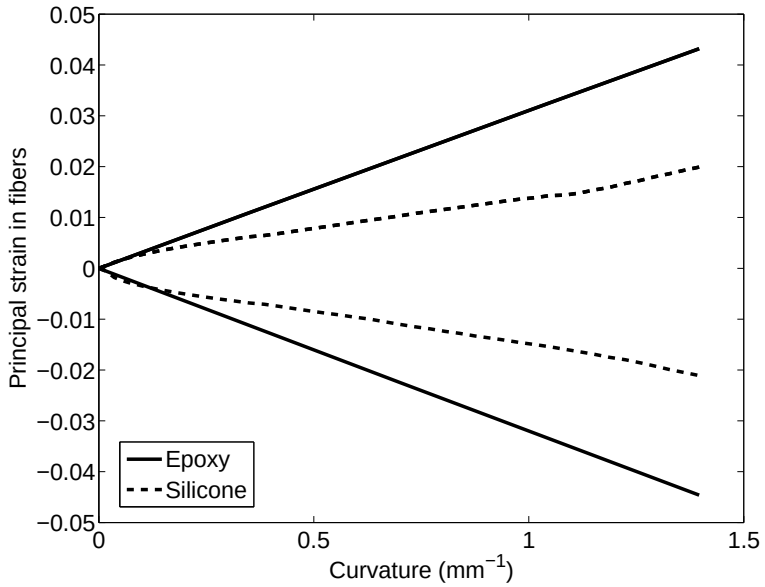

Figure 5.4: Maximum and minimum principal strains in fibers: (a) $V_f = 55\%$ and (b) $V_f = 30\%$

The strain state in the matrix is much more complex, and no failure criteria for silicone under multi-axial loading has been established. For these two reasons, the comparison of principal strains in experiments and simulations can only be used as an indication. It is clear, however, that they are too high, since the numerical values (see Figure 5.5) are much higher than the failure strains observed in the experiments, which are 120% to 140% at most. The matrix would be expected to present some form of failure (fracture,

debonding from the fiber, cavitation) before reaching such high strains.

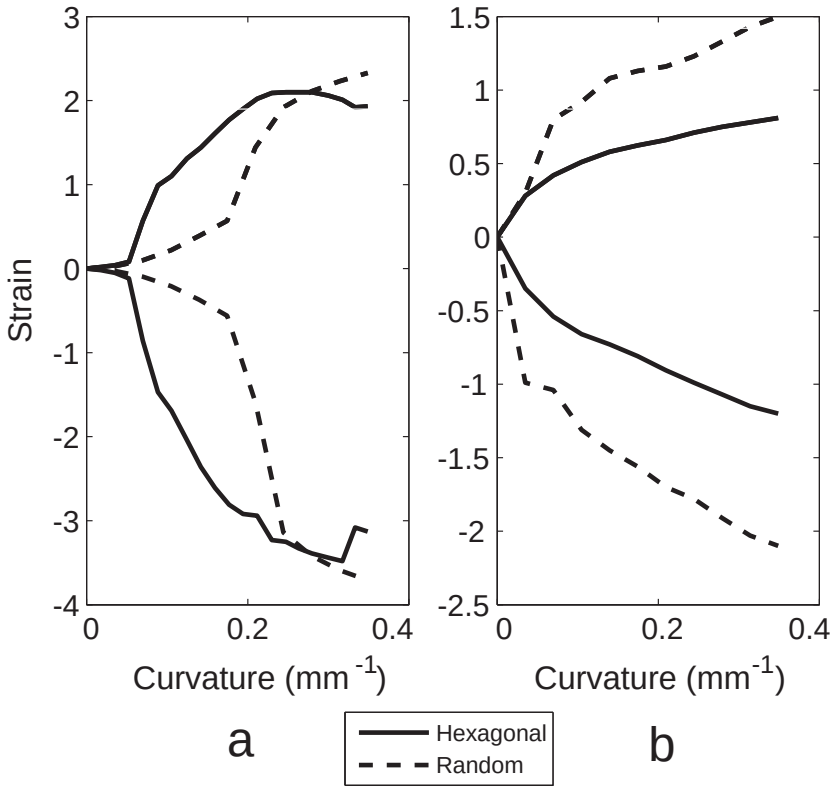

Figure 5.5: Maximum and minimum principal strains in the matrix: (a) $V_f = 55\%$ and (b) $V_f = 30\%$

The fact that the maximum principal strains are similar in the matrix for both hexagonal and random arrangements does not mean that the strain states are similar in both configurations. Figure 5.6 shows the values of γ_{yz} for two cross sections in models with $V_f = 55\%$. Both sections are taken at the point of maximum deflection of the buckle, with curvature 0.35 mm^{-1}. In the case of hexagonal pattern all fibers buckle in the same way, the only difference being the amplitude, which is higher for the fibers in the compression, leading to the shearing in the $y - z$ plane. This shear strain is particular of buckling under bending, since in pure compression the amplitude will be the same for all the fibers. The strain pattern in the matrix is very regular. The randomly arranged fibers create a more complex strain state, with very high positive and negative strains within the same section. In this case the amplitude of the buckle is practically the same through the whole thickness. This produces higher strains in both matrix and fibers.

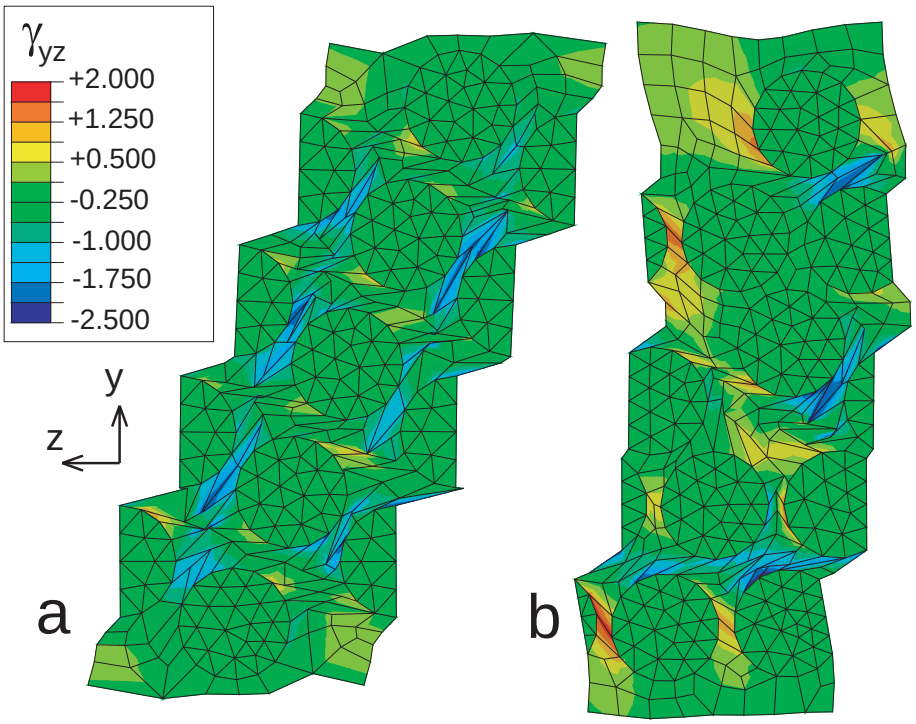

Figure 5.6: γ_{yz} strain field for $V_f = 55\%$: (a) hexagonal pattern and (b) random pattern

In the case of lower fiber volume fraction the results are similar, but the difference between the random and regular fiber arrangements is less marked (see Figure 5.7). In particular, the dependance of the buckling amplitude with respect to the thickness is similar for both arrangements, unlike the previous case.

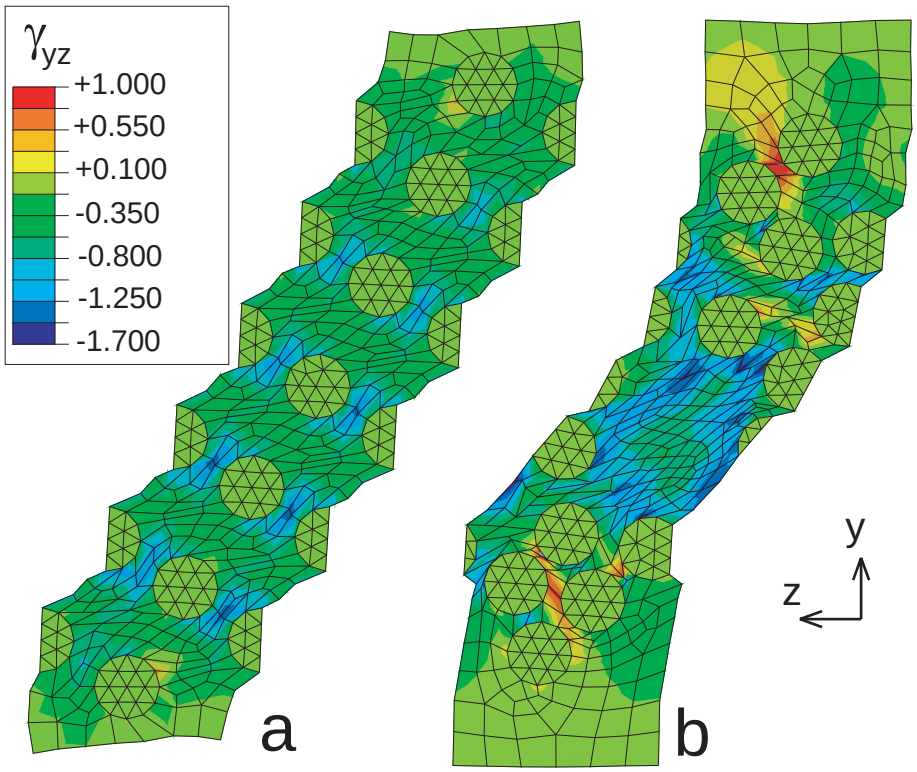

Figure 5.7: γ_{yz} strain field for $V_f = 30\%$: (a) hexagonal pattern and (b) random pattern

5.1.3 Moment vs. curvature

The higher strains observed in the cases with random fiber arrangement result in a stiffer model, as can be seen studying the moment-curvature relationship. In all plots, the curvature is assumed to be uniform through the material, and it is therefore calculated by dividing by L the rotation applied at the ends. Figure 5.8 shows the moment-curvature relationship of the simulations with $V_f = 55\%$. The cases with random fiber arrangement show some variation with each other, but they are clearly stiffer than the case with a hexagonal pattern. An analysis with linear geometry for the hexagonal pattern is also plotted for comparison. It coincides, as expected, with the initial response of all cases. Once the fibers have buckled, the stiffness of the regular pattern is roughly 20% of the initial, and 60–75 % in the case of the randomly arranged fibers.

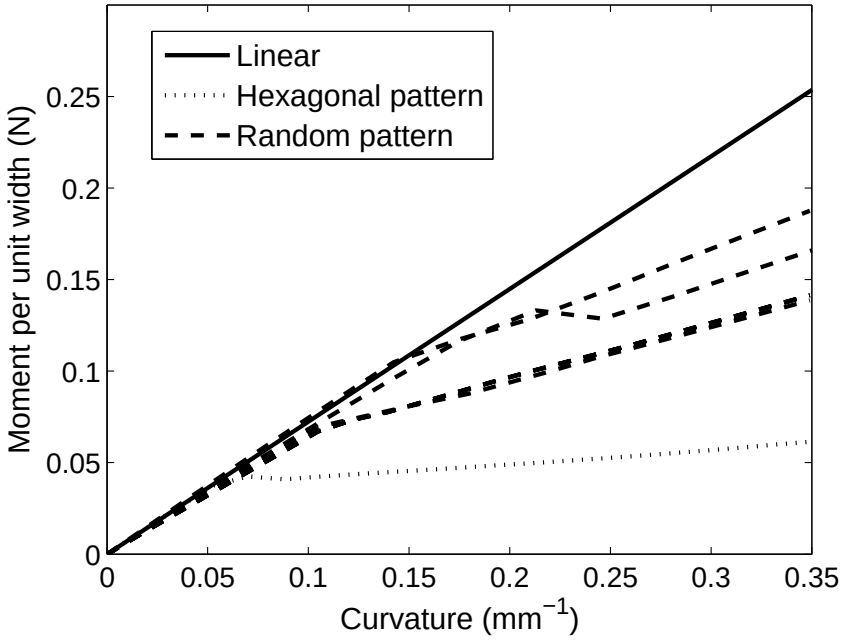

Figure 5.8: Moment vs. curvature for simulations with $V_f = 55\%$. The plot shows the results from the simulation with hexagonal fiber arrangement, four simulations with random fiber arrangement, and a linear analysis for reference

In the case of lower volume fraction (see Figure 5.9) the response of the regular and random fiber arrangements are much closer to each other, and both of them are much softer than the linear prediction. The sudden drop in stiffness is due to a not-smooth transition from the initial state to the post-buckled state, which produces a discontinuity in the first derivative of the strain energy. This is not likely to occur in the real material, due to the presence of imperfections, which will produce a smooth transition. The effect can be reduced by introducing waviness in the model, but it is not always possible to make it disappear completely.

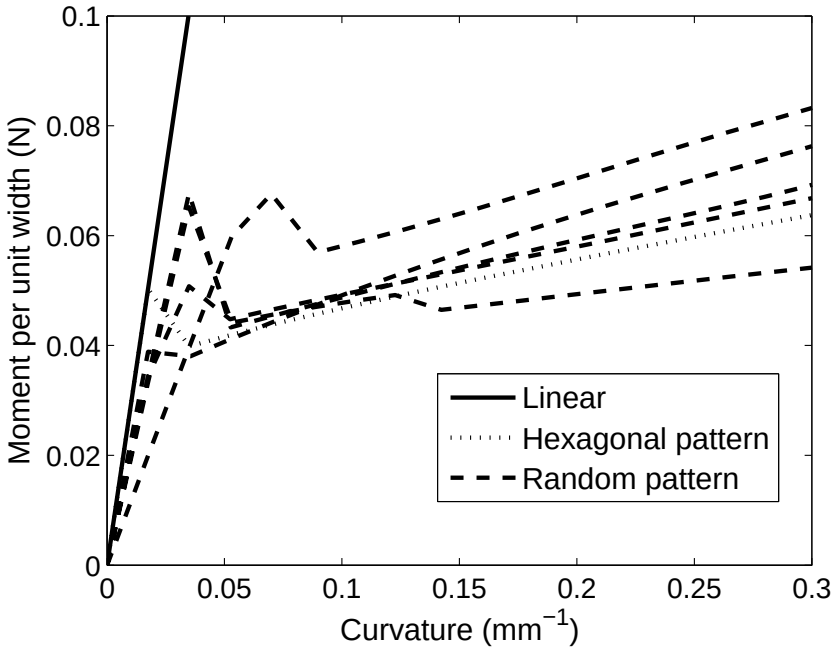

Figure 5.9: Moment vs. curvature for simulations with $V_f = 30\%$. The plot shows the results from the simulation with hexagonal fiber arrangement, three simulations with random RVE, and a linear analysis for reference

The results of the finite element analysis and the experiments are compared in Figure 5.10 and Figure 5.11, where the area enveloped by the simulations with random fiber arrangement has been shaded in grey. In the first case, $V_f = 55\%$, the prediction is much stiffer than the actually measured behavior. This is due to the damage taking place in the material. This is indicated not only by the presence of strain softening, but also by the unrealistically high strains observed in the matrix, see Figure 5.5.

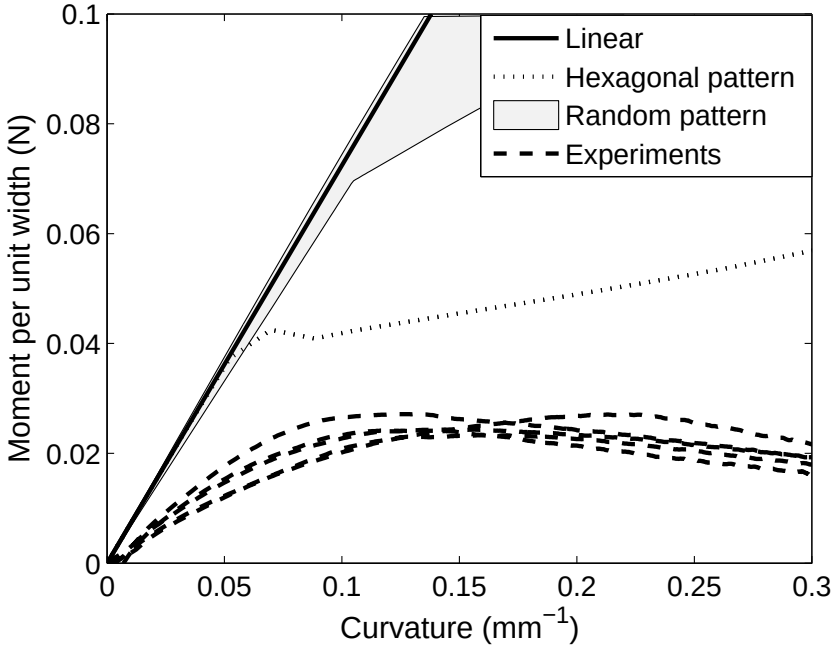

Figure 5.10: Comparison of moment vs. curvature in simulations and experiments for $V_f = 55\%$. The plot shows the results from the simulation with hexagonal fiber arrangement, the range spanned by the simulations with random RVE, and five experiments. A linear analysis has been added as a reference

In the case with 30% volume fraction, the test results lie within the region predicted by the simulations. The model provides a good prediction of the initial stiffness, as well as the curvature marking the transition to the nonlinear regimen. The post-buckled behavior is again stiffer in the finite element model. Although the conditions on the matrix are not as extreme as in the material with $V_f = 55\%$, strain softening is also present, which means that damage is taking place in the material.

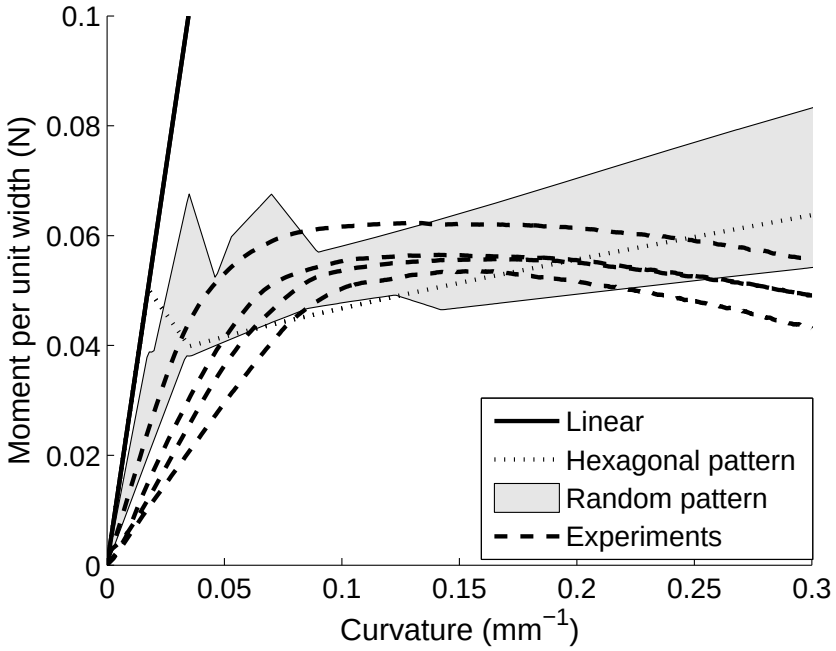

Figure 5.11: Comparison of moment vs. curvature in simulations and experiments for $V_f = 30\%$. The plot shows the results from the simulation with hexagonal fiber arrangement, the range spanned by the simulations with random RVE, and four experiments. A linear analysis has been added as a reference

5.2 Transverse tension—Perfect bonding

The linear responses of several RVEs have been calculated, for both purely random and reconstructed fiber distribution (see Figure 5.12). Five different cases have been studied for each one of the three fiber volume fractions considered. The average linear response is similar for the two sets of RVEs.

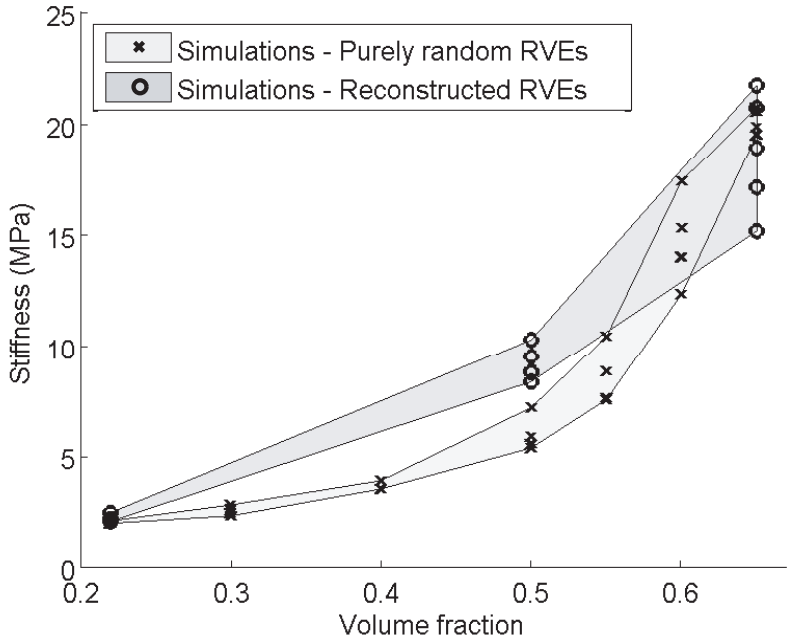

Figure 5.12: Linear stiffness obtained in simulations with purely random and reconstructed RVEs

The result of the simulations with reconstructed RVEs and the experiments are compared in Figure 5.13. The experimental results show an elastic modulus about 25% higher than those of the simulations for the same volume fraction. The difference can be attributed to the presence of misaligned fibers. Such fibers would carry part of the load in the longitudinal direction, increasing the overall stiffness in the material. Experimental observations of the material after failure suggest the presence of such fibers, see Section 3.6.

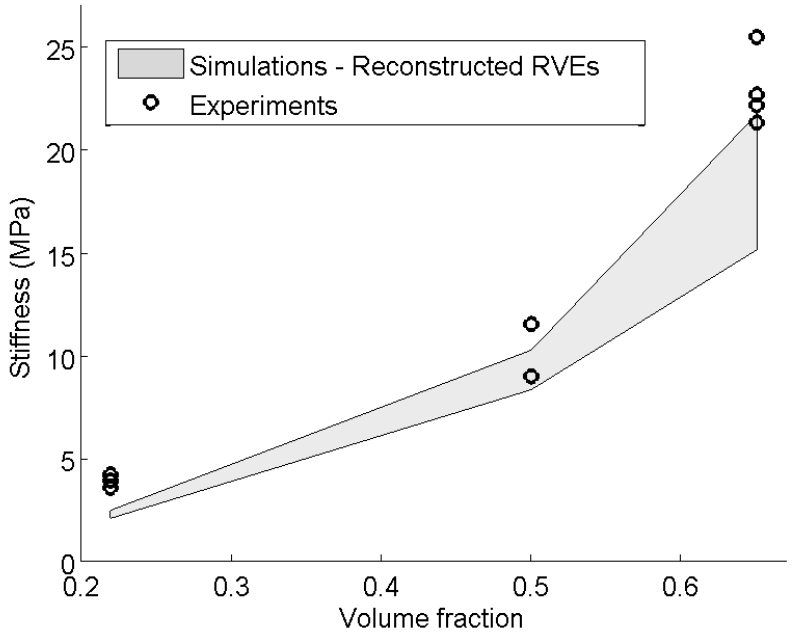

Figure 5.13: Linear stiffness obtained in reconstructed simulations and experiments

The simulations allow the study of the local stress and strain fields within the material. The strain field remains basically zero in the fibers, but very high strain concentrations in the matrix, particularly between very close fibers. There are several regions where the stress is between 10 and 50 times higher than the macroscopic applied strain for the case with $V_f = 65\%$ (see Figure 5.14).

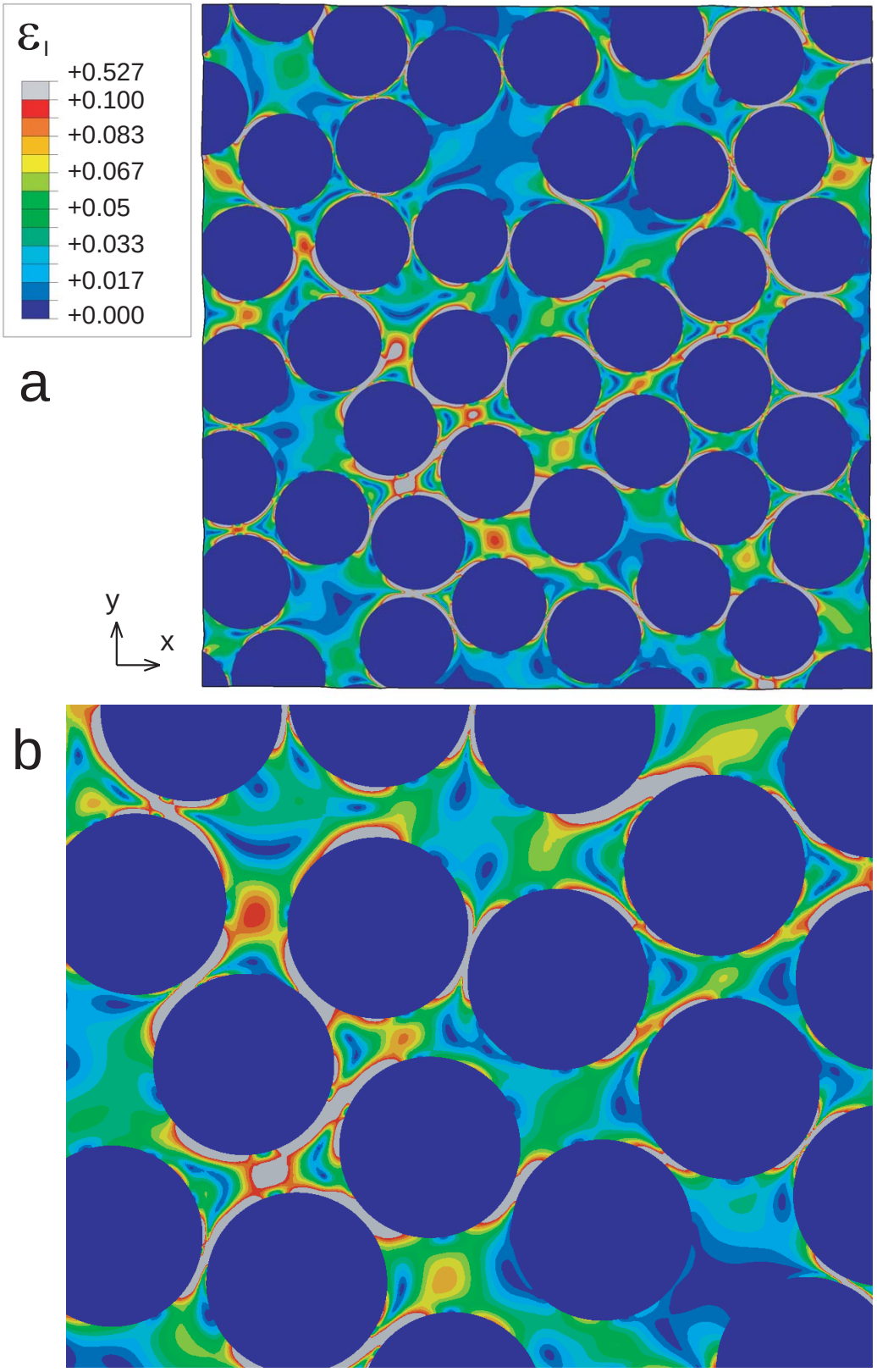

Figure 5.14: Maximum principal strain under 1% applied deformation. Reconstructed RVE, $V_f = 65\%$: (a) complete 50x50 μm RVE and (b) close up

Figure 5.15 shows the differences between a reconstructed and a purely random RVE with the same volume fraction. In the case of the RVE based on the micrographs the fibers tend to cluster more than in the purely random distribution, in which the distribution is more regular. This produces a higher strain concentration between the fibers, leading to a higher overall stiffness.

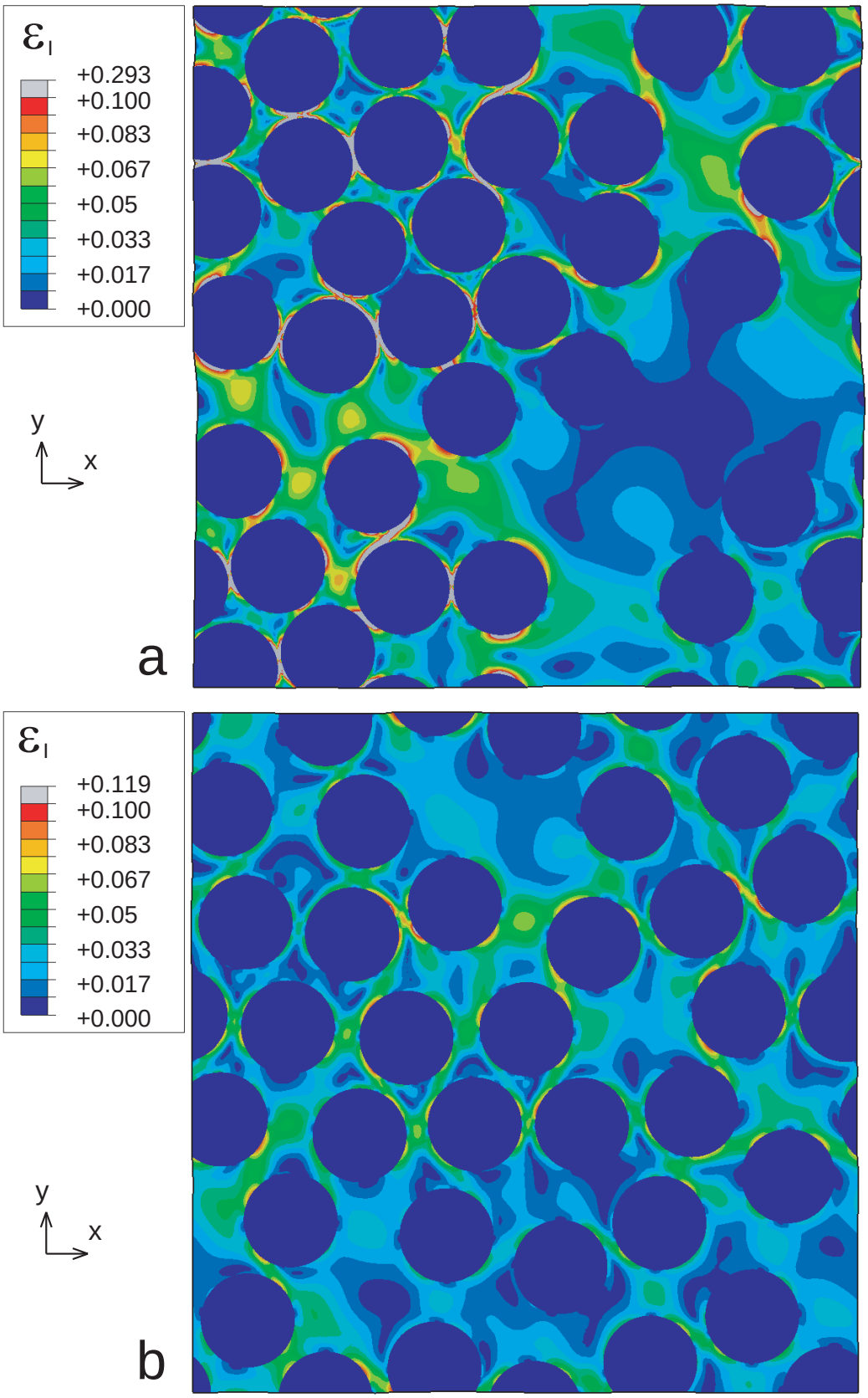

Figure 5.15: Maximum principal strain under 1% applied deformation. Reconstructed RVE, $V_f = 50\%$: (a) reconstructed RVE and (b) purely random RVE

Figure 5.16 shows the stress in the y direction in the case with $V_f = 65\%$, that is, the direction in which the average deformation is applied. In this case the plot shows the load transmission path, and the high stress concentration in the matrix between very close fibers due to incompressibility.

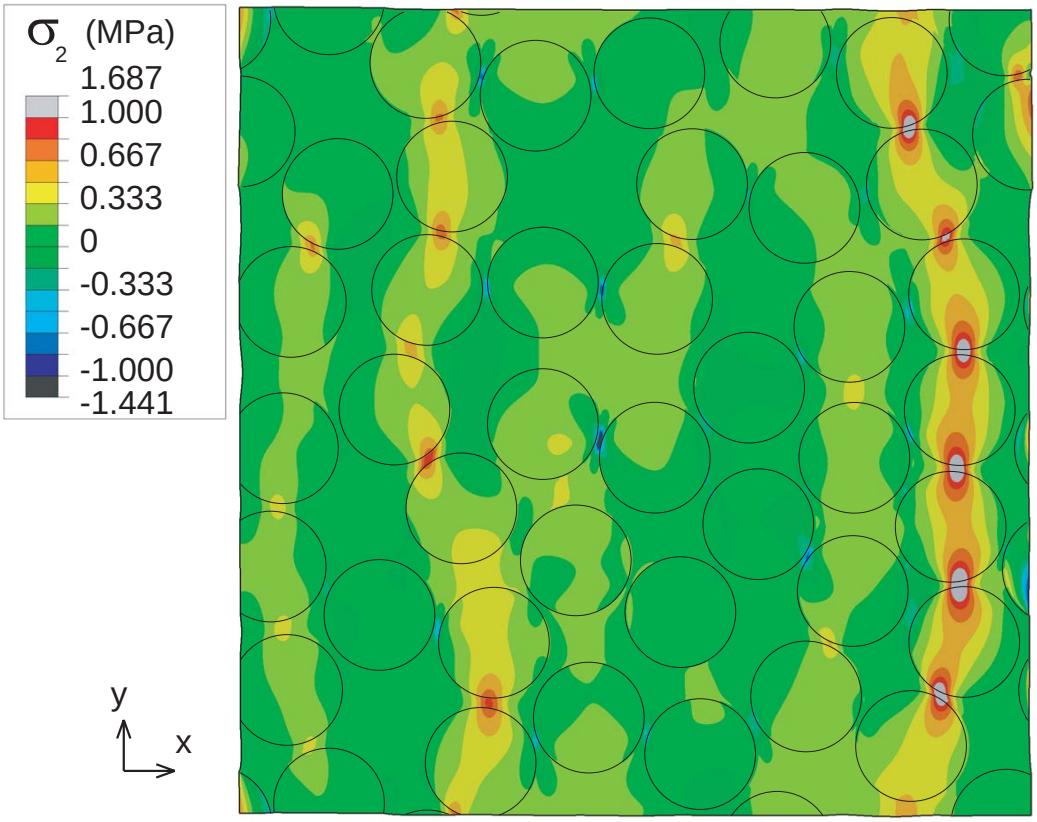

Figure 5.16: Stress in the loading direction under 1% applied deformation. Reconstructed RVE, $V_f = 65\%$

The simulations are unable to capture the behavior once the nonlinearity begins (see Figure 5.17). In order to capture this effect, as well as the stress softening, cohesive elements are introduced between fibers and matrix.

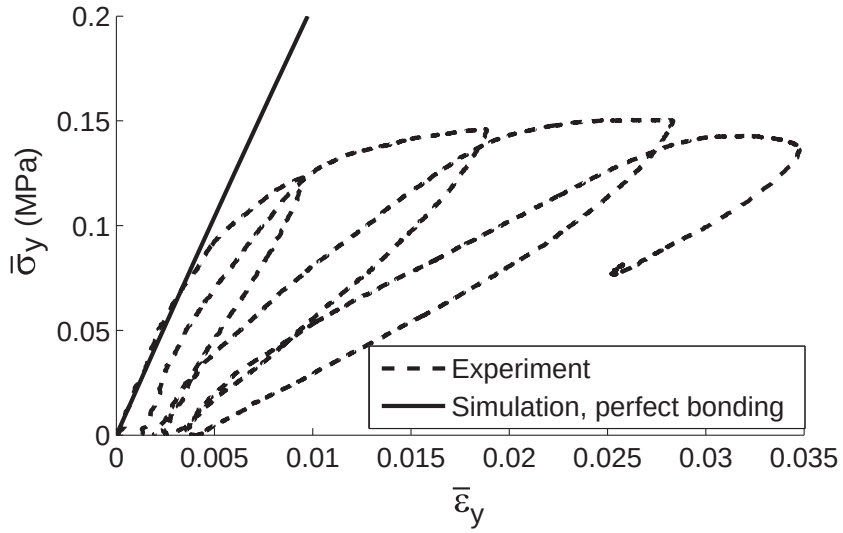

Figure 5.17: Stress vs. strain under transverse loading: experiment and simulation (reconstructed RVE, $V_f = 65\%$) with perfect bonding

5.3 Transverse tension—Debonding allowed

Cohesive elements are introduced in the model to model the debonding between fibers and matrix. In order to reduce the influence of the cohesive elements before damage takes place, their initial stiffness is set to 100 GPa (five times the transverse stiffness of the fibers), which guarantees almost perfect bonding between matrix and fibers before damage takes place.

The failure behavior of the cohesive elements available in ABAQUS have three main parameters: the condition for damage initiation, the separation δ_f at which the stiffness of the cohesive element is equal to zero, and the damage evolution. In this work, the condition for damage initiation in the cohesive elements was given as a quadratic combination of the tractions, that is, damage will occur when:

$$\left(\frac{t_n}{t_{n0}}\right)^2 + \left(\frac{t_s}{t_{s0}}\right)^2 = 1 \tag{5.1}$$

where t_n and t_s are the normal and shear components of the nominal traction stress vector and t_{n0} and t_{s0} are two normalizing factors. In the results presented here, the same factor was used for all tractions, $t_{n0} = t_{s0} = t_0$. However, different values were

used in preliminary analysis, with the goal of finding out the relative importance of every stress term. It was found that t_n is the leading term regarding damage initiation. Models considering only t_n showed no difference in damage initiation than those that take into account the two stress components. However, the part of the simulations concerning damage growth is numerically more stable in the second case, meaning that t_s plays a more important role in the evolution of damage once it is initiated.

Regarding the separation δ_f, two main behaviors were found. The first one corresponds to separations ranging from 1 μm to values higher than the fiber diameter, such as 100 μm. In this case, the response of the system is fairly independent of the actual value used (see Figure 5.18). The reason is not only that the cohesive elements introduce a limit in the stress in the material, but also that a very small opening between fibers and matrix is able to relax the constraints in the material due to the matrix incompressibility. When the value of δ_f is small compared to the fiber radius, the reduction is much larger. In this case, the opening taking place between fiber and matrix is enough to produce a large decay in the stress, and in some cases result in complete debonding.

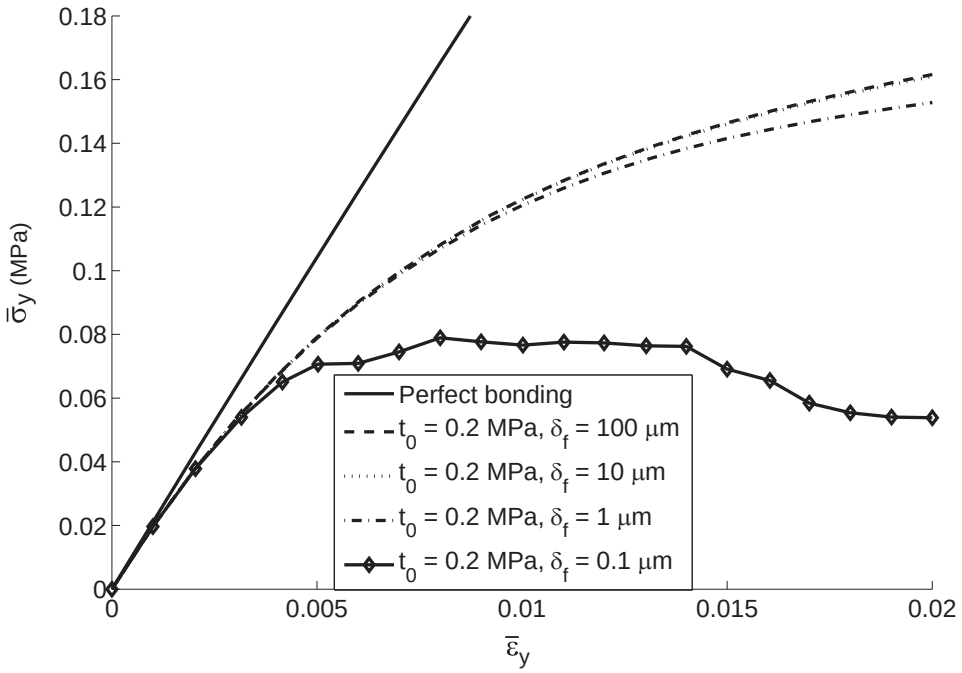

Figure 5.18: Stress vs. strain under transverse loading for different values of δ_0, reconstructed RVE, $V_f = 65\%$

The model shows a better agreement with the experimental results with low values of δ_f. In that case, the dependance of the solution with respect to t_0 is shown in Figure 5.19. As expected, an increase in t_0 delays the start of the nonlinearity, and lowers the total stress.

The simulation with $t_0 = 0.1$ MPa shows a decrease in stress for strains higher than 0.015. This can be used as an indication of the initiation of failure in the composite, which, as was seen in Section 3.6, is not an instantaneous process.

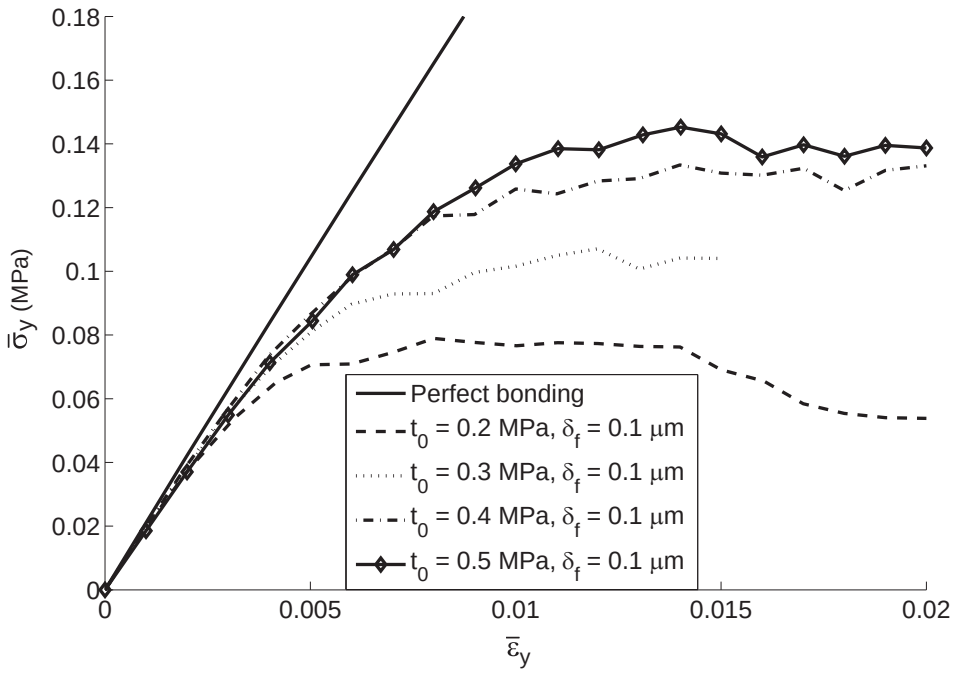

Figure 5.19: Stress vs. strain under transverse loading for different values of t_0, reconstructed RVE, $V_f = 65\%$

Finally, the damage evolution in ABAQUS can be linear or exponential with respect to the separation. The previous results were produced with models with linear damage growth. Using an exponential did not change the results.

All the previous results have been obtained with the same mesh in the same RVE. Figure 5.20 shows a comparison between experiments and simulations, all of them with $V_f = 65\%$, and fiber arrangements obtained from micrographs. The numerical results provide a very good approximation of the test results. The response in the simulations is not completely smooth due to the reduced number of fibers: when one of them debonds,

the stiffness of the material drops, and then it rises again as more strain is applied. This effect will be reduced using a much larger RVE, where the effect of the debonding of a single fiber will be much less.

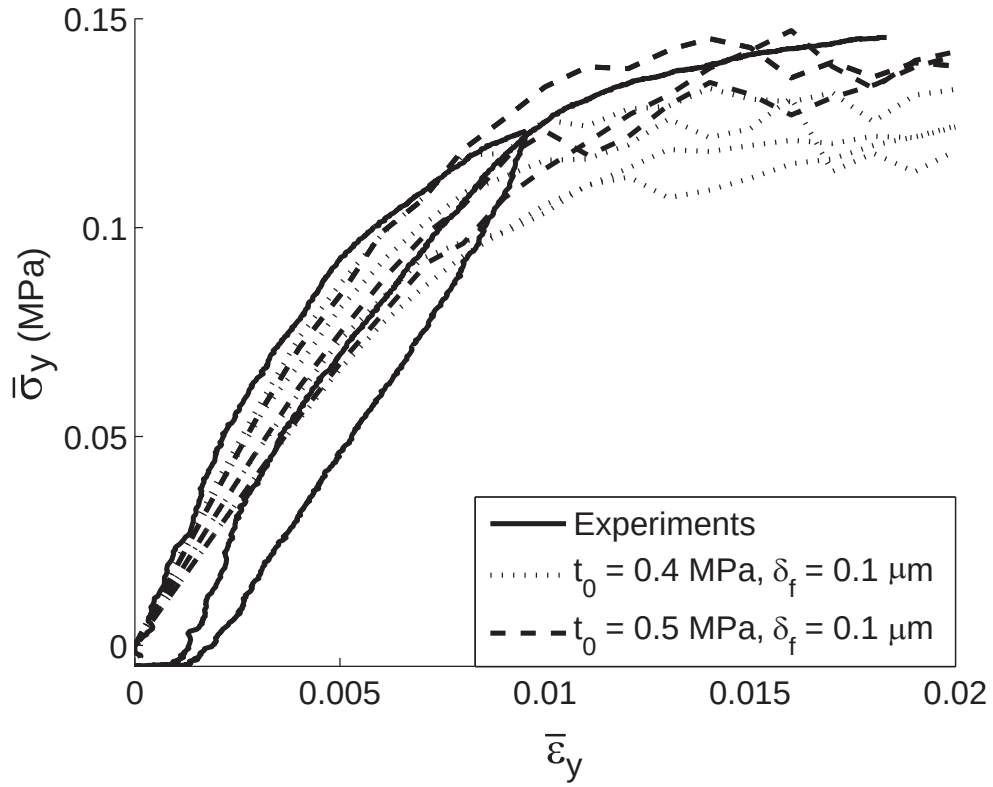

Figure 5.20: Stress vs. strain under transverse loading for experiments and simulations using different reconstructed RVEs, $V_f = 65\%$

If a loading-unloading cycle is applied, the model shows permanent damage, due to the degradation of the cohesive elements (see Figure 5.21). There are several differences with respect to the experiments, mainly due to the fact that, as long as no damage is being generated, the cohesive elements behave elastically. Therefore there is no hysteresis, nor permanent deformation, and the unloading-reloading path is basically a straight line until new damage occurs. The model is still able to provide a very good prediction of the experimental behavior.

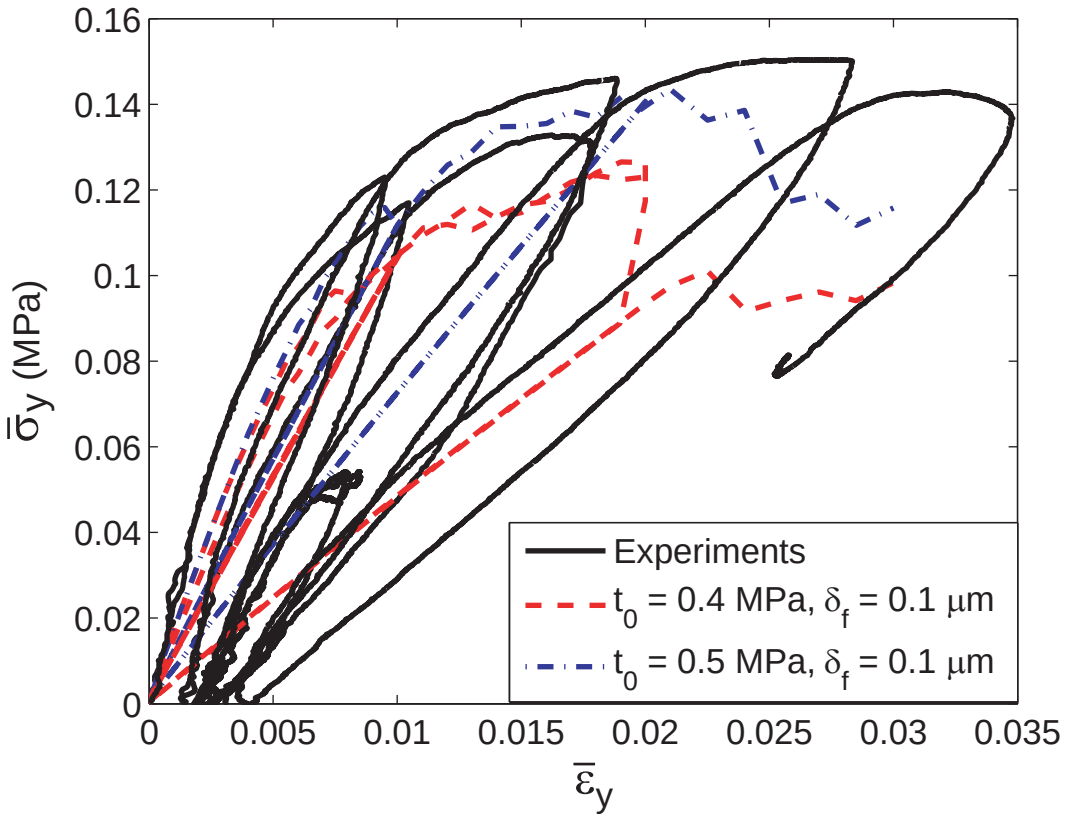

Figure 5.21: Stress vs. strain under cyclic transverse loading for experiments and simulations using different reconstructed RVEs, $V_f = 65\%$

If the same cohesive elements are applied to the model with $V_f = 22\%$, the behavior observed is very different, as it was in the experiments. The nonlinearity appears at a much higher strain, and the hysteresis is very low. Figure 5.22 shows a comparison of numerical and experimental results. The initial stiffness obtained with the model is about half of the test results, which explains the disagreement. The qualitative behavior, however, is well captured.

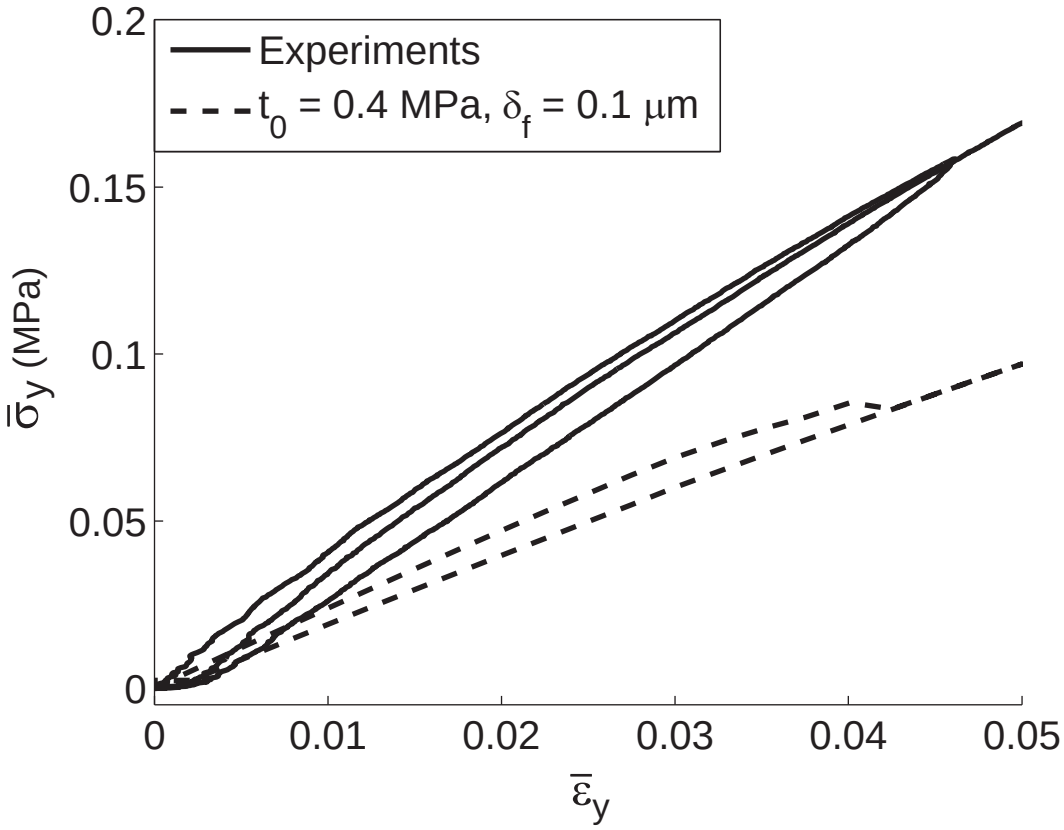

Figure 5.22: Stress vs. strain under cyclic transverse loading, $V_f = 22\%$

The simulations can be used again to look at the microscopic stress and strain fields. Figure 5.23 and Figure 5.24 show the maximum principal strain and the stress in the loading direction when cohesive elements are introduced in the simulations presented in Figures 5.14 and Figure 5.16 in the case of perfect bonding. The same scale has been kept for an easier comparison. The strains have approximately the same values, although the distribution is different. The corresponding stresses are much lower, as is to be expected with the inclusion of the cohesive elements.

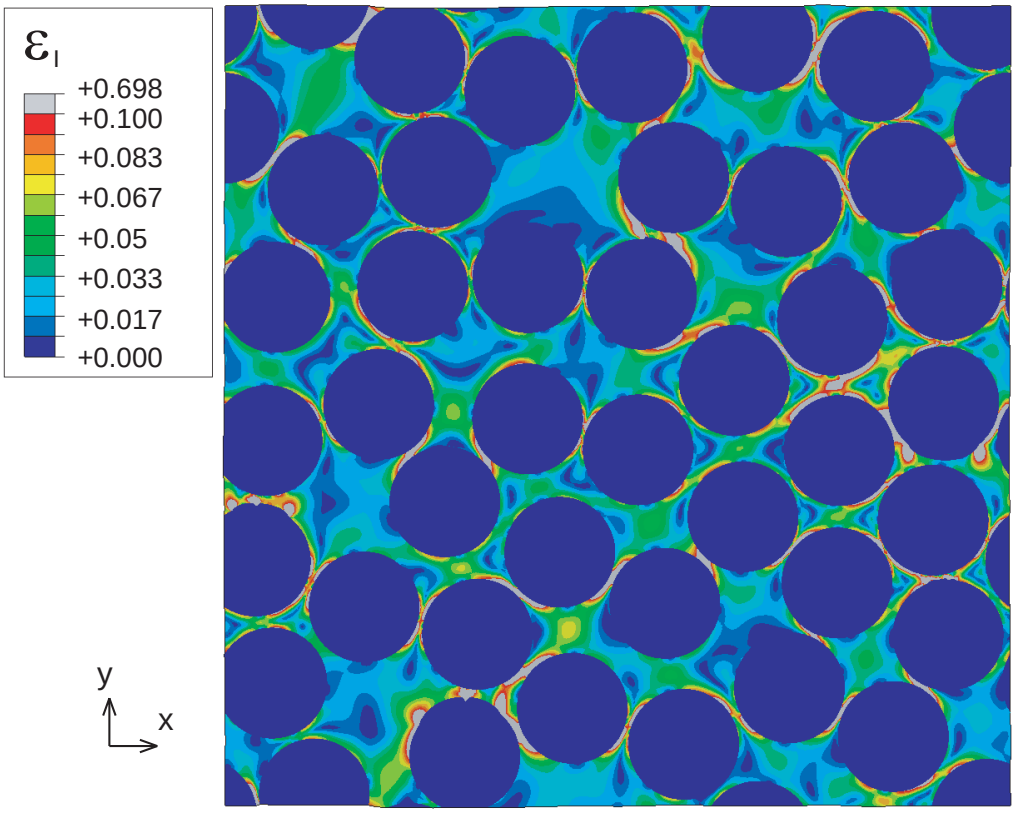

Figure 5.23: Maximum principal strain under 1% applied deformation. Reconstructed RVE, $V_f = 65\%$, cohesive elements introduced between fibers and matrix

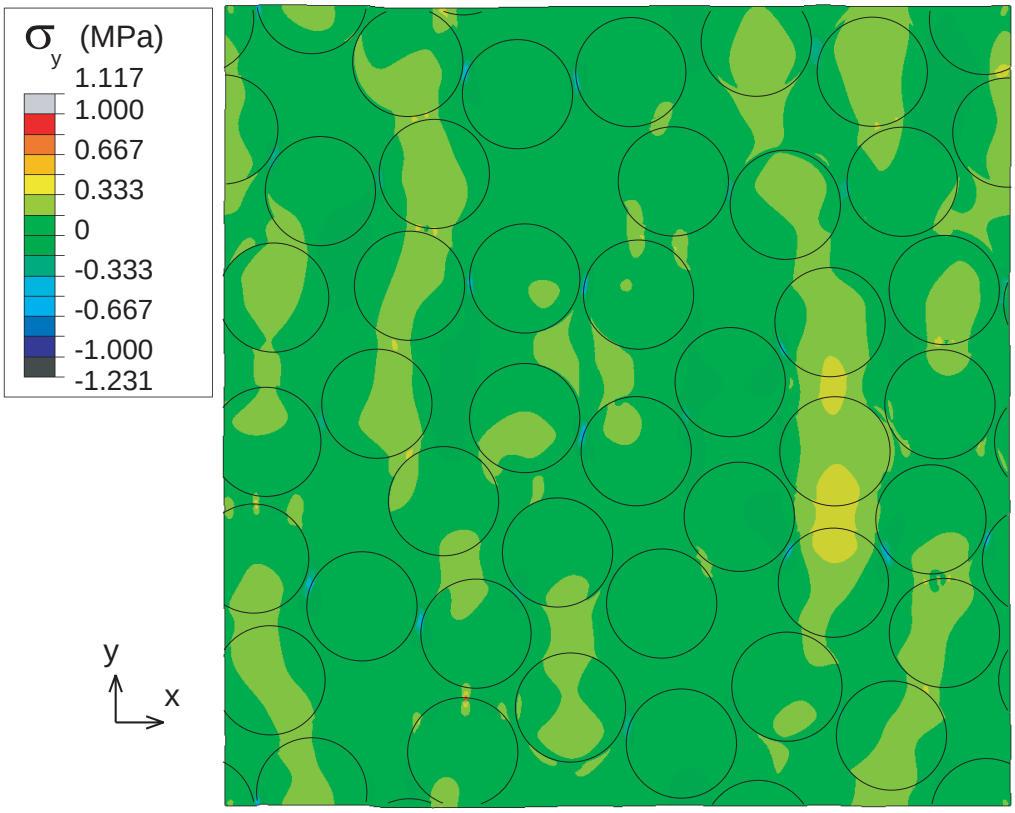

Figure 5.24: Stress in the loading direction under 1% applied deformation. Reconstructed RVE, $V_f = 65\%$, cohesive elements introduced between fibers and matrix

The stresses are not only lower, but they follow a much different distribution than in the simulations with perfect bonding. If the scale is changed according to the new stress levels, Figure 5.16 shows that the highest stress no longer take place between the closest fibers, since the corresponding cohesive elements have degraded more than those in regions where the fibers are more spread out.

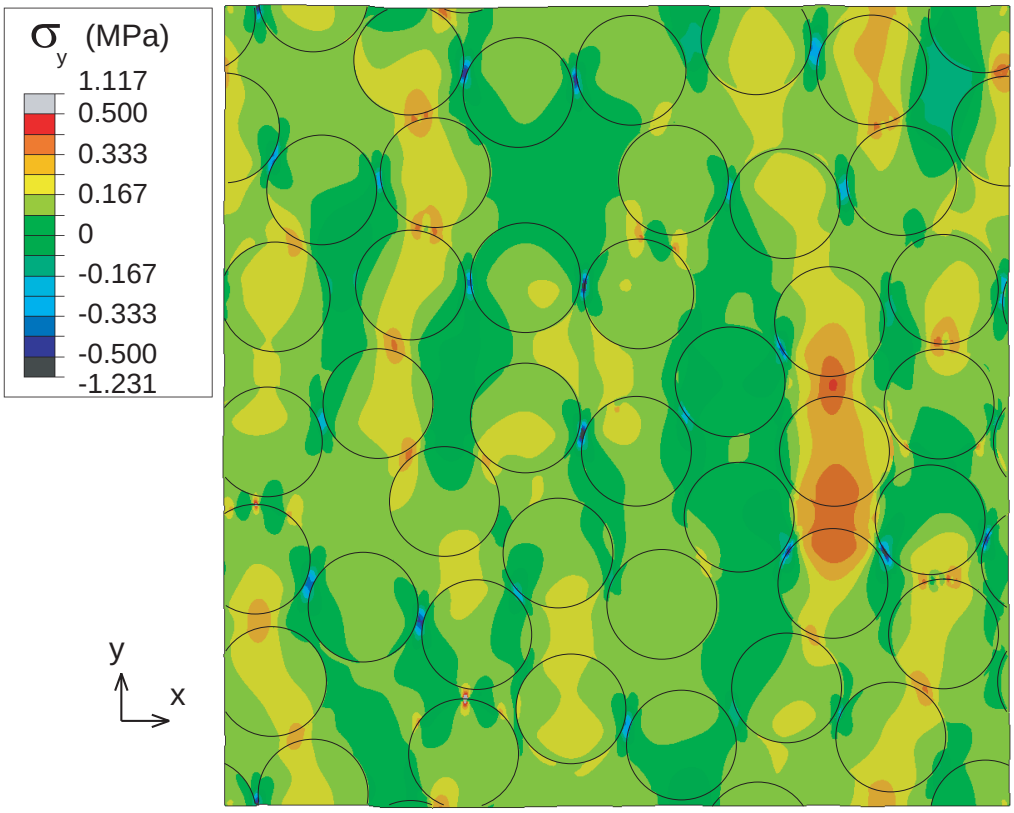

Figure 5.25: Stress in the loading direction under 1% applied deformation. Reconstructed RVE, $V_f = 65\%$, cohesive elements introduced between fibers and matrix

As it was stated in Section 3.1 and Section 5.1.2, no failure criteria for silicone rubber under multi-axial loading has been created, and key failure processes in rubbers, such as cavitation, have not been studied for silicone rubber. However, the values of the principal strain observed in the simulations are well beyond the failure point observed in uniaxial testing. Although these results cannot be used to assess the integrity of the material, it suggests that the debonding mechanism reduces the strain in the matrix to acceptable levels.

5.4 Comparison with traditional composites

The behavior of composites with silicone matrix differs from traditional epoxy composites in the loading modes in which the behavior of the fibers is not dominant. If tension along the fibers is applied, no difference can be observed. In the case of bending, composites

with epoxy show linear stiffness until failure occurs, without the nonlinearity due to fiber microbuckling that takes place in composites with a soft matrix. In both cases, however, the initial linear stiffness is the same, given mainly by the stiffness of the fibers.

The situation is very different for tension transverse to the fibers, where the matrix behavior is what determines the average response of the material. This can be observed by comparing the linear stiffness with the predictions obtained with traditional composite theory. There exist several approximations for the transverse stiffness of composite materials (Jones, 1999). The rule of mixtures provides the most basic one, as it treats the fiber and the matrix as two solids which are in parallel in the case of tension along the fibers, and in series in the case of loading perpendicular to the fibers. This gives a transverse stiffness of

$$E_2 = \frac{E_{2f} E'_m}{V_m E_{2f} + V_f E'_m} \tag{5.2}$$

where V_f and V_m are the fiber and matrix volume fractions, $E_2 f$ is the transverse stiffness of the fibers, and E'_m is equal to

$$E'_m = \frac{E_m}{1 - \nu_m} \tag{5.3}$$

where E_m and ν_m are the properties of the matrix, which is assumed to be isotropic.

This analysis largely neglects the geometric complexities of the material, and serves as a rough lower bound. A much closer approximate can be obtained through the Halpin-Tsai equations (Halpin and Kardos, 1976), which constitutes a series of semi-empirical estimates for the properties of composites. In the case of stiffness transverse to the fibers, the expression provided is

$$E_2 = E_m \frac{1 + \eta \xi V_f}{1 - \eta V_f} \tag{5.4}$$

where the parameter η is defined as

$$\eta = \frac{E_{2f} - E_m}{E_{2f} + \xi E_m} \tag{5.5}$$

and ξ is a parameter to be fitted experimentally, whose value usually ranges from 1 to 2.

In order to study the validity of those approximations in the case of composites with hyperelastic matrix, Figure 5.26 shows the comparison between numerical results, the rules of mixtures, and the Halpin-Tsai prediction. The value used for the matrix stiffness is the initial tangent modulus of the silicone under uniaxial tension, $E_m = 6C_1 + 2C_2 = 0.9048$ MPa, and the Poisson's factor is that of incompressible materials, $\nu_m = 0.5$. In order to increase the number of values of the volume fraction for which numerical results are available, the simulations were produced with purely random RVEs, i.e., no information from the micrographs was used. The simulations were repeated using the same fiber arrangement and mesh, but modeling the matrix as a typical epoxy usually used in composites, with $E_m = 4.5$ GPa and $\nu_m = 0.35$. In both cases the response is normalized by the elastic modulus of the matrix.

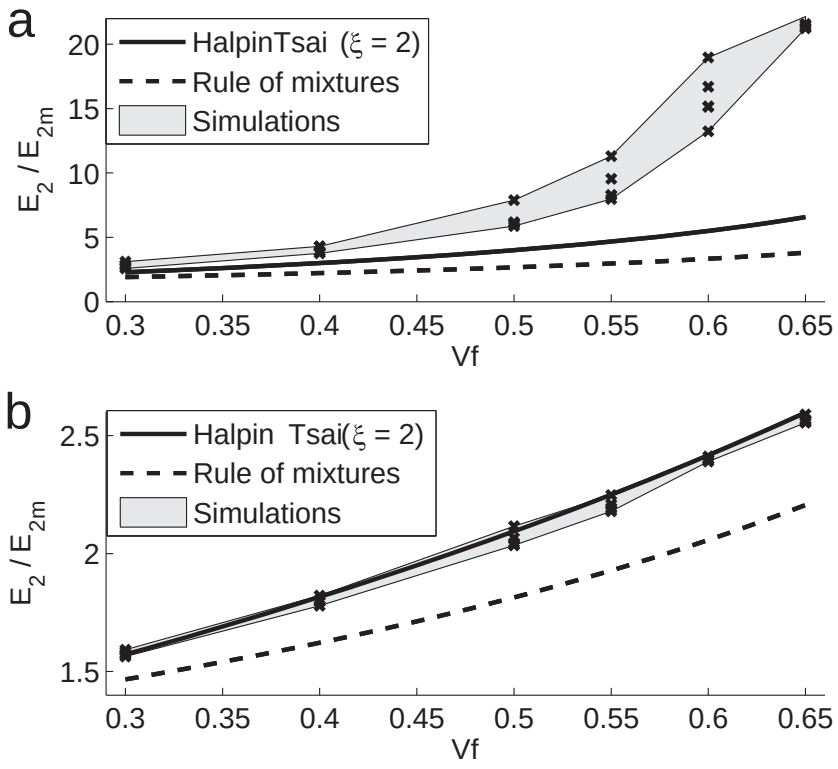

Figure 5.26: Transverse stiffness of a composite. Simulations with random RVEs and analytical predictions for composite with: (a) silicone matrix and (b) epoxy matrix

The results show two main differences. The first is the value of the increase in stiffness with respect to the matrix values, and its dependance with respect to the volume fraction. The normalized stiffness of the composite with silicone matrix reaches a value of more than 20, and it grows much more rapidly with respect to the volume fraction. This behavior is also very different from the Halpin-Tsai prediction. Attempts to increase the value of ξ were still not able to reproduce the dependance on volume fraction observed in the simulations.

The second difference is the much greater spread in stiffness in the simulations with silicone matrix than in those with epoxy. In the case of 60% volume fraction the extreme values differ up to 20% in either direction of the mean value of the five simulations. It must be noted that the same RVEs and meshes have been used in the two sets of simulations. Even if the spread is much smaller, the simulations providing a higher stiffness in the case of silicone matrix also present a higher stiffness when the matrix is epoxy (see Table 5.2).

There are two possible explanations for this difference of behaviors: the extreme dis-

Case	Silicone	Epoxy
Mesh 1	11.31	2.25
Mesh 2	8.29	2.19
Mesh 3	8.24	2.19
Mesh 4	7.97	2.18
Mesh 5	9.55	2.21

Table 5.2: Linear stiffness for silicone and epoxy simulations, normalized by the Young's modulus of the matrix. Volume fraction 55%, purely random fiber arrangement

parity of stiffness between fiber and silicone matrix, and the incompressible nature of the silicone. In order to study both options, two new sets of simulations was produced using the same RVEs and different matrix properties (see Figure 5.27). The first one models the matrix as a linear material with $\nu_m = 0.35$ and stiffness equal to the tangent modulus of the silicone, $E_m = 0.9048$ MPa. In this case the material could be fitted with the Halpin-Tsai equation using $\xi = 1.5$, which lies in the usual range of the parameter. In the second case the matrix retains the elastic modulus of epoxy, $E_m = 4.5$ GPa, but adding incompressibility. In this case the stiffness gain is much higher than in the case of compressible epoxy, and the Halpin-Tsai equation with $\xi = 2$ produces a poor prediction. If a value of $\xi = 25$ is used, the prediction is much better, and able to capture the dependance on high-volume fractions. It should be noted, however, that the value is well beyond the usual range.

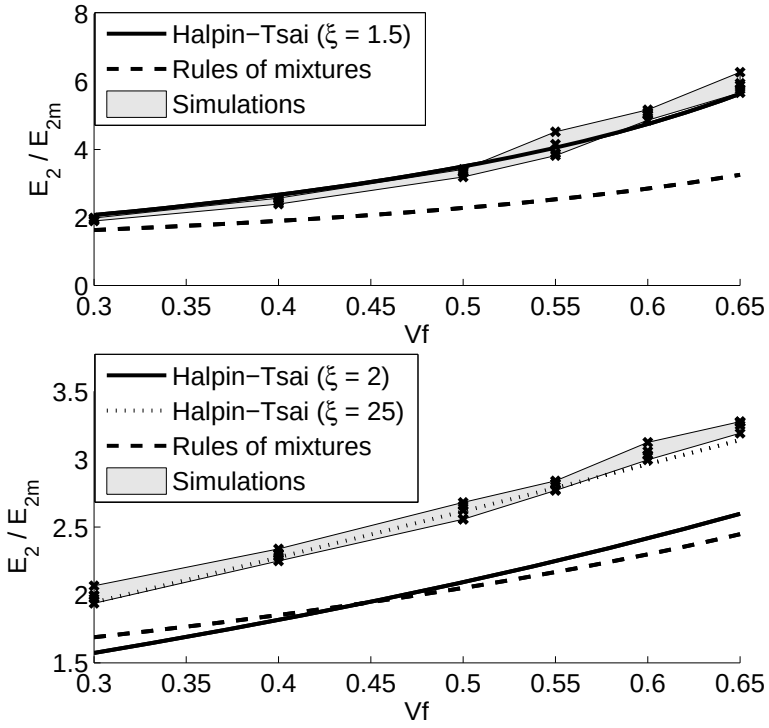

Figure 5.27: Transverse stiffness, simulations, and analytical stiffness. Matrix properties: (a) $E_m = 0.9048$ MPa, $\nu_m = 0.35$, and (b) $E_m = 4.5$ GPa, $\nu_m = 0.5$

Therefore, incompressibility alone is enough to produce some deviation from the usual behavior of composites, but the effect is much more important when combined with a matrix that is several orders of magnitude softer than the fibers. In particular, the large spread in the response is only seen when both effects are present.

Finally, the simulations can be also compared to the Hashin-Rosen bounds (Hashin and Rosen, 1964), an application for the case of fiber composites of the Hashin-Shtrikman bounds to heterogeneous materials. The bounds use the bulk modulus of the matrix as a parameter. Several values have been calculated using the linear stiffness of the silicone and different values for the Poisson's ratio (0.4, 0.49, 0.499, and 0.4999). The upper bounds are highly dependent on the value of ν_m, although it shows convergence for values very close to the incompressibility limit. The lower bound, on the other hand, shows no dependency on ν_m. The values obtained for Poisson's ratios higher than 0.49 work as bounds for the numerical results (see Figure 5.28). However, the disparity between higher and lower bounds is too high to be used in the design of a structure using fiber-reinforced

rubbers.

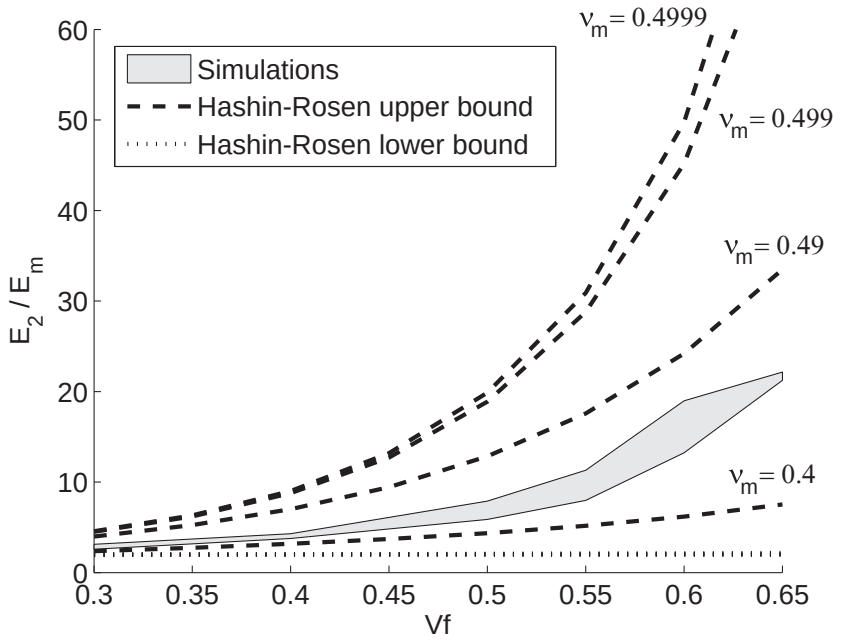

Figure 5.28: Transverse stiffness, simulations, and Hashin-Rosen analytical bounds. The stiffness used for the matrix is $E_m = 0.9048$ MPa, and the Poisson's ratio is specified in the figure

Chapter 6

Analytical Model

This chapter presents an analytical study of the bending mechanics of a thin fiber composite with a very compliant matrix, with the goal of creating tools to be used in the design of structures using this type of composite. It is a linearized model similar to the works of Rosen (1965) and Francis (2008). Even if this model makes several simplifying assumptions, it captures a qualitative description of the material behavior, and it is useful to understand the mechanics involved in the process. Quantitatively, the model provides a better approximation in the case of low-volume fractions, as with the numerical simulations.

6.1 Model geometry and kinematics

A thin composite material is considered. It has the form of a thin plate of thickness t, extending in the $x-y$ plane, with the fibers aligned in the x direction. The fibers are assumed to be perfectly parallel, and homogeneously distributed though the material.

This composite is then folded around the y axis. It is assumed that the curvature is uniform through the material. The neutral surface coincides with the middle surface until buckling in the compressed fibers appears. This buckling will take the form of buckles in the y direction, with a wavelength λ. The expression of the buckles is then:

$$\delta = a(z) \sin \frac{\pi x}{\lambda} \tag{6.1}$$

where $a(z)$ is the amplitude of the sine for a given value of the through-the-thickness

coordinate z.

It is assumed that the buckled fibers are not stretched or compressed. As detailed in Chapter 2, Francis (2008) gave an approximation of the required sine amplitude:

$$a(z) = \frac{2\lambda}{\pi}\sqrt{-\epsilon_x} = \frac{2\lambda}{\pi}\sqrt{\kappa(z - z_n)} \tag{6.2}$$

where ϵ_x is the homogenized strain and z_n is the position of the neutral axis.

Not all the compressed fibers need to buckle. In particular, the coordinate z_b marks the position of the first buckled fibers. The buckled material is then divided into three areas: straight fibers under tension, straight fibers under compression, and buckled fibers. The position of z_n and z_b needs to be calculated during the analysis, as discussed in Section 6.3

6.2 Pre-buckled configuration

In the pre-buckled configuration it is possible to model the material as a homogenized material using the rule of mixtures:

$$E_x = V_f E_f + V_m E_m \tag{6.3}$$

where E_f and V_f are the elastic modulus and volume fraction of the fibers, and E_m and V_m are the same properties for the matrix.

The moment M applied on the material is then given by

$$M_{pre} = EI\kappa = \frac{1}{14}E_x t^3 \kappa \ . \tag{6.4}$$

This state will apply as long as the material strain energy W_{pre}, with expression:

$$W_{pre} = \frac{1}{2}M\kappa = \frac{1}{2}E_x I\kappa^2 = \frac{1}{24}E_x t^3 \kappa^2 \tag{6.5}$$

is lower than the energy of the buckled configuration.

6.3 Buckled configuration

The first step to analyze the buckled configuration of the material is to obtain all the relevant strain energy terms. Once the total strain energy of the material W_{post} has been obtained, the moment can be calculated as:

$$M_{post} = \frac{\partial W_{post}}{\partial \kappa} \ . \tag{6.6}$$

6.3.1 Material with straight fibers

This region of the material can still be modeled using the equations described in Section 6.2. The strain energy is then equal to:

$$W_{str} = \frac{E_x \kappa^2}{6} \left((z_b - z_n)^3 + \left(\frac{t}{2} + z_n \right)^3 \right) \ . \tag{6.7}$$

6.3.2 Buckled fibers

The energy per unit length of a single fiber buckled following the sinusoidal kinematics described in Section 6.1 will have strain energy:

$$W_{1f}(z) = \frac{\pi^4 E_f I_f a^2(z)}{4\lambda^4} \tag{6.8}$$

where E_f and I_f are the elastic modulus and second moment of inertia of the fibers.

The distribution of fibers is assumed to be homogeneous through the material. The fiber density is then equal to:

$$\rho_f = \frac{V_f}{\pi r_f^2} \tag{6.9}$$

where r_f is the fiber radius. The strain energy per cross-section unit due to the buckled fibers is then equal to:

$$W_{f,area} = \frac{\pi^3 E_f I_f a^2(z) V_f}{4\lambda^4 r^2} \ . \tag{6.10}$$

Integrating over the region in which fibers are considered buckled, the total strain energy of the buckled fibers is then:

$$W_f = \frac{\pi^2 E_f I_f V_f \kappa}{2\lambda^2 r^2} \left(\left(\frac{t}{2} - z_n \right)^2 - (z_b - z_n)^2 \right) . \tag{6.11}$$

6.3.3 Strain energy of the matrix

The are two shear strain terms in the matrix, γ_{xy}, which is created when the matrix shears between two fibers with the same deflection (i.e., the same z coordinate), and γ_{yz}, due to shearing between two fibers with different deflection (different value of z):

$$\gamma_{xy} = \frac{\partial \delta}{\partial x} = \frac{a(z)}{\lambda} \cos\left(\frac{x}{\lambda}\right) \tag{6.12}$$

$$\gamma_{yz} = \frac{\partial \delta}{\partial z} = a'(z) \sin\left(\frac{x}{\lambda}\right) = \frac{\lambda}{\pi} \sqrt{\frac{\kappa}{z - z_n}} \sin\left(\frac{x}{\lambda}\right) . \tag{6.13}$$

The strain energy due to γ_{xy} is equivalent to the one given by Rosen (1965):

$$W_{xy} = \frac{V_m G_m \kappa}{2} \left(1 + \frac{r}{h}\right)^2 \left(\left(\frac{t}{2} - z_n \right)^2 - (z_b - z_n)^2 \right) \tag{6.14}$$

where h is the distance between two fibers. The value corresponding to a hexagonal distribution has been used during this analysis.

The strain due to γ_{yz} is a term that only appears in cases where the buckling is not homogeneous, such as bending, as noted by Francis (2008).

$$W_{yz} = \frac{V_m G_m \kappa \lambda^2}{\pi^2} \log\left(\frac{\frac{t}{2} - z_n}{z_b - z_n} \right) \tag{6.15}$$

6.3.4 Jump condition

The deflection of the fibers is not continuous, since $\delta(z)$ goes from zero to a finite value at z_b. An additional strain term has been introduced to penalize this jump. It takes into account the shear of the material due to the discontinuity in δ, defined over the inter-fiber

distance h:

$$W_{jump} = \frac{4G_m V_m \lambda^2}{\pi^2 h} (z_n - z_b) \ . \tag{6.16}$$

6.3.5 Total energy

The total strain energy of the buckled configuration is formed by adding all the previous terms:

$$W_{post}(\lambda, \kappa, z_n, z_b) = W_{str} + W_f + W_{xy} + W_{yz} + W_{jump} \ . \tag{6.17}$$

The energy then needs to be minimized with respect to the variables λ, z_n, and z_b. The moment is then calculated using Equation 6.6. The expression of the total energy will be the minimum between W_{pre} and W_{post}, and the moment will the combination of the corresponding moments:

$$M = \begin{cases} M_{pre} & \text{if } W_{pre} \leq W_{post} \\ M_{post} & \text{if } W_{pre} > W_{post} \ . \end{cases} \tag{6.18}$$

Note that the expression obtained for W is not convex, and so the moment will have a discontinuity.

6.4 Results

This section presents the application of the model previously described to the two specimens used during the experimental testing: unidirectional one-ply specimens with $V_f = 30\%$ (approximate thickness 80 μm) and $V_f = 55\%$ (approximate thickness 40 μm).

Figure 6.1 shows a comparison of predicted and experimental moment vs. curvature relationships for the specimen with $V_f = 30\%$. The model clearly overestimates the stiffness of the specimens, including the initial linear stiffness. This is due to the fact that the homogenization technique used assumes that the fibers are distributed uniformly, which is unrealistic: large sections of pure silicone can be observed at the top and bottom surfaces of the composite. Since this section of the material will have a larger contribution

to bending, assuming that fibers are present will greatly increase the overall stiffness. This effect is of particular importance in the case of very thin composites, such as the ones studied here.

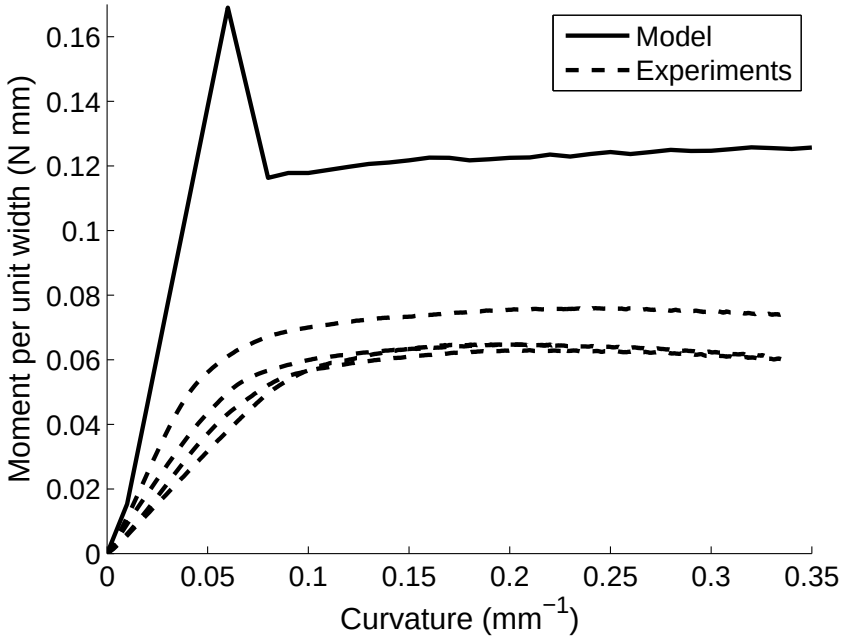

Figure 6.1: Comparison of analytical and experimental moment vs. curvature for $V_f = 30\%$

In order to correct this effect, the thickness considered in the analytical model has been reduced to match the thickness of material in which fibers are present, as observed in the micrographs. In the case of $V_f = 30\%$, this represents a 25% reduction, going from 80 μm to 60 μm. The results are shown in Figure 6.2. The model still overestimates the stiffness of the material, but the results are much closer now. It also provides a good estimation of the curvature in which the nonlinearity starts taking place.

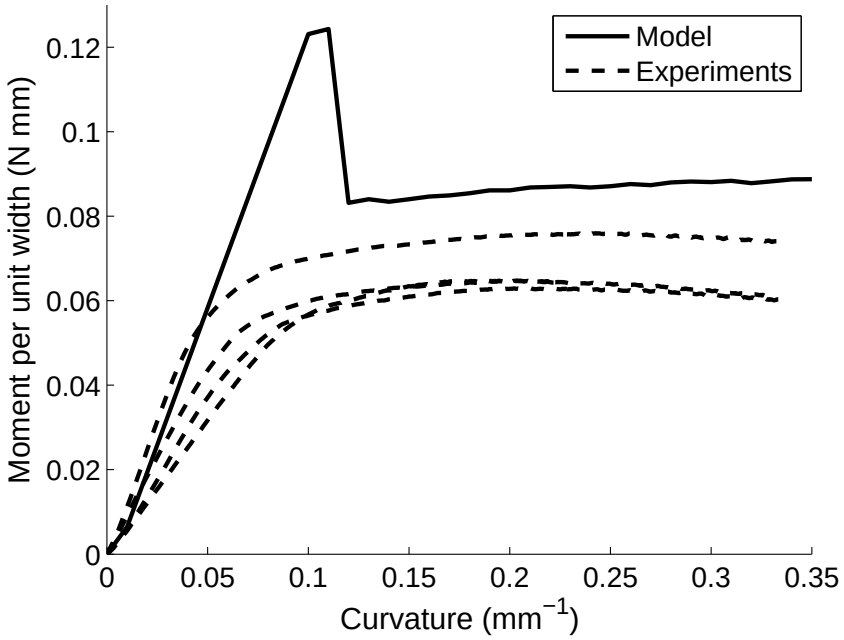

Figure 6.2: Comparison of analytical and experimental moment vs. curvature for $V_f = 30\%$. Corrected thickness

The discontinuity observed in the moment, similar to the one observed in the numerical results in Chapter 5, is due to the non-convexity of the strain energy. This situation does not happen in reality, since waviness and imperfections ensure a smooth transition to the post-buckled state. It can be fixed by choosing not the state with lower strain energy, but the state with lower moment. This produces an earlier transition to the buckled state, as seen in Figure 6.3. The moment curve is still not differentiable, but it resembles the experimental results much more closely.

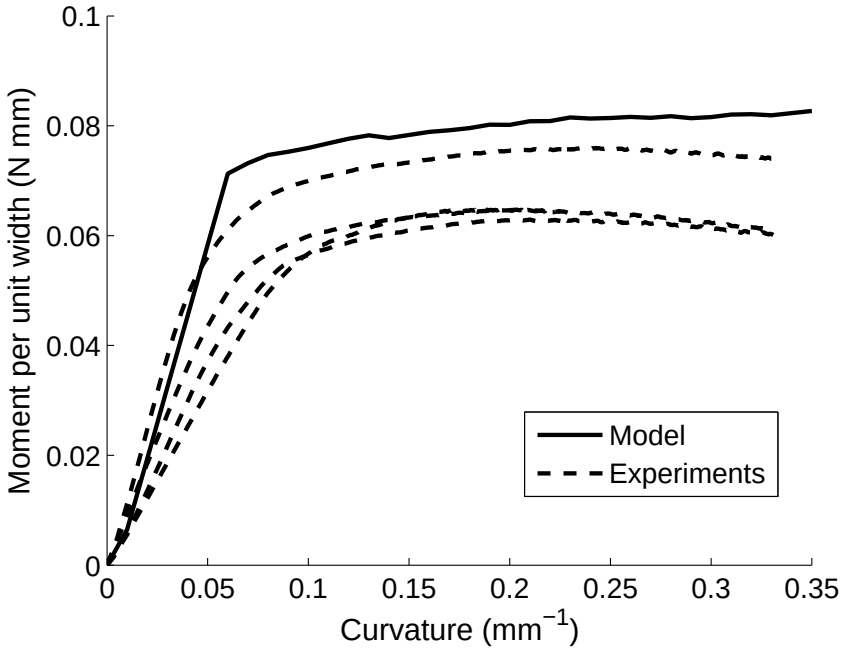

Figure 6.3: Comparison of analytical and experimental moment vs. curvature for $V_f = 30\%$. Corrected thickness, transition to buckling controlled by minimum moment

The specimens with $V_f = 55\%$ present much smaller silicone sections, and a reduction of only 90% in thickness (from 40 μm to 36 μm) has been applied in this case. As happened with the finite element results for these type of specimens, the predicted moment roughly doubles that obtained in the experiments, see Figure 6.4.

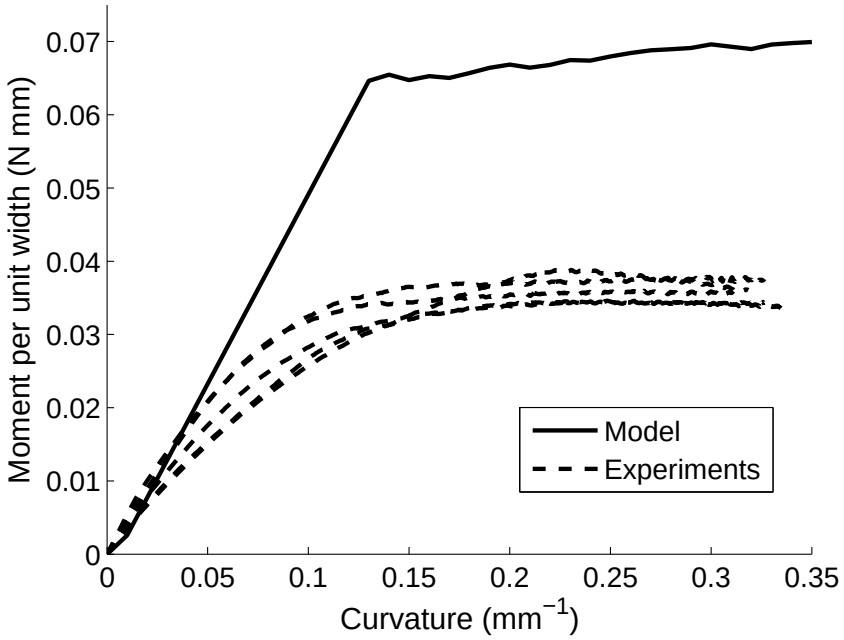

Figure 6.4: Comparison of analytical and experimental moment vs. curvature for $V_f = 55\%$. Corrected thickness, transition to buckling controlled by minimum moment

The wavelength provided by the model is 0.45 mm for $V_f = 30\%$ and 0.39 mm for $V_f = 55\%$. In both cases the values are lower than those observed experimentally, 0.6–0.65 mm and 0.55–0.7 mm, respectively, which implies that the energy contribution of the matrix has been overestimated.

The model also allows the analysis of the position of the neutral surface, and the surface in which buckling starts. Figure 6.5 shows the position of the neutral and buckling surfaces as a function of the applied curvatures. As expected, when the curvature is low, the neutral surface coincides with the geometric centroid, and the buckling surface with the surface with the material in the compression side, that is, there is no buckling. Once the instability appears, both surfaces move towards the tension side. The material then presents a tension region, a very small linear compression region, and the post-buckled region, taking most of the thickness.

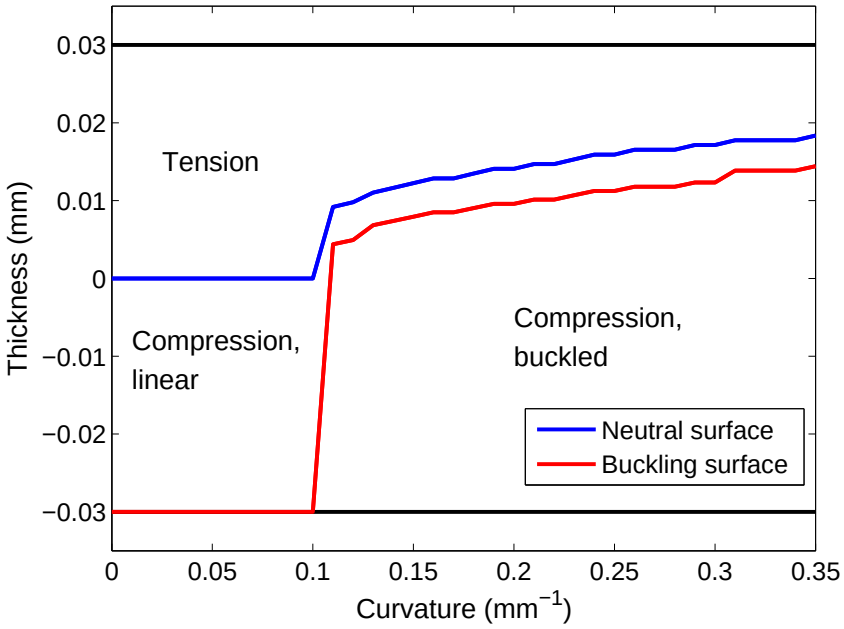

Figure 6.5: Position of the neutral and buckling surfaces as a function of the applied curvatures. The surfaces delimitate the three regions in the material: tension, linear compression and the buckled region in compression. $V_f = 0.3$

The model can be used to calculate the strain of the fibers, which for every region is expressed as:

$$\epsilon_{f,tension} = \kappa \left(\frac{t}{2} - z_n \right) \epsilon_{f,compression} = \kappa \left(z_b - z_n \right) \epsilon_{f,buckled} = \frac{da\pi^2}{2\lambda^2} \tag{6.19}$$

where the amplitude of the sine, a, is calculated as

$$a = \frac{2\lambda}{\pi} \sqrt{-\epsilon_x} = \frac{2\lambda}{\pi} \sqrt{\kappa (z - z_n)} \tag{6.20}$$

as it was detailed in Chapter 2.

Figure 6.6 shows the absolute value of the maximum fiber strain for the fibers in tension, as well as the maximum strain produced by the microbuckling waviness. The strain obtained with a linear Kirchhoff's linear theory. It corresponds to the strain in a composite with epoxy matrix, which would prevent microbuckling. The slope of the

strain decreases as the applied curvature increases, and at $\kappa = 2$ mm^{-1} the strain has not reached yet the failure value given by the manufacturer, 1.8%. As a comparison, failure will be reached at $\kappa = 0.6$ mm^{-1} if the behavior of the material is linear. The reason for the saw pattern observed in the figure is the fact that the displacements of the neutral and buckling surfaces towards the tension side is not smooth.

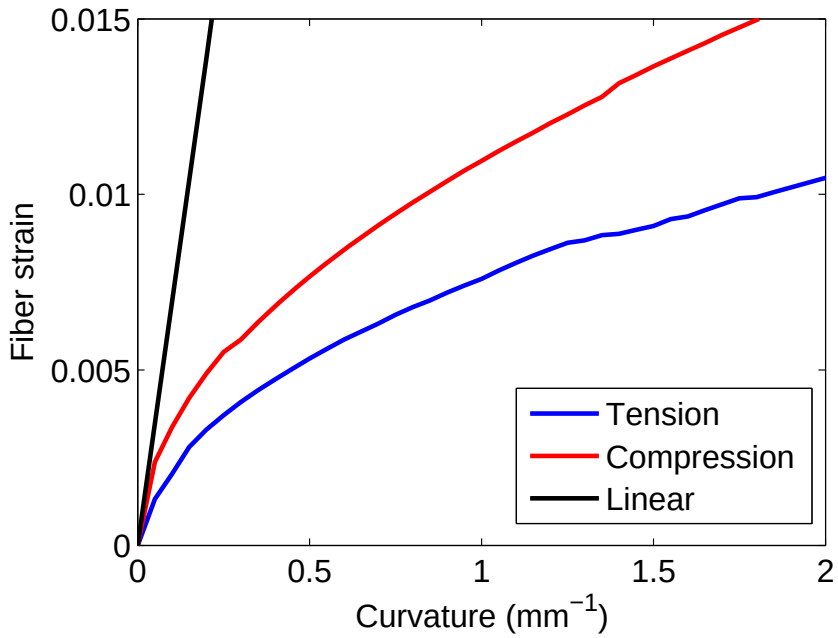

Figure 6.6: Absolute value of the maximum fiber strain for fibers in tension and buckled, as well as a linear case added for comparison. $V_f = 0.3$, 138 μm thickness

In addition to the reduction in maximum fiber strain due to microbuckling, it is important to also take into account how brittle fracture affects the maximum strain of carbon fiber and bending, as opposed to pure tension, as described in Section 3.1.1. Figure 6.7 shows the strain in the fiber, as well as the two lines showing the strain at which a fiber will break in pure tension (1.8%) and when 5% of the fibers will break in pure bending (2.9%), according to the results shown in Figure 3.3. This increases the failure curvature from $\kappa = 0.26$ mm^{-1} for the linear case, to $\kappa = 5.5$ mm^{-1}, which takes place in the fibers under tension, even if the maximum strain is higher for the buckled fibers.

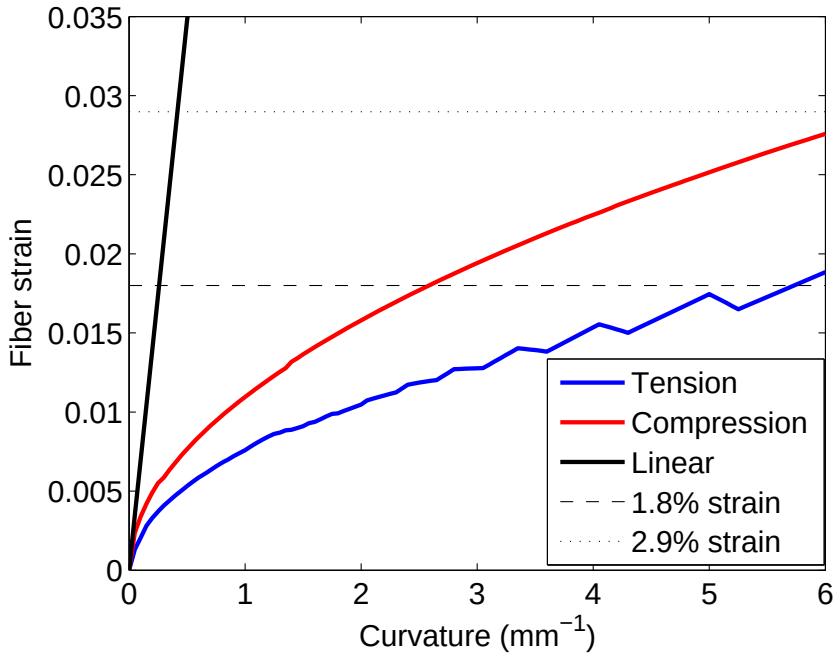

Figure 6.7: Absolute value of the maximum fiber strain for fibers in tension and buckled, as well as a linear case added for comparison. $V_f = 0.3$, 138 μm thickness. The two horizontal lines show the strain at which a fiber will break in pure tension (1.8%) and bending (2.9%)

Chapter 7

Conclusions

This thesis has presented a study of a composite material consisting of unidirectional carbon fibers in a silicone matrix, which is several orders of magnitude softer than the fibers. This type of composite can be folded to very high curvatures, due to the fiber's ability to microbuckle without breaking. This property makes it of interest in the design of stored-energy deployable structures, where the main limitation to the packaging factor is the curvature failure of the material.

The fabrication process used in this work has been presented, as well as a method to characterize the fiber arrangement with micrographs of the cross section. These micrographs show a very irregular fiber distribution, with clustering of fibers in specimens with low volume fraction. The fiber arrangement was taken into account during the finite element modeling of the material. The simulations show not only the importance of taking into account the actual fiber distribution, but also that the mechanics of the material would benefit from a regular fiber distribution. Fiber clustering, in particular, results in very high stress concentrations in the matrix. Efforts to improve the fabrication technique should focus on achieving a more homogeneous fiber distribution in the material.

The composite was then tested experimentally. The behavior under tension along the fiber direction is dominated by the fiber properties, and thus it does not differ from the typical behavior of fiber composites with epoxy matrix. The stiffness is linear, and about 5% to 10% lower than the approximation provided by the rules of mixtures. The reason is the initial waviness in the fibers, and it is likely to be reduced in thicker specimens. The behavior under bending, however, is very different from traditional composites. The composite can not only be folded to virtually zero radius of curvature, but it also presents

a very nonlinear moment vs. curvature relationship: after an initial linear stage, fiber microbuckling greatly reduces the stiffness of the material. At high curvatures, the incremental stiffness reaches negative values. The experiments also show stress softening under cyclic loading, similar to Mullins effect. It produces a decrease in stiffness, hysteretic behavior, and permanent deformation. It is more marked in specimens with higher fiber volume fraction.

In order to study the bending behavior, a finite element model was created in the commercial package ABAQUS/Standard. It uses a representative volume element (RVE) containing a small number of fibers, with periodic boundary conditions. It allows the study of not only the macroscopic response of the material, but also the microscopic fields. The fiber arrangement was modeled using two different approaches: a regular hexagonal lattice, and a random process based on the distribution observed in the material micrographs. The model is able to capture the fiber microbuckling, and shows how it greatly decreases the strain in the fibers when the material is folded. The model can therefore be used to predict the curvature at which fiber failure will take place, which is much higher than in the case of composites with an epoxy matrix, in which microbuckling does not take place. This research has also shown how fiber failure occurs in the tension section in the material, even if the maximum strain observed is higher in the microbuckled fibers, due to the flaw dependent nature of brittle failure. A complete characterization of fiber failure could be used to implement a probabilistic failure criteria in the 3D simulations.

The simulations can also be used to calculate the moment vs. curvature relationship. In specimens with low fiber volume fraction (30%), the simulations provide a good approximation, although they overestimate the stiffness after buckling. In cases with high fiber volume fraction (55%), the simulations predict a much stiffer response than that observed experimentally. The reason are the idealizations in the modeling of the material. In particular, it has been assumed that the bonding between fibers and matrix is perfect, and no failure mechanism for the matrix has been included, neglecting mechanisms like fracture in the matrix, debonding, or cavitation. The finite element results show very high strains in the matrix (more than 200%), which suggest that some damage mechanism would have taken place before. This explains the disagreement with the experiments.

There are two other main limitations to the model. The first is the assumption that all

fibers are parallel and perfectly straight. This will produce a model with an initial stiffness higher than that observed in the experiments, and with a less smooth transition to the post-buckled state. However, this should not affect the postbuckled behavior, when the waviness of the fibers due to the buckling is much higher than initially. A slight waviness was introduced in some simulations, which smoothed the buckling process, producing a better agreement with the experimental results. However, the introduced waviness was the same for all the fibers. A more realistic analysis will require introducing misalignment between the fibers in the same RVE, and studying its influence on the results.

The second limitation is the small size of the RVE used. This limit was imposed by the high computational cost of the simulation. The implication of using a small RVE to model a problem with instabilities is that all possible solutions neglect instabilities whose representative size (such as the wavelength for a beam buckling problem) is larger than the RVE. The only instability observed in the experiments was the fiber microbuckling, which was captured by the model. Therefore, the results provided by increasing the size of the RVE are not likely to be very different from the ones presented here. However, the buckling pattern observed in pictures of the material was not perfectly homogeneous across the width of the specimens. Using a wider RVE might help to capture the different buckling wavelengths observed experimentally and study how they interact with each other.

In order to understand the effect of the damage in the matrix, the material was tested under loading transverse to the fiber direction. This experiment still shows strain softening, but it does not include the additional geometric nonlinearity due to microbuckling, and that isolates the effect of the material damage. The behavior is again very nonlinear, with an initial linear response that changes to a region in which the average stress in the material remains basically constant when the applied strain is increased. Strain softening is very important in specimens with high fiber volume fraction, while it has almost no effect in specimens with low volume fraction, due to the lower stress concentration.

The behavior under transverse loading was studied with a two-dimensional simulation, under plane strain assumption. Attempts to use generalized plane strain, leaving the out-of-plane coordinate free, produced the same results. This is due to the high stiffness of the fibers, which prevents strain in their longitudinal direction. The fiber arrangement

was constructed using the same procedure as the previous models, and in this case the model uses a RVE with periodic boundary conditions on both sides. Assuming perfect bonding leads to an almost linear response that greatly overestimates the stresses observed in the experiments. In order to capture the nonlinearity and strain softening due to fiber debonding, cohesive elements have been introduced between the fibers and the matrix. This allows the two-dimensional model to replicate the non-linear behavior, as well as the damage under cyclic loading. The simulations are still not able to capture the hysteresis or the permanent deformation, since the unloading-reloading behavior of the cohesive elements is elastic. The model still neglects failure within the matrix, such as cavitation. No failure models specific for silicone rubber were found in the literature, so it is not possible to do a proper analysis, especially when multiaxial loading states are involved. However, the microscopic strains observed in the 2D simulations are well below the failure point observed in the experiments, which indicates that neglecting the matrix failure and focusing on debonding is a reasonable hypothesis.

The transverse loading test provides two important results. First, it can be used as a measure of damage, comparing the experimental results with the simulations obtained assuming perfect bonding. This technique can be used to compare different types of silicones (with special interest in space-qualified silicones) or fiber sizing, in order to find the best combination of materials. Second, the cohesive elements can be calibrated with the transverse simulations, and then used in the analysis of more complicated loading cases, such as bending or biaxial tension. In particular, cohesive elements could be introduced in the 3D bending simulations, but it is computationally very expensive. The numerical model could even be used to predict complete failure in the material if a mechanism for matrix failure is introduced. This can be achieved by introducing cohesive elements within the matrix elements. In this case, the parameters controlling the damage initiation of the cohesive elements will be given by the critical stretch of the silicone.

An additional result found is the fact that the transverse stiffness of composites with a silicone matrix is much higher than what would be predicted using traditional tools, such as the Halpin-Tsai equations. The simulations have shown that the primary source of disagreement is in the incompressibility in the silicone matrix, by using the numerical model to perform a parametric study varying the properties of the matrix. In particular, the

simulations modeling the matrix as epoxy show good agreement with the corresponding Halpin-Tsai predictions.

In addition to the simulations, a homogenized model of the material has also been created. It provides a good qualitative description of the material behavior, and it helps understand the mechanics that take place, such as the equilibrium of energy terms leading to a finite wave length, as opposed to microbuckling under compression. It also shows how the microbuckling greatly reduces the strain in the fibers. However, it overestimates the effect of the matrix, leading to very short fiber wavelength, as well as a stiffer response than that observed in the experiments. Before it can be used as a design tool, this analytical model needs to be improved to accurately predict the moment vs. curvature relationship, as well as the failure parameters, such as strain in the fibers. Possible modifications include using a large strain formulation, as well as a geometrical description that allows the buckles to extend into the tension side, as it is observed in the real material. An accurate analytical model will also be useful in the analysis of thicker composites, for which a finite element model like the one presented in this work might be computationally too expensive.

Such an analytical model will greatly benefit from the numerical models used in this work, in order to incorporate the effect of the microstructure on the matrix stiffness. In homogenized composite models it is common to use a description for the matrix that matches not the behavior of the pure material, but the behavior including the effect of the stress concentrations. This is usually done by fitting experimental data, although the use of a finite element model like the one presented here could skip that step, at least in the initial stage of the design process, especially when considering that a wide range of volume fractions and types of matrix would make testing prohibitively expensive.

The present study has been performed on unidirectional thin composites since it is easier to focus on the mechanics of the fiber microbuckling. However, the work needs to be extended to thicker specimens, and composites with more than one fiber direction, both in the case of specimens with several plies of unidirectional fibers and those with woven composites. These are more interesting cases from an engineering point of view, and so it is important to study the interaction between the different fiber directions. Such specimens could also be tested in other load cases, such as compression and shear, for

which the very thin unidirectional specimens are too fragile.

From this research, there is enough information to provide various conclusions regarding the use of this type of composite in the design of space structures. Specimens with low volume fraction show better behavior, including less strain softening, higher bending stiffness, and larger failure strain, when loaded in the transverse direction. The main drawback is the same as with traditional composites, the fact that for a given maximum axial load, composites are lighter when they have a high fiber volume fraction. Weight is great concern in the design of space structures, and so it will be important to modify the fabrication process to obtain specimens with high volume fraction and low damage in the matrix, especially if a large structure is to be designed with composites with a hyperelastic matrix. However, if the composite with a soft matrix is only going to be used in a small region, such as a hinge that is part of a larger structure composed of traditional composites, the improved mechanical properties might compensate for the extra weight. In a design with more than one type of matrix, it will also be necessary to study the interaction between regions with epoxy and silicone matrix in the same composite.

Bibliography

ABAQUS/Standard. Software, Ver. 6.7, Simulia, Providence, R.I., 2007.

D. S. Adams and M. Mobrem. Lenticular jointed antenna deployment anomaly and resolution onboard the Mars Express Spacecraft. *Journal of Spacecraft and Rockets*, 46: 403–410, 2009.

Adobe Photoshop CS4. Software, Adobe, San Jose, CA, 2008.

M. Agoras, O. Lopez-Pamies, and P. Ponte Castañeda. A general hyperelastic model for incompressible fiber-reinforced elastomers. *Journal of the Mechanics and Physics of Solids*, 57:268286, 2009.

M. F. Ashby and D. R. H. Jones. *Engineering Materials 2. An Introduction to Microsctures, Processing and Design.* Pergamon Press, Oxford, UK, first edition, 1986.

M. F. Beatty and S. Krishnaswamy. A theory of stress-softening in incompressible isotropic materials. *Journal of the Mechanics and Physics of Solids*, 48:1931–1965, 2000.

J. S. Bergström and M. C. Boyce. Constitutive modeling of the large strain time-dependent behavior of elastomers. *Journal of the Mechanics and Physics of Solids*, 46:931–954, 1998.

K. Bertoldi and M. C. Boyce. Mechanics of the hysteretic large strain behavior of mussel byssus threads. *Journal of Materials Science*, 42:8943–8956, 2007.

D. Campbell, M.S. Lake, and K. Mallick. A study of the bending mechanics of elastic memory composites. In *45th AIAA/ASME/ASCE/AHS/ASC Structures, Structural Dynamics, and Materials Conference*, Palm Springs, CA, 2004.

K. Cho and A. N. Gent. Cavitation in model elastomeric composites. *Journal of Materials Science*, 23:141–144, 1988.

K. Cho, A. N. Gent, and P. S. Lam. Internal fracture in an elastomer containing a rigid inclusion. *Journal of Materials Science*, 22:2899–2905, 1987.

L. Datashvili, H. Baier, E. Wehrle, T. Kuhn, and J. Hoffmann. Large shell-membrane space reflectors. In *51st AIAA/ASME/ASCE/AHS/ASC Structures, Structural Dynamics, and Materials Conference*, number AIAA-2010-2504, Orlando, Florida, 2010.

P.J. Davy and F.J. Guild. The distribution of interparticle distance and its application in finite-element modelling of composite materials. *Proceedings of the Royal Society of London*, 418:95–112, 1988.

J. Diani, B. Fayolle, and P. Gilormini. A review on the Mullins effect. *European Polymer Journal*, 45:601–612, 2009.

J. B. Donnet, T. K. Wang, J. C. M. Peng, and S. Rebouillat. *Carbon Fibers*. Marcel Dekker, New York, third edition, 1998.

A. Dorfmann and R. W. Odgen. A constitutive model for the Mullins effect with permanent set in particle-reinforced rubber. *International Journal of Solids and Structures*, pages 1855–1878, 2004.

S. Drapier, C. Garding, J.-C. Grandidier, and M. Potier-Ferry. Structure effect and microbuckling. *Composites Science and Technology*, 56:861–867, 1996.

S. Drapier, J.-C. Grandidier, and M. Potier-Ferry. Towards a numerical model of the compressive strength for long fibre composites. *European Journal of Mechanics A—Solids*, 18:69–92, 1999.

S. Drapier, J.-C. Grandidier, and M. Potier-Ferry. A structural approach of plastic microbuckling in long fibre composites: comparison with theoretical and experimental results. *International Journal of Solids and Structures*, 38:3877–3904, 2001.

N. A. Fleck. Compressive failure of fiber composites. *Advances in Applied Mechanics*, 33: 43–117, 1997.

W. H. Francis. Mechanics of post-microbuckled compliant-matrix composites. Master's thesis, Colorado State University, 2008.

W. H. Francis, M.S. Lake, and J. Steven Mayes. A review of classical fiber microbuckling analytical solutions for use with elastic memory composites. In *47th AIAA/ASME/ASCE/AHS/ASC Structures, Structural Dynamics, and Materials Conference*, number AIAA-2006-1764, Newport, RI, 2006.

Y.C. Fung. *Biomechanics. Mechanical Properties of Living Tissues.* Springer, New York, second edition, 1972.

K. Gall, M. Mikulas, N. A. Munshi, F. Beavers, and M. Tupper. Carbon fiber reinforced shape memory polymer composites. *Journal of Intelligent Material Systems and Structures*, 11:877–886, 2000.

A. N. Gent. Detachment of an elastic matrix from a rigid spherical inclusion. *Journal of Materials Science*, 15:2884–2888, 1980.

A. N. Gent. Elastic instabilities in rubber. *International Journal of Non-Linear Mechanics*, 40:165–175, 2005.

A. N. Gent and P. B. Lindley. Internal rupture of bonded rubber cylinders in tension. *Proceedings of the Royal Society of London—A*, 249:195–205, 1959.

A. N. Gent and B. Park. Failure processes in elastomers at or near a rigid spherical inclusion. *Journal of Materials Science*, 19:1947–1956, 1984.

G. Geymonat, S. Müller, and N. Triantafyllidis. Homogenization of nonlinearly elastic materials, microscopic bifurcation and macroscopic loss of rank-one convexity. *Archive for Rational Mechanics and Analysis*, 122:231–290, 1993.

S. Govindjee and J. Simo. A micro-mechanically based continuum damage model for carbon black-filled rubbers incorporating Mullins' effect. *Journal of the Mechanics and Physics of Solids*, 39:87–112, 1991.

J. C. Halpin and J. L. Kardos. The Halpin-Tsai equations: A review. *Polymer Engineering and Science*, 16:344–352, 1976.

Z. Hashin and B. W. Rosen. The elastic moduli of fiber-reinforced materials. *Journal of Applied Mechanics*, 31:223–232, 1964.

G. A. Holzapfel, T. C. Gasser, and R. W. Ogden. A new constitutive framework for arterial wall mechanics and a comparative study of material models. *Journal of Elasticity*, 61: 1–48, 2000.

R. M. Jones. *Mechanics of composite materials*. Taylor Francis, Philadelphia, second edition, 1999.

X. Lan, Y. Liu, H. Lv, X. Wang, J. Leng, and S. Du. Fiber reinforced shape-memory polymer composite and its application in a deployable hinge. *Smart Materials and Structures*, 18:1–6, 2009.

M. Leipold, H. Runge, and C. Sickinger. Large SAR membrane antennas with lightweight deployable booms. In *28th ESA Antenna Workshop on Space Antenna Systems and Technologies*, ESA/ESTEC, 2005.

F. Lopez Jimenez and S. Pellegrino. Folding of thin-walled composite structures with a soft matrix. In *50th AIAA/ASME/ASCE/AHS/ASC Structures, Structural Dynamics, and Materials Conference*, number AIAA-2009-2633, Palm Springs, California, 2009.

O. Lopez-Pamies and M. I. Idiart. Fiber-reinforced hyperelastic solids: a realizable homogenization constitutive theory. *Journal of Engineering Mathematics*, 2010.

O. Lopez-Pamies and P. Ponte Castañeda. On the overall behavior, microstructure evolution, and macroscopic stability in reinforced rubbers at large deformations: II—Application to cylindrical fibers. *Journal of the Mechanics and Physics of Solids*, 54: 831863, 2006.

G. Machado, G. Chagnon, and D. Favier. Analysis of the isotropic models of the Mullins effect based on filled silicone rubber experimental results. *Mechanics of Materials*, 42: 841–851, 2010.

R. Marissen and H. R. Brouwer. The significance of fibre microbuckling for the flexural strength of a composite. *Composites Science and Technology*, 59:327–330, 1999.

J. M. Mejia-Ariza, E. L. Pollard, and T. W. Murphey. Manufacture and experimental analysis of a concentrated strain based deployable truss structure. In *47th AIAA/ASME/ASCE/AHS/ASC Structures, Structural Dynamics, and Materials Conference*, number AIAA-2006-1686, Newport, Rhode Island, 2006.

J. M. Mejia-Ariza, K. Guidanean, T. M. Murphey, and A. Biskner. Mechanical characterization of L'Garde elastomeric resin composite materials. In *51st AIAA/ASME/ASCE/AHS/ASC Structures, Structural Dynamics, and Materials Conference*, number AIAA-2010-2701, 2010a.

J. M. Mejia-Ariza, T. W. Murphey, and H. P. Dumm. Deployable trusses based on large rotation flexure hinges. *Journal of Spacecraft and Rockets*, 47:1053–1062, 2010b.

J. Merodio and R. W. Ogden. Material instabilities in fiber-reinforced nonlinearly elastic solids under plane deformation. *Archives of Mechanics*, 54:525–552, 2002.

J. Merodio and R. W. Ogden. Instabilities and loss of ellipticity in fiber-reinforced compressible non-linearly elastic solids under plane deformation. *International Journal of Solids and Structures*, 40:4707–4727, 2003.

L. Meunier, G. Chagnon, D. Favier, L. Orgéas, and P. Vacher. Mechanical experimental characterization and numerical modelling of an unfilled silicone rubber. *Polymer Testing*, 27:765–777, 2008.

I. Monetto and W. J. Drugan. A micromechanics-based nonlocal constitutive equation for elastic composites containing randomly oriented spheroidal heterogeneities. *Journal of the Mechanics and Physics of Solids*, 52:359–393, 2004.

J. Moraleda, J. Segurado, and J. Llorca. Finite deformation of incompressible fiber-reinforced elastomers: A computational micromechanics approach. *Journal of the Mechanics and Physics of Solids*, 57(9):1596–1613, 2009a.

J. Moraleda, J. Segurado, and J. Llorca. Effect of interface fracture on the tensile deformation of fiber-reinforced elastomers. *International Journal of Solids and Structures*, 46(9):4287–4297, 2009b.

S. Müller. Homogenization of nonconvex integral functionals and cellular elastic materials. *Archive for Rational Mechanics and Analysis*, 99:189–212, 1987.

T. W. Murphey, T. Meink, and M. M. Mikulas. Some micromechanics considerations of the folding of rigidizable composite materials. In *42nd AIAA/ASME/ASCE/AHS/ASC Structures, Structural Dynamics, and Materials Conference*, number AIAA-2001-1418, 2001.

NASA Science News. http://science.nasa.gov/science-news/science-at-nasa/2010/07jan_nustar/, January 7 2010.

NuSil Silicone Technology. http://www.nusil.com/library/products/CF19-2615P.pdf, March 2007.

R. W. Ogden and D. G. Roxburgh. A pseudo-elastic model for the Mullins effect in filled rubber. *Proceedings of the Royal Society*, 455:2861–2877, 1999.

A. Pandolfi and G. A. Holzapfel. Three-dimensional modeling and computational analysis of the human cornea considering distributed collagen fibril orientations. *Journal of Biomechanical Engineering*, 130, 2008.

A. Pandolfi and F. Manganiello. A model for the human cornea: constitutive formulation and numerical analysis. *Biomechanics and Modeling in Mechanobiology*, 5:237–246, 2006.

R. Parnes and A. Chiskis. Buckling of nano-fibre reinforced composites: a re-examination of elastic buckling. *Journal of the Mechanics and Physics of Solids*, 50:855–879, 2002.

P. Ponte Castañeda. Second-order homogenization estimates for nonlinear composites incorporating field fluctuations: I—Theory. *Journal of the Mechanics and Physics of Solids*, page 737757, 2002.

G.L. Povirk. Incorporation of microstructural information into models of two-phase materials. *Acta Metallurgica et Materialia*, 43:3199–3206, 1995.

R. Pyrz. Correlation of microstructure variability and local stress field in two-phase materials. *Materials Science and Engineering*, 177:253–259, 1994a.

R. Pyrz. Quantitative description of the microstructure of composites. Part I: Morphology of unidirectional composite systems. *Composites Science and Technology*, 50:197–208, 1994b.

R. Pyrz and B. Bochenek. Topological disorder of microstructure and its relation to the stress field. *International Journal of Solids and Structures*, 35:2413–2427, 1998.

G. Ravichandran and C. T. Liu. Modeling constitutive behavior of particulate composites undergoing damage. *International Journal of Solids and Structures*, 32:979–990, 1995.

F. Rehnmark, M. Pryor, B. Holmes, D. Schaechter, N. Pedreiro, and C. Carrington. Development of a deployable nonmetallic boom for reconfigurable systems of small spacecraft. In *48th AIAA/ASME/ASCE/AHS/ASC Structures, Structural Dynamics, and Materials Conference*, number AIAA-2007-2184, Honolulu, Hawaii, 2007.

M.D. Rintoul and S. Torquato. Reconstruction of the structure of dispersions. *Journal of Colloid and Interface Science*, 186:467–476, 1997.

B.W. Rosen. *Fiber Composite Materials*. Metals Park, Ohio, 1965.

J. C. Simo. On a fully three-dimensional finite-strain viscoelastic damage model: formulation and computational aspects. *Computer Methods in Applied Mechanics and Engineering*, 60:153–173, 1987.

A. J. M. Spencer. Constitutive theory of strongly anisotropic solids. In International Centre for Mechanical Sciences, editor, *Continuum theory of the mechanics of fibre-reinforced composites*. 1972.

L. T. Tan and S. Pellegrino. Thin-shell deployable reectors with collapsible stiffeners: Part 1 approach. *AIAA Journal*, 44:2515–2523, 2006.

M. Tanemura. On random complete packing by disks. *Annals of the Institute of Statistical Mathematics*, 31:351–365, 1979.

S. P. Timoshenko and J. M. Gere. *Theory of Stability*. 1936.

Toho Tenax. http://www.tohotenax.com/tenax/en/products/st_property.php, retrieved August 2010.

W. Tong and G. Ravichandran. Effective elastic moduli and characterization of a particle metal-matrix composite with damaged particles. *Composites Science and Technology*, 52:247–252, 1994.

N. Triantafyllidis and R. Abeyaratne. Instabilities of a finitely deformed fiber-reinforced elastic material. *Journal of Applied Mechanics*, 50:149–156, 1983.

X. A. Zhong and W. G. Knauss. Analysis of interfacial failure in particle-filled elastomers. *Transactions of the ASME*, 119:198–204, 1997.

X. A. Zhong and W. G. Knauss. Effects of particle interaction and size variation on damage evolution in filled elastomers. *Mechanics of Composite Materials and Structures*, 7:35–53, 2000.

Appendix A

ABAQUS Details

This appendix offers some specific details regarding the finite element model, including information on the numerical stability of the problem, as well as on the specific commands used in ABAQUS to model the boundary conditions.

A.1 Stabilization and increment control

In the case of unstable problems, ABAQUS offers the possibility of stabilizing the problem with the addition of numerical damping to the model. The viscous forces have the form:

$$F_v = c\mathbf{M}^* v \tag{A.1}$$

where $\mathbf{M}^*$ is an artificial mass matrix with unit density, c is the damping factor (which can be constant or vary during the analysis), and $v = \frac{\Delta u}{\Delta t}$ is the vector of nodal velocities, which may or may not have a physical meaning. The option is activated with the command:

```
*Static, STABILIZE
```

This introduces damping so that a fraction to that the ratio between energy lost to the fictitious viscous forces and total energy does not surpass a given value. The default value is $2 \cdot 10^{-4}$, but it can be specified using:

```
*Static, STABILIZE = 2e-4
```

However, the two previous statements are not equivalent. If a value is specified, ABAQUS obtains an estimate of the damping factor c using the first increment of the step,

and it maintains it during the whole step. In the other case, this initial estimate can change during the analysis. This is important when the first increment is not representative of the subsequent ones, as is the case here. The adaptive automatic stabilization scheme can be activated when the the stabilization factor is directly prescribed using the `ALLSDTOL` command. However, it was found easier to use the default setting of the stabilization, and just reduce the initial increment of the step until sufficient convergence was achieved The simulations are also dependent on the minimum step, even if it is never reached. The most probable reason is that it is also used to calculate the damping coefficient, although this is not specified in the manual. A value of 0.01, equal to the initial increment, was used in most simulations.

It is often the case that the size of the increments need to be reduced suddenly, once the simulation reaches a bifurcation point. By default, ABAQUS halves the size of every subsequent attempt to solve an increment, and stops the simulation due to lack of convergence if a solution is not found after five attempts, or when more than 100 increments are required. This can be changed with the option:

```
*Step, nlgeom=yes, INC = 4000, name=StaticLoad
*Static, STABILIZE
0.01,1,1e-15,0.01
* CONTROLS, PARAMETERS = TIME INCREMENTATION
,,,,,,,20,,,,
```

which in this case sets the total number of increments in the step to 4000, and makes it possible to have 20 consecutive attempts to solve a given increment.

Figure A.1 shows a typical evolution of the analysis with respect to the number of increments, showing how it is common to have a large number of very large increments to later recover stability.

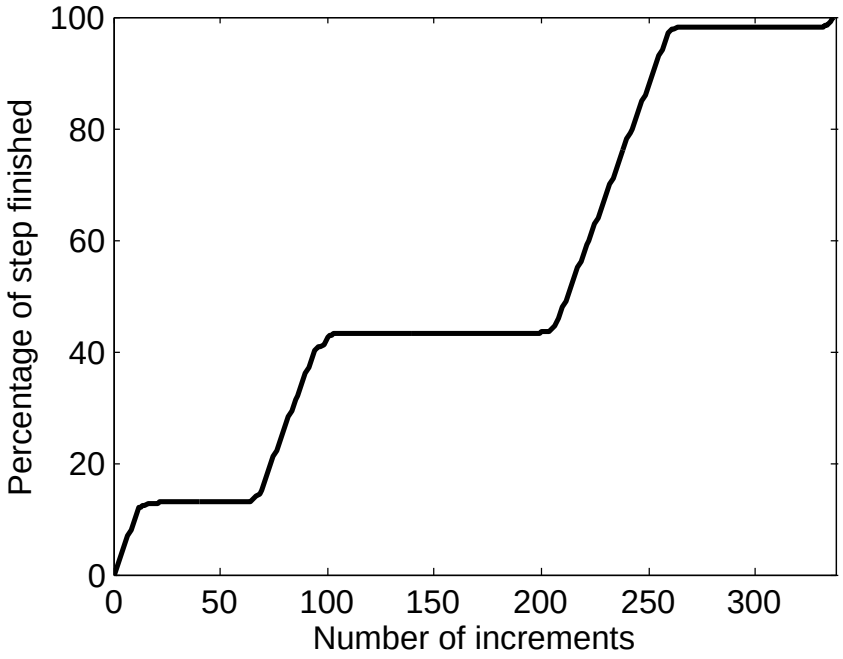

Figure A.1: Typical simulation progress vs. number of increments. The simulation is a 3D folding simulation, 30% volume fraction, hexagonal fiber arrangement

The automatic stabilization is usually required in the 3D simulations. It might be omitted if the imperfection seeded into the system leads to a smooth transition to the buckled state. However, the stabilization scheme is required in most cases, and it is able to stabilize the simulations even in cases in which a wrong wave length is used for the imperfection. In that case there would more than one jump in the transition to the buckled state: one to the wrong wave length, and the second to the correct number. This second stiffness agrees with the one obtained introducing the correct wave length in the imperfection, see Figure A.2.

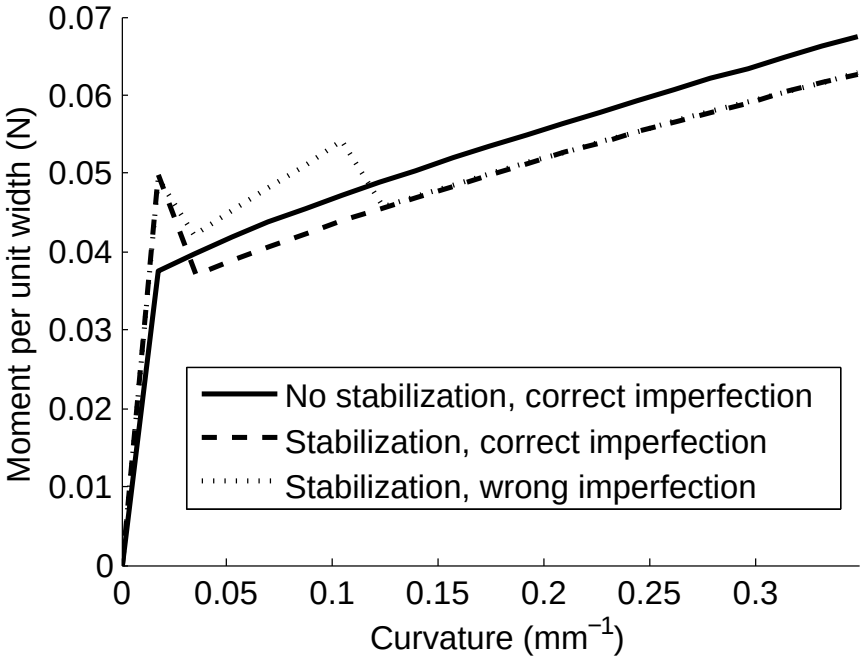

Figure A.2: Moment-curvature for different options of applied stabilization and seeded imperfections. The simulation is a 3D folding simulation, 30% volume fraction, hexagonal fiber arrangement

In the case of the 2D simulations with perfect bonding the stabilization is not required, but including it does not affect the simulations, since with the adaptive automatic stabilization scheme the damping is only noticeable in the case of poor convergence.

A.2 Boundary conditions

Two main boundary conditions are applied in the simulations: periodic boundary conditions, and a rotation at the ends of the model for the folding simulations. In both cases, the boundary conditions require most of the nodes in the boundary to be connected to dummy nodes with the commands `Kinematic Coupling` and `Equation`. ABAQUS tends to eliminate all the degrees of freedom of nodes that are already a slave of another node, even if that particular degree of freedom was not included in the relationship. For that reason, extra dummy nods need to be included in some cases, in order to apply all the required conditions.

A.2.1 Three-dimensional simulations

Regarding the ends of the model, that is, the intersections with the planes $x = \frac{L}{2}$ and $x = \frac{-L}{2}$, all the nodes are coupled to two reference nodes, `node_x_plus` and `node_x_minus`, respectively. For most of the nodes, only the displacement in the x direction is coupled. That forces the node to lie in a plane with moves as the dummy nodes rotate, but they are free to move within the plane. One additional node in each face, `node_center_x_plus` and `node_center_x_minus`, have additional degrees of freedom couple, in order to eliminate the rigid body motions in the material.

```
* Kinematic Coupling, REF NODE=node_x_minus
     nodes_face_x_minus, 1, 1
     node_center_x_minus, 1, 3
* Kinematic Coupling, REF NODE=node_x_plus
     nodes_face_x_plus, 1, 1
     node_center_x_plus, 1, 2
```

The faces in which boundary conditions are applied need to be connected with each other. The displacement in the x and y connections is made equal in both faces, while the difference of displacements in the z direction is made equal to the displacement of the dummy node `node_z_plus`, whose boundary condition will be to have zero force applied. This gives the model constant width, but does not impose a particular value.

```
* EQUATION
     2
     nodes_face_z_plus, 1, 1, nodes_face_z_minus, 1, -1
* EQUATION
     2
     nodes_face_z_plus, 2, 1, nodes_face_z_minus, 2, -1
* EQUATION
     3
     nodes_face_z_plus, 3, 1, nodes_face_z_minus, 3, -1,
                                        node_z_plus, 3, -1
```

The final boundary conditions applied on the dummy nodes are:

```
*Boundary
node_x_minus, 1, 5, 0
node_x_plus, 2, 5, 0
node_z_plus, 1, 2, 0
node_z_plus, 4, 6, 0
*Boundary, TYPE=VELOCITY
node_x_minus, 6, 6, -1.745329e-001
node_x_plus, 6, 6, 1.745329e-001
```

The boundary conditions in velocity are more convenient in the case of nonlinear deformations, specially in cases with more than one step.

A.2.2 Two-dimensional simulations

In this case, periodic boundary conditions were applied in the four sides of the model. This is achieved in all the nodes that are not in the corners of the RVE with the equation command, making distance between faces equal to the displacements of the dummy nodes `node_z_plus` and `node_y_plus`.

```
* EQUATION
     2
     nodes_face_z_plus, 1, 1, nodes_face_z_minus, 1, -1
* EQUATION
     3
     nodes_face_z_plus, 2, 1, nodes_face_z_minus, 2, -1,
                                        node_z_plus, 2, -1
* EQUATION
     3
     nodes_face_y_plus, 1, 1, nodes_face_y_minus, 1, -1,
                                        node_y_plus, 1, -1
* EQUATION
```

```
     2
     nodes_face_y_plus, 2, 1, nodes_face_y_minus, 2, -1
```

In the case of the nodes of the corners, it is necessary to first connect them to specific dummy nodes

```
* EQUATION
     3
     nodes_y_plus_z_plus, 2, 1, nodes_y_plus_z_minus, 2, -1,
                                    node_z_plus_corners, 2, -1
* EQUATION
     3
     nodes_y_minus_z_plus, 2, 1, nodes_y_minus_z_minus, 2, -1,
                                    node_z_plus_corners, 2, -1
* EQUATION
     3
     nodes_y_plus_z_plus, 1, 1, nodes_y_minus_z_plus, 1, -1,
                                    node_y_plus_corners, 1, -1
* EQUATION
     3
     nodes_y_plus_z_minus, 1, 1, nodes_y_minus_z_minus, 1, -1,
                                    node_y_plus_corners, 1, -1
```

that are the ones that move according to the displacement applied on the main dummy nodes:

```
* EQUATION
     2
     node_y_plus_corners, 1, 1, node_y_plus, 1, -1
* EQUATION
     2
     node_z_plus_corners, 2, 1, node_z_plus, 2, -1
```

The strain is applied through the displacement boundary conditions in the dummy node `node_z_plus`. Additionally, all the displacements of a node in the center of the RVE are made equal to zero. This is necessary to eliminate rigid body motions, since the rest of the boundary conditions are only applied as difference in displacements.

```
*Boundary
node_z_plus, 2, 2, 1.000000e-003
node_center, 1, 2, 0
```

A.3 Hyperelastic model

The user-defined material subroutine `UHYPER` was used to incorporate the hyperelastic Gent potential into the model. The subroutine requires the definition of the strain energy, as well as its first and second derivatives with respect to I_1, I_2, and the volumetric component J_{el}. The latter are zero due to the incompressibility assumption. The code used is:

```
      SUBROUTINE UHYPER(BI1,BI2,AJ,U,UI1,UI2,UI3,TEMP,NOEL,
     1 CMNAME,INCMPFLAG,NUMSTATEV,STATEV,NUMFIELDV,FIELDV,
     2 FIELDVINC,NUMPROPS,PROPS)
C
      INCLUDE 'ABA_PARAM.INC'
C
      CHARACTER*80 CMNAME
      DIMENSION U(2),UI1(3),UI2(6),UI3(6),STATEV(*),FIELDV(*),
     2 FIELDVINC(*),PROPS(*)
      REAL*8 C1,C2,Jm


C     ENERGY
      IF (BI1 .LE. (PROPS(3)*0.9 + 3.0)) THEN
      U(1) = -PROPS(1)*PROPS(3)*LOG(1.0-(BI1-3.0)/PROPS(3)) +
     1 PROPS(2)*LOG(BI2/3.0)
```

```
      ELSE
        U(1) = -PROPS(1)*PROPS(3)*LOG(0.1) +
     1 (PROPS(1)/0.1)*(BI1 - 0.9*PROPS(3) - 3.0) +
     2 0.5*(PROPS(1)/0.1/0.1/PROPS(3))*((BI1-0.9*PROPS(3)-3.0)**2.0)
     3 +   PROPS(2)*LOG(BI2/3.0)
      END IF
      U(2) = 0.0
C     FIRST DERIVATIVE ENERGY
      IF (BI1 .LE. (PROPS(3)*0.9 + 3.0)) THEN
        UI1(1) = PROPS(1)/(1.0 - (BI1-3.0)/PROPS(3) )
      ELSE
        UI1(1) = (PROPS(1)/0.1) +
     1 (PROPS(1)/0.1/0.1/PROPS(3))*(BI1 - 0.9*PROPS(3) - 3.0)
      END IF
      UI1(2) = PROPS(2)/BI2
      UI1(3)= 0.0
C     SECOND DERIVATIVE ENERGY
      IF (BI1 .LE. (PROPS(3)*0.9 + 3.0)) THEN
        UI2(1) = (PROPS(1)/PROPS(3))/((1.0-(BI1-3.0)/PROPS(3))**2.0 )
      ELSE
        UI2(1) = (PROPS(1)/PROPS(3))/(0.1**2.0 )
      END IF
      UI2(2) = -PROPS(2)/ (BI2**2.0)
      UI2(3)= 0.0
      UI2(4)= 0.0
      UI2(5)= 0.0
      UI2(6)= 0.0
C     THIRD DERIVATIVE ENERGY
      UI3(1)= 0.0
      UI3(2)= 0.0
      UI3(3)= 0.0
```

```
UI3(4)= 0.0
UI3(5)= 0.0
UI3(6)= 0.0

RETURN
END
```

Appendix B

Fiber folding test

This appendix presents an analysis of the loads in the looped fiber used in Section 3.1.1 to calculate the failure curvature of fibers. The fiber would be modeled as an inextensible and unshearable elastic rod using Euler's elastica. The configuration considered is shown in Figure B.1. The problem is modeled as 2D, so the torsional component is neglected. As boundary conditions, it is assumed that only an axial force F is applied. In order to do so, it is important to find a relationship between the load applied and the geometry of the problem.

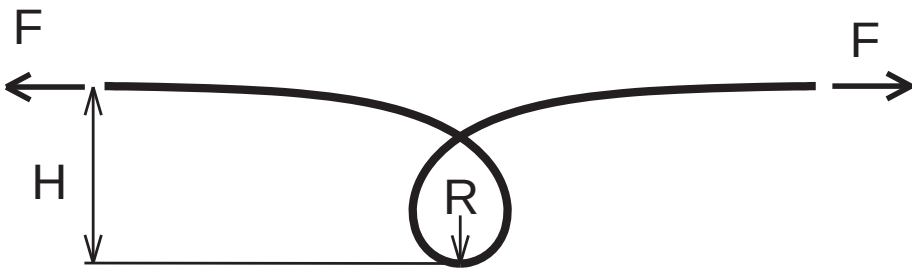

Figure B.1: Schematic of looped fiber used in folding test

First, by applying symmetry the problem can be reduced to the configuration seen in Figure B.2. The coordinate s describes the arclength of the rod, with origin at $x = y = 0$.

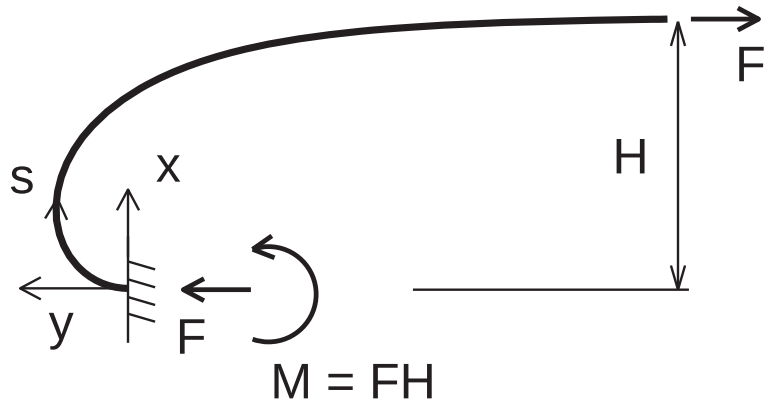

Figure B.2: Analysis of the looped fiber test after symmetry is applied

The differential equations modeling the tangent vector t are

$$\frac{dt_1}{ds} = \kappa t_2 \tag{B.1}$$

$$\frac{dt_2}{ds} = -\kappa t_1 \tag{B.2}$$

where t_i is the i-th component, and κ is the curvature.

The curvature is calculated with

$$\kappa = \frac{M}{EI} = \frac{F\,(H - x)}{EI}\ . \tag{B.3}$$

The differential equation can be expressed in the coordinate system $x - y$ as

$$x'' = A\,(H - x)\,y' \tag{B.4}$$

$$y'' = -A\,(H - x)\,x' \tag{B.5}$$

where $A = \frac{M}{EI}$, with boundary conditions

$$x(0) = 0 \qquad y(0) = 0 \tag{B.6}$$

$$x\prime(0) = 0 \qquad y\prime(0) = 1 \tag{B.7}$$

$$x\prime\prime(0) = \frac{FH}{EI} \qquad y\prime\prime(0) = 0 \tag{B.8}$$

$$x(\infty) = H \qquad y(\infty) = -\infty \tag{B.9}$$

$$x\prime(\infty) = 0 \qquad y\prime(\infty) = 1 \tag{B.10}$$

$$x\prime\prime(\infty) = 0 \qquad y\prime\prime(\infty) = 0\ . \tag{B.11}$$

This can be solved with a shooting method, iterating in F. The solution has been used to produce Figure B.1. However, the value of the load can be found analytically. The second equation can be integrated, which gives

$$y\prime = -AHx + \frac{Ax^2}{2} + C\ . \tag{B.12}$$

The boundary condition on $y\prime(0)$ makes $C = 1$. The second boundary condition ($s = \infty$), gives an equation that relates the values of H and the maximum radius of curvature at $s = 0$, R_{max}

$$H = 4R_{max}\ . \tag{B.13}$$

This provides a relationship between the applied force and the maximum curvature

$$F = \frac{\kappa_{max}^2 EI}{4}\ . \tag{B.14}$$

Assuming that the analysis is performed on a fiber of radius r, then the normal average strain can be expressed as a function of the maximum curvature

$$\epsilon = \frac{\kappa^2 I}{4A} = \left(\frac{r\kappa_{max}}{4}\right)^2\ . \tag{B.15}$$

The average axial strain for the curvatures observed in the test is shown in Figure B.3. The analysis shows that the axial loading can be neglected, and the fibers considered in pure bending.

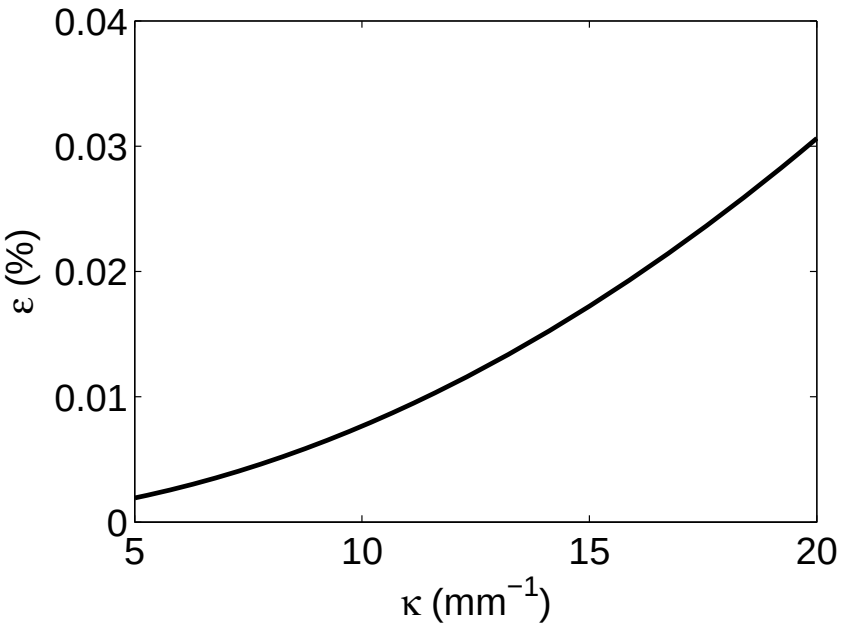

Figure B.3: Axial strain as a function of maximum curvature in the curvature test